Licentiate Thesis

Intricacy and Stability
of Graphene Spintronic Devices

Daria Belotcerkovtceva

UPPSALA
UNIVERSITET

Abstract

Graphene, the first experimentally isolated atomically thin crystal has displayed numerous superlative properties for quantum and spin-based electronics, as evidenced by research results of more than a decade. The scalable form of graphene, produced by the chemical vapor deposition (CVD) method has been increasingly attracting scientific and technological interest, as outstanding properties are combined with large scalability and high quality. The high-performance devices based on large-scale polycrystalline graphene growth capabilities with efficient charge and spin transport make it prospective for practical implementation into future spintronic and quantum integrated circuits. While CVD graphene presents unlimited prospects for exploring spin currents, there exist challenges along the way in terms of scalability of efficient performance, and reliability. Deformations, wrinkles, and structural (electronic) modifications caused at the interfaces with contacts remain key concerns for device performance. In particular, oxide-based interfaces with graphene are central to both graphenes electronic and spintronic devices. For high-performance scalable devices, it is of crucial significance to understand the details of these interfaces and how devices of CVD graphene with polycrystallinity respond to high current limits. In this thesis, we discuss a systematic study of the effect of e-beam evaporated ultra-thin titanium oxide (TiO_x) and aluminum oxide (AlO_x) on graphene; which are conventionally used as tunnel barriers in spintronic and nanoelectronics devices. Characteristic topographic features of both metal oxides on the graphene surface were revealed by atomic force microscopy. To estimate the impact of these oxides on graphene, electrical measurements were performed on graphene spin devices with and without metal oxides on the same devices. These measurements show significant p-type doping for both metal oxides, with sustained sheet conductance (σ_0) and mobility (μ) values. Strikingly, Raman spectroscopy and X-ray photoelectron spectroscopy show the emergence of significant sp^3 carbon for AlO_x on graphene, in sharp contrast to TiO_x. Our results and observations, together with theoretical calculations provide new insights into how sp^3 carbon for AlO_x can lead to new memristive mechanisms and explicate enhanced spin relaxation into graphene with AlO_x devices, which was widely attributed to the presence of interface pinholes. Here we also investigate how CVD graphene-based devices respond to high current stress to understand their stability and robustness. Despite the grainy and wrinkled structure, we observed the highest till-date current density of 5.2×10^8 A/cm^2, remarkably higher than previously reported values for multilayer graphene and graphene nanoribbons. The recorded reversible regime (~10^8 A/cm^2) for device operation allows reliable spin transport measurements with an observable spin signal up at such high current density. Furthermore, our investigation also encompasses cyclical current-voltage electrical measurement, to unveil the stability of graphene/ultra-thin oxide interfaces in graphene devices. Overall, these results present significance for CVD graphene device engineering for nanoelectronics and spintronics.

Keywords: chemical vapor deposited (CVD) graphene, graphene electronics, graphene spintronics, charge transfer, high current density

*Do not attempt a takeoff before being
sure the flaps are down*

Peter J. Feibelman

List of Papers

This thesis is based on the following papers, which are referred to in the text by their Roman numerals.

I.   **Insights and Implications of Intricate Surface Charge Transfer and sp³-Defects in Graphene/Metal Oxide Interfaces**
Daria Belotcerkovtceva, Renan P Maciel, Elin Berggren, Ramu Maddu, Tapati Sarkar, Yaroslav O Kvashnin, Danny Thonig, Andreas Lindblad, Olle Eriksson, M Venkata Kamalakar
ACS Appl. Mater. Interfaces (2022) 14, 31, 36209–36216
DOI: 10.1021/acsami.2c06626

II.   **High current limits in chemical vapor deposited graphene spintronic devices**
Daria Belotcerkovtceva[1], J. Panda[1], M. Ramu, Tapati Sarkar, Ulrich Noumbe, and M. Venkata Kamalakar
Nano Research (2022)
DOI: 10.1007/s12274-022-5174-9
[1] co-first-authors

Reprints were made with permission from the respective publishers.

Comments on my own participation

The work behind research papers included in this thesis is based on collaborative teamwork. My contribution to Papers I, II included fabricating devices using nanofabrication techniques, performing high-precision electrical measurements, and characterization using Raman Spectroscopy, and Atomic Force Microscopy. In these papers, I was responsible for the analysis of the data, writing of the manuscripts, and contributing to defending the reviewers' comments.

Disclaimer: This thesis is written with the "we" personal pronoun in order to mean "me and the reader" or to refer to everyone in the field in general.

Extended bibliography

The following are publications to which I have contributed but are not research results in this thesis.

Experimental advances in charge and spin transport in chemical vapor deposited graphene
H Mishra, J Panda, M Ramu, T Sarkar, J-F Dayen, <u>Daria Belotcerkovtceva</u> and M Venkata Kamalakar
Journal of Physics: Materials (2021) 4 042007
DOI: 10.1088/2515-7639/ac1247

Highly-efficient growth of cobalt nanostructures using focused ion beam induced deposition under cryogenic conditions: application to electrical contacts on graphene, magnetism, and hard masking
Alba Salvador-Porroche, Soraya Sangiao, César Magén, Mariano Barrado, Patrick Philipp, <u>Daria Belotcerkovtceva</u>, M. Venkata Kamalakar, Pilar Cea and José María De Teresa
Nanoscale Advances (2021) 3, 5656-5662
DOI: 10.1039/D1NA00580D

Table of Contents

Chapter I
Graphene for nanoelectronics and spintronics

The discovery of two-dimensional (2D) materials opened up promising areas in fundamental research as well as application possibilities for nanoelectronics and spintronics. Graphene, the first material to be discovered in the 2D materials family, was experimentally isolated for the first time in 2004 by two researchers at the University of Manchester, Professors Andre Geim and Kostya Novoselov [1] *using the scotch tape method to peel layers from a lump of bulk graphite. Graphene offers high electron mobility and mechanical strength combined with transparency and flexibility. Following the initial promise, for scalability, several methods were explored, out of which, chemical vapor deposited (CVD) graphene stands out as a promising material with significant application potential. In this chapter, we will briefly discuss the uniqueness of graphene originating from its structure, how large-scale graphene is obtained by CVD methods, promising experiments in electronics and spintronics (such as ballistic transport and spin transport), and existing avenues/challenges in CVD graphene.*

1.1   Graphene: a unique two-dimensional material

Graphene is an atomically thin allotrope of carbon, where the carbon atoms are arranged in a hexagonal honeycomb lattice. This arrangement arises from the sp^2 hybridization of the carbon atoms. Graphene is the only atomically thin material (monolayer thickness ~3.35 Å) known till date that demonstrates a combination of high electrical and spin transport, thermal conductivity, mechanical strength, flexibility, elasticity, chemical stability, and a high optical absorption coefficient (2.3%). It provides outstanding possibilities in terms of its electrical properties that arise from the arrangement of carbon atoms in the layered structure allowing electrons to move freely at extremely high speeds without significant scattering. In fact, the history of graphene began more than half a century ago, when its electronic structure was first discussed by P.R. Wallace [2]. Its electrical properties can be related to its exceptional electronic structure. The honeycomb lattice of graphene is not a specific Bravais lattice, rather it can be represented as a combination of two sublattices: A and B (Figure 1.1a). The graphene hexagonal lattice can be described by the primitive translation vectors:

$$\vec{a_1} = \sqrt{3}a_0(\tfrac{\sqrt{3}}{2};\tfrac{1}{2}) \text{ and } \vec{a_2} = \sqrt{3}a_0(\tfrac{\sqrt{3}}{2};-\tfrac{1}{2}) \text{ (Figure 1.1 b)},\qquad (1.1)$$

where $a_0 = 1.421$ Å is the carbon-carbon bond distance. The reciprocal lattice is also hexagonal with the reciprocal lattice vectors:

$$\vec{b_1} = \tfrac{2\pi}{\frac{3a}{2}}(\tfrac{1}{2};\tfrac{\sqrt{3}}{2}) \text{ and } \vec{b_2} = \tfrac{2\pi}{\frac{3a}{2}}(\tfrac{1}{2};-\tfrac{\sqrt{3}}{2}) \text{ (Figure 1.1c).}\qquad (1.2)$$
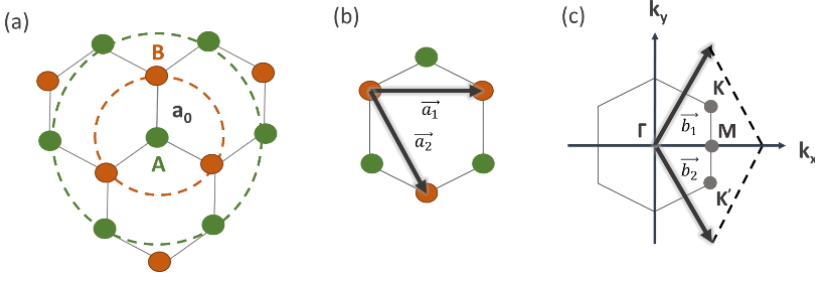
Figure 1.1. (a) Scheme showing graphene lattice, with the carbon atoms of the two sublattices (A and B) marked in green and red, respectively. The carbon-carbon bond distance is a_0. (b) The primitive unit cell of graphene showing the primitive translation vectors, a_1 and a_2. (c) Scheme showing reciprocal lattice of graphene (also hexagonal) with the reciprocal lattice vectors, b_1, and b_2. High symmetry points are labeled as K, M, and K'.

Thus, the graphene band structure can be calculated by the first-nearest-neighbor simple tight-binding model using only out-of-plane orbitals. The approximation considers only hopping between nearest-neighbor atomic sites since higher-order hopping terms are significantly smaller and can be neglected. This gives rise to two independent points per Brillouin zone, K and K'. In the valleys, the valence and conduction bands touch at K and K'. The energy spectrum of electrons in graphene can be described by the following equation:

$$E_\pm(\vec{k}) = \pm t\sqrt{1 + 4\cos\left(\frac{3k_xa}{2}\right)\cos\left(\frac{\sqrt{3}k_ya}{2}\right) + 4cos^2(\frac{\sqrt{3}k_ya}{2})}, \qquad (1.3)$$

where $a = \sqrt{3}a_0$ and t is the transfer integral between first-neighbour π-orbitals (nearest neighbor hopping energy).

Here, unlike the parabolic dispersion for semiconductors, at low energies graphene shows a linear energy relation

$$E_k = \pm\hbar v_F|k|, \qquad (1.4)$$

where reduced Plank constant ($\hbar$), Fermi velocity (v_F) $\sim 10^6\ m/s$, wave vector (k) Graphene emerges as a semimetal (a semiconductor with zero bandgap), where the electron/hole dynamics is described not by the Schrödinger equation, as in bulk semiconductors, but by the Dirac equation for massless quasiparticles. Graphene electronic linear dispersion with ambipolar functionality [2] leads to charge carriers having very high mobility and carrier tunability with an external electric field. Besides, the two gapless bands touching at the Dirac points K and K' makes graphene capable of conducting electricity even at the limit of nominally zero carrier concentration. That can be observed because of electron propagation along carbon atoms, where interaction appears with the periodic potential of the graphene honeycomb lattice. Although a minimum conductivity at the neutrality point has been theoretically predicted for Dirac electrons in graphene in the ballistic regime with a value of $4e^2/\pi h$ [3], the origin of the observed minimum conductivity and its interplay with a disorder in diffusive devices has

fueled both theoretical and experimental debate. Once again, owing to the A and B sublattices, electrons/holes in graphene acquire an additional degree of freedom, called pseudospin. This leads to a series of remarkable quantum transport phenomena such as anomalous integer quantum hall effect [4], [5], fractional quantum Hall effect[6], and Klein tunneling [7]. Furthermore, at room temperature, graphene shows high-quality carrier transport, that results in the observation of micrometer ballistic transport lengths [8]. Apart from the charge transport, graphene also shows an ultimate promise for the transport of spin-polarized electrons, for graphene spintronics. The intrinsic weak spin-orbit coupling[9], and negligible hyperfine interaction[3] in graphene make it an ideal medium for transporting spin-polarized currents, with a predicted spin diffusion length ~100 μm at room temperature [10]. Fascinatingly, the room temperature charge and spin transport phenomena such as field effect tunability, ballistic transport [11], and longest spin transport [12] can be realized in large-scale graphene such as CVD graphene. In particular, the ballistic and spin transport phenomena allow for the practical potential of graphene in graphene nanoelectronics and spintronics.

1.2   Synthesis methods

In the laboratory, graphene can be readily obtained by mechanical exfoliation of graphite crystals using scotch tape. This technique is still the most widely used method to obtain high-quality graphene flakes, that have been employed to investigate quantum and spin transport in graphene and its heterostructures with other crystals. More recently, a rapid interest in graphene-based applications and a focus towards translational research have propelled the need for exploring other methods for graphene isolation and synthesis. Below, we describe a few key methods for graphene synthesis.

Mechanically exfoliated graphene. Physical methods allow for the production of high-quality graphene on a laboratory scale. The mechanical exfoliation method is quite simple and can be used for all 2D materials where the atomic layers are weakly coupled in the respective bulk crystals. The first graphene sample was obtained by Novoselov and Geim using such a technique [1]. Homogeneity and high crystallinity are the key factors for selecting graphite sources such as natural graphite, kish graphite, or highly oriented pyrolytic graphite (HOPG). Despite the low yield, low productivity, and small crystal sizes (few μm), this method remains the most reliable method for obtaining high-quality single crystalline samples with record carrier mobility suitable for electrical transport measurements on the laboratory scale.

Large-scale graphene. Realizing large-scale graphene industrially can become a golden approach to translating graphene research into applications. Large-scale synthesis of graphene is mainly achieved via two routes, namely epitaxial growth and CVD growth. Epitaxial growth involves obtaining graphene on the surface of silicon carbide (SiC) by sublimation of Si atoms from its surface. Since to the graphene layers obtained here are an intrinsic part of the substrate (the top layer of the substrate with the So atoms removed), this form of graphene cannot be easily transferred to a different substrate. In contrast, CVD growth allows us to obtain graphene with bigger crystals and high mobility on chosen substrates for use in laboratories as well as potential industrial applications. This idea originated from the work published by Ruoff's group in 2009 [13] and was then developed further in the subsequent reports demonstrating the roll-to-roll production method [14], [15]. Nowadays, commercial graphene with a size of up to 8×8 cm^2 produced on a metal substrate and then transferred onto a SiO$_2$/Si wafer or quartz glass

are available from several companies (Graphenea Inc., ACS Material), and these demonstrate mobility suitable for electrical measurements and exploration of applications in electronic, photonics or batteries.

Graphene composites synthesis for non-electrical applications. Plenty of applications do not require high-quality samples, the more important is mass production which can be achieved by chemical methods. The principle is the intercalation of graphite with surfactants, which have higher energy of interaction with graphene layers than the van der Waals forces between the layers. After intercalation, the distance between the layers increases, which allows mechanical treatment (sonication and centrifugation) on the graphite to separate the layers. Another way is graphite exposed to a mixture of sulfuric and nitric acids, followed by oxidation, and carboxyl groups of graphene appear at the edges of the sample [16], [17]. Then, graphene layers can be formed under the reaction with octadecylamine ($C_{18}H_{39}N$) in solutions of tetrahydrofuran (C_4H_8O), carbon tetrachloride (CCl_4), and dichloroethane ($C_2H_4Cl_2$) with a thickness of 0.54 nm. Also, graphene films can be synthesized by reducing a monolayer graphite oxide film followed by annealing in an argon/hydrogen mixture [18]. However, the quality of graphene obtained by such chemical methods is low due to the incomplete removal of various functional groups.

1.3 Chemical Vapor Deposited (CVD) graphene

1.3.1 CVD synthesis

One of the most prominent industrial methods for large-scale synthesis of graphene is chemical vapor deposition (CVD). Since 1976, this has been widely used for the synthesis of graphite samples [19], and the technique was later modified for the growth of graphene. CVD synthesis (Figure 1.2a) requires a mixture of carbon-containing gas such as methane (CH_4) [20], [21], ethylene (C_2H_4) [22], [23], or, the more recently used CO[24], followed by hydrogen (H_2), and argon (Ar) at various pressures (from a few fractions of a millitorr to atmospheric pressure) (Fig. 1.2). Decomposition into carbon and components occurs on precursor substrates (such as nickel or copper) at temperatures below 400°C. Carbon atoms start getting deposited on the nickel substrate as the temperature increases, starting from 650°C. At temperatures above 800°C, carbon begins to diffuse into nickel. The heating is continued till a maximum temperature of 950-1000°C [25]. When cooled down to room temperature, the crystal lattice of the metal compresses carbon atoms to the surface (due to thermal compression)). This leads to the formation of a graphite-like structure due to similar values of the lattice constant of nickel (or copper) and graphene. Large-scale graphene is routinely synthesized using CVD in laboratories and is being sold by several companies today across the world (Figure 1.2b).
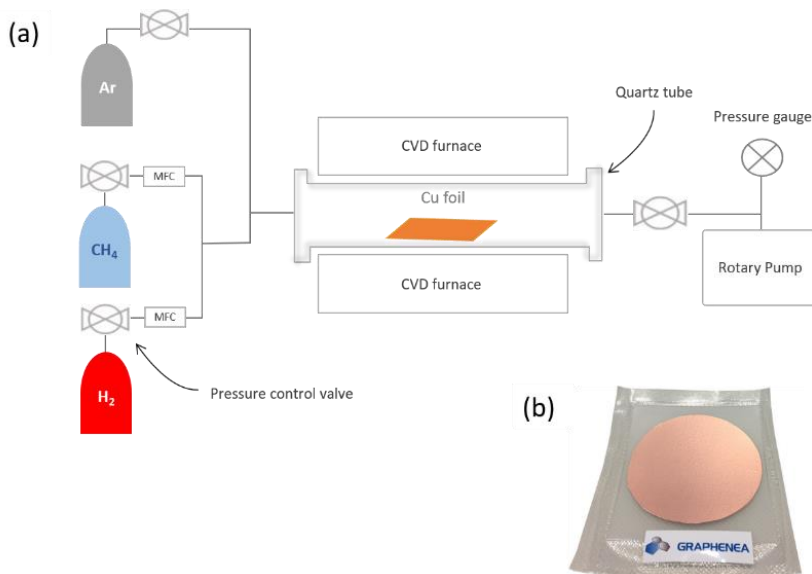
Figure 1.2. (a) Schematic diagram of CVD set-up for the synthesis of graphene using CH_4 and H_2 (MFC: mass flow controller). (b) CVD graphene on a copper substrate from Graphenea Inc.

1.3.2 Current state-of-the-art: nanoelectronics and spintronics

Interest in graphene for electronic applications has grown due to its high mobility and unique mechanical properties, which make it a suitable candidate for transparent conductive films (TCFs) and implementation in the semiconductor industry. Indeed, the increased surface-to-volume ratio (compared to bulk materials) promotes the use of graphene as effective Hall sensors [23–25] and bio- or chemical sensors [29]–[32] with better performance than compounds based on III-V semiconductors. In practice, the fabrication of graphene-based sensors involves an encapsulation step realized by stacking Al_2O_3 [33], h-BN [34], etc. to protect against environmental contamination.

Significant progress has been made in graphene nanoelectronics. The development of field-effect transistors based on graphene began simultaneously with its production. The first graphene field-effect transistor (GFET) was fabricated in 2004 on a SiO_2/Si substrate [1], where a 300 nm thick silicon dioxide film served as the gate dielectric. The heavily doped silicon substrate acted as the bottom gate of the transistor, modulating the conductivity of the graphene channel. The first graphene-based top gate transistor was manufactured in 2007 [35]. Despite the reduction in electron and hole mobility compared to bottom-gate GFETs, top-gate GFETs could still compete with reliable mobility values. Besides, the resistive switching behavior mechanism due to charge trapping observed in GFETs allows the fabrication of transistor-based memory devices [36]. Further, the possibility of large-scale production makes CVD graphene a frontrunner as the basic material for nanoelectronics. The sensitivity of graphene to the choice of substrate and external conditions has been seen to have a large impact on the charge mobility values. Polymer-supported wet transfer or dry transfer methods are used for CVD graphene

transfer, and the transfer method can also have an impact on the electrical properties of graphene. The carrier mobility of graphene obtained on SiO_2/Si substrate via polymer-assisted transfer exceeds 7000 $cm^2V^{-1}s^{-1}$ [37] at room temperature, whereas for graphene obtained on h-BN substrate, the value of the mobility exceeds 37000 $cm^2V^{-1}s^{-1}$ at 4.2 K [38]. State-of-the-art mobility value of 3000000 $cm^2V^{-1}s^{-1}$ was achieved in graphene at low temperatures by the combination of dry transfer and subsequent h-BN encapsulation (Figure 1.3a) [11]. Most of the commercially available large-scale CVD graphene demonstrate mobility values in the range of 2000 – 4000 $cm^2V^{-1}s^{-1}$. These developments have allowed the observation of ballistic transport with the unimpeded motion of electrons in graphene, observed upto 1 μm at room temperature. In order to detect ballistic transport, current applies between two neighboring electrodes which causes voltage drop on opposite remaining contacts (as shown in Figure 1.3b). The estimated negative bend resistance (due to an out-of-plane magnetic field) is a signal of ballistic transport along the graphene channel. Demonstrating such a regime is possible on a sample with high charge carrier mobility and concentration [39].
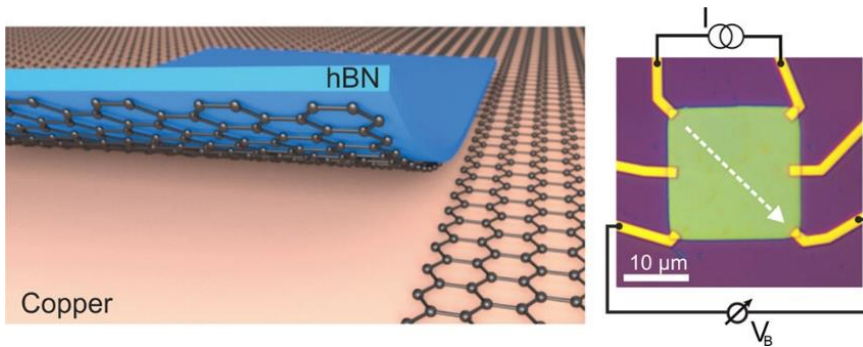

Figure 1.3. (left) Scheme of stacking graphene on hBN layer from copper foil. (right) Optical image of the device for ballistic transport measurements [11].

2D materials due to their atomically thin nature present new prospects for spintronic devices such as magnetic memory and magnetoresistive random-access memory (MRAM) [40], [41]. Due to the low spin-orbit coupling of light carbon atoms in graphene and negligible hyperfine interaction, graphene was proposed as a suitable material for the basic ferromagnet-nonmagnet-ferromagnet layer structure in spin-valve devices [42]–[45]. Long spin diffusion length (λ ~100 μm) and high spin lifetime (τ ~1 μs) in graphene were theoretically predicted in 2006[9]. A year later, spin transport in a graphene channel was demonstrated for the first time using a non-local measurement technique, with spin precession across a channel length of ~2 μm, thus, surpassing the capability of any other material (where spins travel ~100 nm) at room temperature [43]. Further, there was increased research exploring ways to enhance spin transport in graphene by improving the quality of contacts and graphene. The implementation of hBN as a tunnel barrier reveals efficient spin injection as well as graphene encapsulation with achieved values of spin diffusion length λ_s ~12 μm and τ_s ~2 ns at room temperature [46]. There has also been increased interest in polycrystalline CVD graphene that allows large-scale device fabrication. Despite enhancements in device performance using special encapsulated structures [47], [48] and tunnel barrier implementation [49], routine devices based on CVD graphene grown on widely used substrates such as oxidized silicon

wafers still show values of λ_s ~1.5 μm and τ_s ~150-200 ps [50], [51]. Nevertheless, large values of λ up to 10 μm was observed in flexible CVD graphene spin circuit [52]. Despite the higher roughness of large-scale flexible polyethylene naphthalate (PEN) and imperfect graphene crystal structure, effective spin transport has been demonstrated in CVD graphene [12]. In fact, such system provide reasonably decent quality electrical transport[53], [54] and opportunities for new processing methods such as direct lamination[55]. In Table 1.1, we present a list of reports that display high-quality charge transport and spin transport in CVD-grown graphene. Thus, research in device physics has shown that CVD-graphene-based devices can demonstrate high field-effect mobility, ballistic transport, and high-quality long-distance spin transport. The realization of quantum electrical and spin transport in large-scale graphene can lead to applications in nanoelectronics and spintronics ranging from memristors, single-electron transistors, tunnel field-effect transistors, and graphene spin valves. As discussed later in this thesis, the properties of graphene are sensitive to adjacent materials and measurement conditions. Such modulation of properties can have new implications for developing unique interfaces in new graphene-based resistive switching and spintronic devices.

Table 1.1 State-of-the-art charge and spin transport parameters obtained for CVD graphene: ballistic transport (ballistic mean free path λ_{mfp}) and spin transport parameters (spin diffusion length λ_{sd}, diffusion constant D, spin lifetime τ) including mobility (μ) and temperature (T).

	System	Ref.	Mobility (cm^2 V^{-1} s^{-1})	Temperature (K)	τ (ns)	D (m^{2}s^{-1})	λ (μm)
Ballistic transport	Single layer and bilayer graphene onto SiO$_2$/Si substrate	[56]	1 400 (SLG) 2 100 (BLG)	5-250	-	-	λ_{SR} = 1.35
	Few-layer graphene-hBN heterostructure	[57]	20 000	300	-	-	λ_{SD} = 10
	CVD graphene dry transferred onto h-BN flakes	[58]	μ_h=42 000 μ_e=29 000	4	-	-	$\lambda_{ballistic}$ = 1
	CVD bilayer graphene-h-BN heterostructure	[59]	180 000 40 000	2 300	-	-	λ_{mfp} = 2
	h-BN encapsulated single-layer CVD graphene	[60]	70 000 120 000	300 9	-	-	λ_{mfp} = 0.6 λ_{mfp} = 1
	CVD graphene/h-BN heterostructure	[61]	μ_h = 110 000 μ_e = 145 000	1.6	-	-	-

		h-BN-stack	[62]	18 000-21 000	300	-	-	30.4
		Co/TiO$_2$	[12]	2 000-3 000	300	0.260	0.0055	1.2
		Co/TiO$_2$	[63]	2 000	4.2–300	1.2	0.026	6
		Co/MgO	[64]	1 400 (SLG) 2 100 (BLG)	5 - 300	0.18	0.007	1.1
		Co/TiO$_2$	[65]	2 000	300	0.405	0.032	3.4
		Co/TiO$_2$	[66]	1 700	300	3	0.028	9.2
		Co/h-BN	[67]	850	4.2–300	0.260	0.0055	1.2
		Co/h-BN	[47]	3 400	300	0.404	0.03	3.5
		Co/MgO/ h-BN	[68]	20 000	300	2.2	-	1.75
	CVD bilayer graphene	Co/Al$_2$O$_3$	[69]	24 000	300	5.8	-	26

Spin transport — *CVD graphene*

19

1.3.3 Technological challenges in large-scale implementation

The possibility to transfer graphene onto a substrate of choice, tuning charge carrier density via the back gate voltage as well as the low production cost are strong advantages of CVD graphene, which makes it preferable for large-scale fabrication. However, such a growth technique also gives rise to unwanted structural features such as wrinkles and grain boundaries. Besides, the transfer technique can induce defects in the monolayers including holes, cracks, and wrinkles. Despite this, commercially obtained CVD graphene (such as from Graphenea Inc.) with a polycrystalline structure has shown high-quality electrical and spin transport properties. The device fabrication process consists of several steps that introduce defects, impurities, and interfaces with other materials such as metal oxide layers, and require optimizations for high reproducibility. A major concern in device performance is related to deformation and structural modification due to interfaces, an understanding of which can lead to better control over the properties. Furthermore, the performance of the as-fabricated device varies with the number of operations. This means that we need to understand both fundamental issues and performance limits, critical to the exploitation of large-scale graphene for technology in 2D electronics and spintronic circuits.

1.3.4 Understanding fundamental issues and limits

The aforementioned high-quality developments (Table 1.1) in charge and spin transport have been realized in large-scale chemical vapor deposited (CVD) graphene, making it prospective for practical implementation in future quantum and spin-integrated circuits [70]. Metal oxide interfaces are essential to graphene nanoelectronics and spintronic applications, particularly for planar and vertical graphene spintronic devices [41], [71]. Ultrathin layers (~nm) of metal oxides serve as tunnel barriers offering optimum interface resistance to overcome the conductivity mismatch problem associated with electrical spin injection [49], [72], [73], which is necessary to reduce interface spin back-scattering. Titanium and aluminum oxides have been used as tunnel barriers in graphene spintronic devices, primarily due to their ease of deposition. Although ultrathin metal oxide layers can be directly realized using atomic-layer deposition (ALD) or sputtering techniques, these can lead to many defects, a source of short-range scattering [74], which makes them less compatible with spintronic device fabrication processing. Therefore, Ti or Al are first deposited using electron beam evaporation in graphene spin devices and are then oxidized with contact to air/O_2. Earlier experimental observations have shown that while spin lifetimes ~1 ns and long spin diffusion lengths ~ 10 μm can be attained using TiO_x barriers [63], [66], [75], the AlO_x-based devices show lower spin lifetimes ~100 ps [43], [76], [77]. These earlier and more recent studies [78], [79] with AlO_x barriers fabricated on graphene by sputtering as well as molecular beam epitaxy confirm this observation and attribute the lower spin lifetimes due to the formation of pinholes. On the other hand, extremely long-distance spin communication and ultimate spin currents have been achieved even in commercially available graphene with mobility μ ~2000-3000 $cm^2V^{-1}s^{-1}$ using titanium oxide tunnel barrier contacts[75]. Given the different responses of different metal oxide layers, understanding the intricacies of metal oxide-graphene interfaces requires more in-depth study and analysis.

Apart from investigating the behavior of graphene/metal oxide interfaces in a normal operating regime, it is also necessary to explore the sustainability of graphene-based devices. Knowing the stability and performance of graphene nanodevices under the

influence of high currents is crucial for their use in spin transport applications. Mechanically exfoliated few-layer graphene nanoribbons from Kis graphite have shown a breakdown current density of the order of ~10^8 A/cm^2 [80]. A similar result was reported for bilayer graphene under current stress with a breakdown current density of ~10^8 A/cm^2 [81]. However, these reports are for graphene samples produced from highly oriented pyrolytic graphite, which have size limitations and are not suitable for large-scale applications. As discussed before, for large-scale applications, CVD graphene is a promising candidate. Studies on CVD graphene under current stress report a breakdown density of ~4×10^7 A/cm^2 [82]. However, there is a lack of sufficient evidence of the actual current-carrying capacity of monolayer CVD graphene.

Solving interface-related issues and determining its ultimate capabilities are fundamental research problems for unleashing the full potential of CVD graphene for applications. Understanding the effects of oxidation, charge transfer, and defect formation in graphene-metal oxide layers is essential to control and enhance the performance of graphene nanoelectronic and spintronic devices. Moreover, such insights will allow new applications of graphene in memristive devices. An increase in current densities and thermal stress of interconnects due to device miniaturization and circuit size reduction bring in new challenges for integrated circuit designs that need to be resolved.

Chapter II
Experimental methods

In this chapter, we will discuss the experimental methods employed to characterize graphene samples, fabricate devices, and perform electrical measurements in graphene-based devices. In this work, we have utilized CVD graphene as the starting material, which was characterized spectroscopically by Raman spectroscopy to determine the quality of graphene, defect density, and doping type. To determine the sp^3-sp^2 bonding and metal oxidation states, we employed X-ray photoelectron spectroscopy. Nanodevices of CVD graphene were fabricated by photolithography, reactive-ion-etching, electron beam lithography, and metal evaporation techniques followed by the lift-off technique. Finally, electrical characterization of contacts and channels was performed by dedicated three-probe and four-probe direct current transport measurements. Measurement configurations and regimes of electrical measurements, and associated analysis are also elaborated.

2.1 Characterization techniques

2.1.1 Optical characterization

Each step in the fabrication process requires verification using optical microscopy. The optical characterization was done using a Nikon Eclips L200ND optical microscope in the cleanroom. Optimum contrast was achieved by filter under the x50 and x100 objectives and atomically thin graphene can be imaged on SiO_2 (280 nm)/Silicon substrate due to Fabry–Perot interference conditions.

2.1.2 Raman spectroscopy

The most informative and non-destructive method for studying carbon-based materials is Raman spectroscopy. Raman spectrum gives the finger print of carbon-based nanomaterials such as graphite, carbon nanotubes, and graphene. The Raman effect consists of elastic and inelastic scattering of incident rays when an object is irradiated with monochromatic optical radiation. The spectra are very sensitive to the nature of chemical bonds - both in organic molecules and polymeric materials, as well as in inorganic crystal lattices and clusters. Apart from its non-destructive nature, Raman spectroscopy enables the possibility for non-contact quality analysis and no need for sample preparation such as transfer to the specific substrate or fabricating a protective layer. It provides information about changes in the structure after manipulations like doping or defects.

Due to the linear dispersion dependence of the electron energy near the K and K' points of the Brillouin zone for graphene, the Raman scattering effect is resonant at any optical excitation. The choice of laser wavelength for the study of nanocarbon materials is a key factor since the graphene samples of interest are usually microscopic. In addition, there is the influence of the substrate. The most common substrates are Si and SiO_2, which can exhibit fluorescence with near-infrared (NIR) lasers such as 780 and 785 nm. To prevent peak overlap, visible lasers are generally recommended, usually a laser with a wavelength

of 633 or 532 nm [83]. In addition, the laser power needs to be monitored and adjusted in small steps. In this way, temperature effects can be controlled, and the Raman signal can be maximized, avoiding heating or damaging the sample.

In a typical Raman spectrum of graphene, there are 3 peaks: 2D, G, and D peaks (Figure 2.1). Graphene is usually characterized by one sharp and symmetrical peak in the 2D band, which makes it different from other carbon-based nanomaterials. Despite their simplicity, the spectra of graphene contain a large amount of information about the quality and the microstructure of the sample. That information is usually extracted from the position of the characteristic peaks, the shape of the peaks, and their intensity (or relative intensity).

The information that can be extracted from the Raman spectra of graphene is summarized below:

- o The G-band is generally located near 1582 cm^{-1} and characterizes graphene in the plane of the sp^2 vibrational mode - this parameter reflects the degree of crystallization of the material. This peak is observed in various carbon-based compounds such as amorphous carbon, glassy carbon, graphite, as well as graphene. Besides, the position of this peak is sensitive to doping. The sensitivity of the G peak to the type of conductivity of graphene and carbon nanotubes is related to the adsorption of electron-donating and accepting molecules as a shift in frequency.

- o The D-band is usually located near 1350 cm^{-1} and reflects the degree of structural disorder near the edge of the microcrystalline structure, which reduces the symmetry of the structure. The ratio of the intensities of the Raman peaks of the two bands (I_D/I_G) can be used to estimate the degree of disorder of the material[84] and to calculate the concentration of defects in the material. The absence of the D-band indicates the superior quality of the sample.

- o The 2D band is near 2700 cm^{-1} (depending on the wavelength of the excitation source) and relates to the number of graphene layers in the material[85].
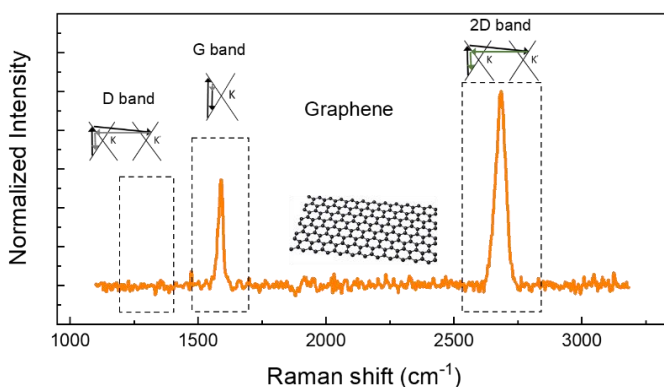

Figure 2.1. Typical spectrum of CVD graphene showing G and 2D band with absent D band for high-quality sample. Each band has the following explanation of excitation in reciprocal space.

23

- For qualitative analysis, the 2D to G peaks ratio is used; for monolayer graphene, the ratio is ≥ 2, which is seen in high-quality chemical vapor deposited (CVD) graphene. Although CVD growth results in polycrystalline graphene with a large number of grain boundaries, the 2D to G peak intensity ratio is about 2, and the presence of a defect peak (D-band) is not observed.

- The peak intensities ratio of the D band to G band (I_D/I_G) is inversely proportional to the crystallite size (L_a) of the graphene sample, i.e., $\frac{I_D}{I_G} \sim \frac{1}{L_a}$ [86].

- A remarkable feature of the Raman spectrum is the strong dependence of the I_D/I_G ratio on the laser excitation energy E_l used in the experiment, i.e., $\frac{I_D}{I_G} \sim E_l$ [87]. Therefore, to ensure that any changes in the peak intensity ratio are only due to changes in the sample, we have kept the laser excitation energy constant for all Raman experiments.

2.1.3 X-ray Photoelectron Spectroscopy (XPS)

X-ray photoelectron spectroscopy (XPS) is one of the widely used techniques to study the surface and interfaces of materials. Here, 2D material especially graphene provides an opportunity for XPS due to atomic thickness limitations. In particular, for graphene and other 2D materials, it has been utilized successfully to estimate the elemental composition, chemical and electronic state of atoms on the surface. XPS is based on the photoelectric effect (described in 1905 by Albert Einstein). The escape of an electron from the surface of a material to a free-electron-like state is governed by the energy conservation law:

$$E_{binding} = E_{photon} - (E_{kinetic} + \phi), \qquad (2.1)$$

where $E_{binding}$ is the binding energy of the electron measured relative to the chemical potential, E_{photon} is the energy of the incident X-ray photons applied in an experiment, $E_{kinetic}$ is the kinetic energy of the electron as measured by the instrument, and ϕ is a work function-like term for the specific surface of the material, which in real measurements includes a small correction to account for the instrument's work function because of the contact potential.
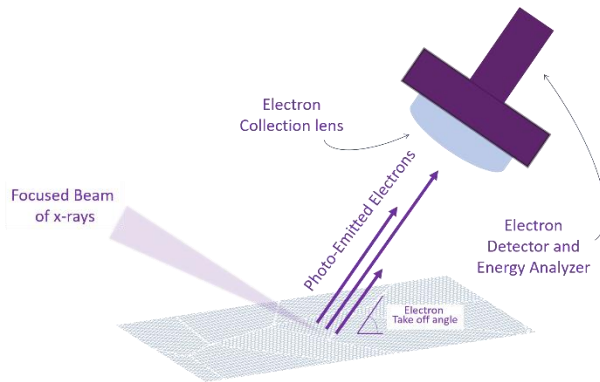

Figure 2.2. Schematic representation of an XPS system.

The procedure of measuring XPS spectra includes irradiation of the graphene sample with an X-ray beam and the recording of the dependence of the number of emitted electrons as a function of their binding energy. Electrons are emitted over the entire penetration depth of the soft X-ray radiation used in the study (Figure 2.2). However, due to the strong absorption of the emitted electrons by the bulk material under study, XPS provides information only about the uppermost (approximately 10–30) atomic layers of the sample.
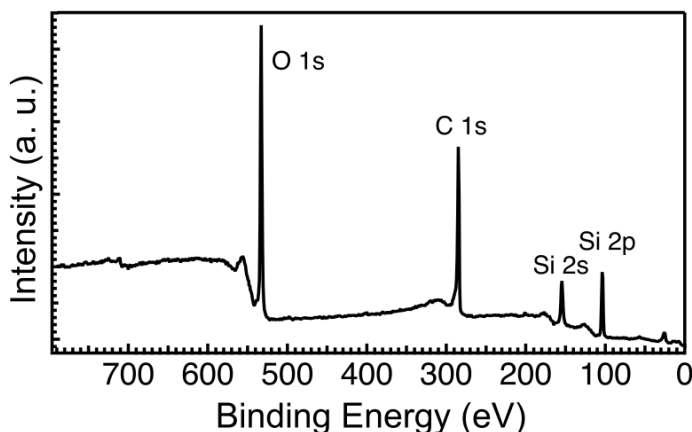

Figure 2.3. Typical X-ray photoelectron spectrum of graphene.

A typical X-ray photoelectron spectrum of graphene on Si/SiO_2 is presented in Figure 2.3, where peaks can be fitted to determine the composition and states of graphene and stacked materials. For defect estimation, the C 1s spectra were calibrated and fitted with a set distance of 0.7 eV between sp^2 (284.4 eV) and sp^3 (285.1 eV) peaks [1]. The binding energy of the O 1s spectrum for the pristine graphene sample was calibrated with the SiO_2 component at 533.1 eV, as this sample showed some charging during XPS measurement [2]. Further, the investigation of ultra-thin TiO_x and AlO_x on graphene requires estimation of stoichiometry using the equation:

$$I=n \cdot SF, \qquad (2.2)$$

where I is the intensity of peak, n is atomic concentration, and SF is the sensitivity factor. The sensitivity factors are acquired from the overview spectra using the software Multipak.

2.1.4 Atomic Force Microscopy (AFM)

Atomic force microscopy (AFM) is widely used to obtain atomic resolution topographic images of samples by a sharp tip (a sharpened cantilever) that is brought close to a sample (Figure 2.4). Thus, atomic forces are used to map the tip-sample interaction at a subnanometer distance (shown in the Force-distance curve in Figure 2.4). As a result, the tip scans over a surface using a feedback loop to adjust the parameters needed to image a surface. There are two modes of operation. The first mode consists of moving the probe keeping the tip-sample distance unchanged. Changing the distance between the tip and

the sample surface gives a change in the interaction force between the sample and tip. In the second mode, the force value is kept constant, and the height position of the tip changes. As the tip gets closer to the surface, increasingly repulsive force takes over and causes the cantilever to move away. The position of the plate is recorded using electrical and optical methods. Scanning is carried out by non-contact methods and by contact when the probe is at a distance of 5-15 nanometers. The vertical position (z-ax) is controlled by an interference pattern produced by a laser beam. Positioning and scanning (x-y plane) of the surface are carried out by electric motors and detectors. These techniques are extremely useful to both characterize graphene morphology and the roughness of the evaporated materials on top of it, as we used it in our work.
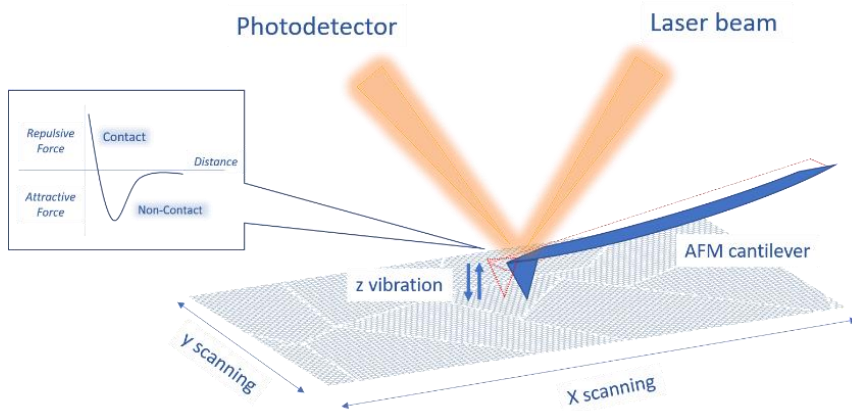

Figure 2.4. Schematic diagram of an atomic force microscope (AFM).

2.2 Device fabrication

For all basic electrical characterization of graphene and graphene/metal oxide interfaces, one type of device was fabricated, which consists of a graphene channel, six contacts deposited on it, and a back gate electrode. The multiple contacts allow for measuring in 2T, 3T, and 4T configurations by applying a gate voltage and gives us more freedom to use different channels on a single device (Figure 2.5a).

The fabrication starts with the patterning of the back gate electrode on a 4-inch silicon wafer (Si p/n doped (500 μm) covered with SiO_2 (285nm)). After cleaning the wafer with the acetone, hexamethyldisilazane (HMDS) primer and S1813 resist were spin-coated on the top side of the silicon wafer to protect the top side. HMDS primer is widely used to promote the adhesion of graphene to silicon surfaces. Next, the substrate was dipped in buffered HF solution to etch silicon dioxide from the bottom layer. The buffered hydrofluoric acid (BHF) (or buffered oxide etch (BOE)) etches approximately 0.8 μm SiO_2 in 10 min. For the 285 nm oxide layer, the substrates were dipped in BHF for at least 3 min 40 sec, followed by rinsing with bubbled water for 1 min. The metals were then evaporated onto the bottom layer using e-beam evaporation in the following multilayer structure: Ti (5 nm)/Cu (50 nm)/Au (10 nm). Next, the spin-coated resist and primer were removed using acetone at 70°C. After this step, the wafer was sent to Graphenea.Inc for transfer of the entire top surface of the wafer with polycrystalline CVD graphene grown on Cu. After receiving the wafer back from Graphenea, we spin-coated the S1813 resist

to protect the graphene and we used the dicing saw to cut a 4-inch silicon wafer into ~ 0.5 cm^2 sized chips.

On this chip, we fabricated 50 devices (an image of one device is in Figure 2.5b). Optical lithography is an optimal and less time-consuming tool to fabricate arrays of graphene channels. First, the chip was cleaned in acetone solution for 7 min at 70°C to remove the resist which protected the graphene during the dicing process, and rinsed with isopropanol alcohol (IPA). Next, photo-resist S1813 was spin-coated (60 sec – 3000 rpm – 1000 rpm/s) and baked at 90 °C for 120 s. The following two steps are required for optical lithography: removing resist completely at the edges and forming the channel. To remove the edges a square shape physical mask was used for 50 s of exposure time in soft contact mode because it does not require high precision. The alignment was made using an optical microscope on marks evaporated during the wafer preparation step. The developing process was performed using solution Microposit 351 Developer and water (1:4) for 50 s and in water (1 min). To form channels, the shadow mask consisted of 50 stripes with a width of 5 μm and length of 40 μm. The developing process was the same as the one used for removing the edges. The chip was then etched in a vacuum chamber using RIE to remove organic leftovers by oxygen plasma treatment (50W, 45 sccm) for 55 s. The final step of channel formation was cleaning the substrate using hot acetone.

There are several important requirements for electrodes. Since the devices are meant to be used for charge and spin transport measurements, the width of contacts on top of the graphene channel is narrow 150-250 nm connected with big square electrodes 150 μm ×150 μm in size. To achieve such resolution, electron beam lithography (EBL) with 80 keV was used for fabricating patterns. There are two typical EBL resists, MMA EL 9 and ARP, which were spin-coated (60 sec – 6000 rpm – 1000 rpm/s) and subsequently baked at 135°C for 10 min. Two layers allow making a sharp-cut of patterns with different widths to allow easier lift-off. An e-beam exposure was carried out to expose the desired patterns, square electrodes exposed at low current (0.7 nA) and electrodes at high current (3.5 nA). Finally, the patterns were developed in hexyl acetate (33 s), MIBK/IPA (1 min 15 s), and IPA (1 min). In the next step, electrodes consisting of a multilayer structure of (TiO$_x$ (0.8 nm)/ Co (60 nm)/ AlO$_x$ (3 nm)) were deposited using the standard e-beam evaporation method on the developed pattern. After the evaporation, a gentle lift-off process in hot acetone was performed. For devices using SiO$_2$/Si as substrate, electrical connection is usually made by wire bonding. All fabrication steps described in this section are presented in Figure 2.6.
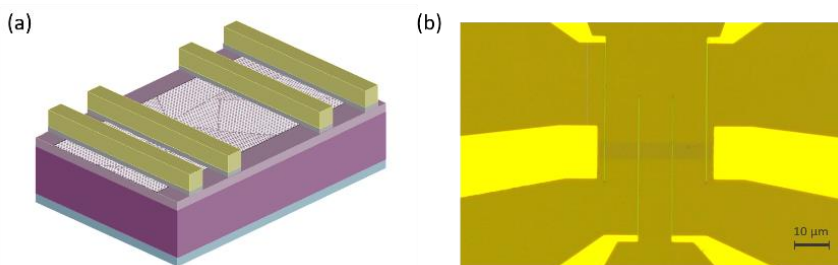

Figure 2.5. (a) Schematic of the graphene-based device on Si/SiO$_2$ substrate with multilayer contacts [TiO$_x$ (0.8 nm)/ Co (65 nm)/ AlO$_x$ (5 nm)]. (b) Optical image of CVD graphene on SiO$_2$/Si substrate with Co/TiO$_2$ tunnel contacts.
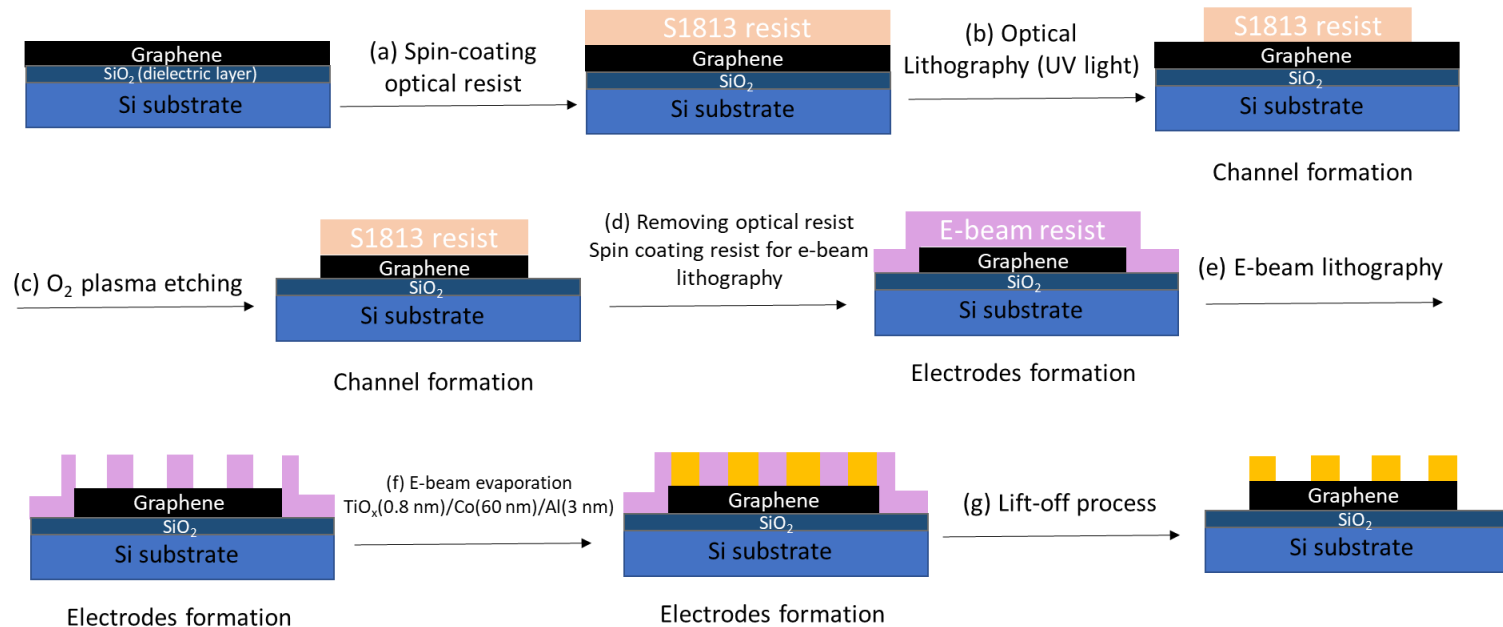
Figure 2.6. Schematic illustration of fabrication process and device architecture for graphene-based devices.

2.3 Electrical characterization

2.3.1 Basic I-V characterization

The I-V curve (or current-voltage characteristic curve) is a graphical representation of the relationship between the applied voltage across an electrical device and the current flowing through it. The I-V curves are widely used to ascertain the functionality of a device as well as basic material properties. Different measurement configurations yield different shapes of the I-V curves, as explained below.

Two-terminal (2T) measurements

The first electrical characterization of the measurements was performed with 2T measurements, where only two contacts of the device are connected to the current source and voltmeter (Figure 2.7a). Such configuration allows us to choose the working contacts. However, this method is not appropriate to extract reliable device parameters. This is because, in 2T measurements, the effect of contact resistance is also included. If we assume that the voltage drop across both graphene-contact interfaces is similar, then the measured voltage drop (V) is given by:

$$V = V_{graphene} + 2V_{contact} = \left(R_{graphene} + 2R_{contact}\right)I, \qquad (2.3)$$

where $R_{graphene} = \frac{\rho L_{ch}}{W_{ch}}$ is graphene resistance (ρ – resistivity, L_{ch} – channel length, W_{ch} – channel width) and $R_{contact} = \frac{\rho_c}{A}$ is contact resistance (ρ_c – contact resistivity, A – area under the contact). In the resulting I-V curve, we can see a combination of linear and tunneling behavior (Figure 2.7b).

Three-terminal (3T) measurements

To characterize the graphene-metal interface, 3T configuration is used. Here, two contacts are connected to the current source and voltmeter each, with only one contact being connected to both (Figure 2.7c). The main difference with the 2T configuration is that there is only one common contact in the 3T configuration. In our devices, the graphene is in contact with TiO_x (0.8 nm)/Co (65 nm). The ultra-thin metal oxide layer (TiO_x) is introduced in the graphene-metal interface to improve the performance of spin-valve devices by decreasing conductivity mismatch between the layers. However, tunneling behavior still exists in the I-V curves recorded using 2T and 3T measurement configurations, which can be understood in terms of metal-semiconductor contact in thermal equilibrium.
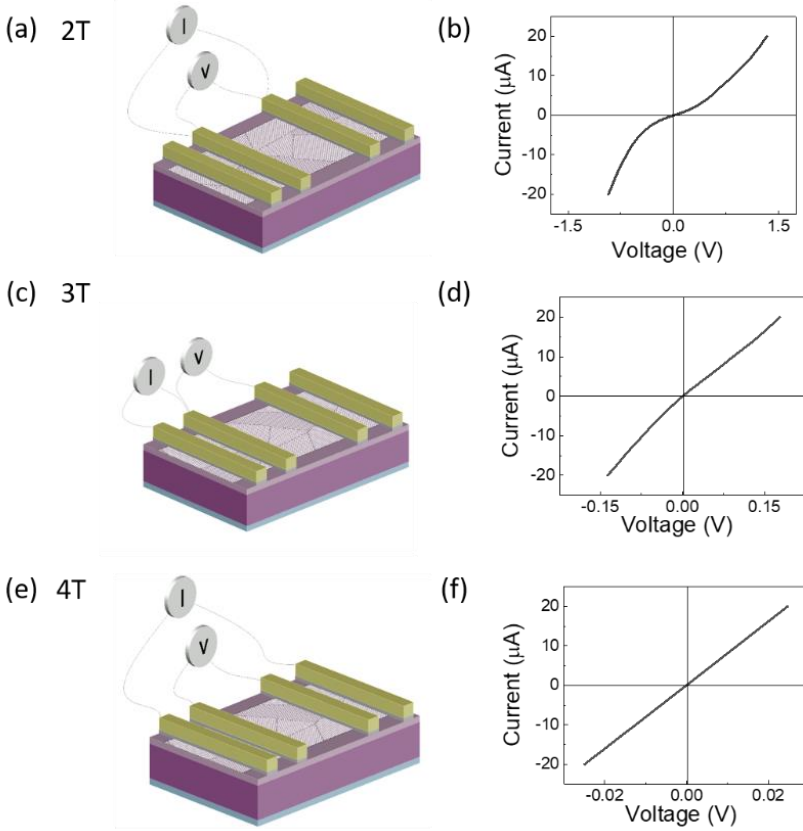
Figure 2.7. Measurement set up for graphene-based device in 2-, 3- and 4-terminals configurations and the corresponding I-V curves.

The tunneling behavior is based on the potential barrier between metals and semiconductors (Figure 2.8a). Since metals and graphene do not have a bandgap, it is characterized by the value of its work function (ϕ_M and ϕ_{Gr}, respectively). On the other hand, the energy difference between the Fermi and vacuum level (conduction zone) for semiconductors is described in terms of electron affinity (χ) and workfunction of semiconductors (ϕ_S). When two materials are close enough to each other (semiconductor-metal or graphene-metal), they start to reach thermal equilibrium so their Fermi levels are aligned (Figure 2.8a,b). Charge carriers will then flow from a high-energy state to a low-energy state, in this case, from the metal to the semiconductor. Under equilibrium, charges can move in both directions. In the case of applied forward bias, the flow of electrons from the semiconductor becomes more dominant. On applied reverse bias, barrier height increases, and only electrons with energy higher than the potential barrier (ϕ_B) can flow from the semiconductor to the metal.
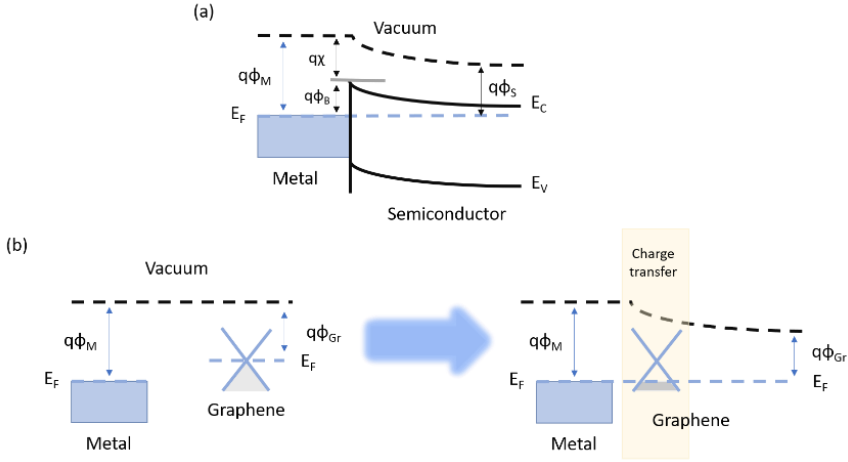
Figure 2.8. (a) Energy-band diagram for the metal-semiconductor junction. (b) Representation of metal and graphene before contact I and after contact with aligned Fermi levels.

The I-V curve of the graphene-contact interface consists of two parts: the Ohmic part originating from the graphene channel (linear regime) and the nonlinear part can originate from the Schottky diode (non-linear regime) (Figure 2.7d). Originally, the Schottky diode is based on a metal-semiconductor interface; in our case, instead of a semiconductor, we have a semimetal (graphene). Since graphene is sensitive to the environment and substrate, and CVD graphene is polycrystalline, therefore the electrical properties can vary from one to another device channels. The heavily electron-doped nature of the graphene channel was observed in our devices. This leads to an upward shift of the Fermi energy. The difference between the Fermi levels of the metal contacts and graphene is accommodated by a charge transfer region. For spin transport devices, creating spin polarized electrons becomes more efficient by introducing a layer of ultra-thin metal oxide to inject charge carriers from the bulk metal to the two-dimensional material (graphene). Here the non-linearity arises from the tunnel barrier shape at high bias across the barrier, as the transition takes place from direct tunneling to Fowler-Nordhiem tunneling [88]. The metal oxide layers are also known to impact the properties of graphene, which will be discussed in Chapters III and IV.

Four-terminal (4T) and cycling measurements

The channel resistance can be accurately measured by a 4-terminal configuration (Figure 2.7e). The problem of contact resistance is eliminated here by having different contacts for the current source and voltmeter. Using simple Ohm's law

$$R_{graphene} = \frac{V}{I}, \qquad (2.4)$$

where $R_{graphene}$ is graphene resistance, V is voltage drop between the two voltage terminals and I is current, we can estimate the resistance of the as-fabricated graphene and also after manipulation on the graphene channel (Figure 2.7f).

Another informative measurement is cyclic 3T and 4T measurements, where, I-V curves are recorded in cycles by varying the maximum current in steps. This is discussed in detail in Chapter III.

2.3.2 Gate-dependent measurements and analysis

Gate-voltage-dependent transport measurements are a common technique to measure the performance of transistor-type devices. Changing the voltage V_G at the gate electrode makes it possible to control the concentration of current carriers. Since the Fermi level in graphene is directly proportional to the gate voltage applied to the material, therefore transport measurements allow us to determine the position of the Fermi level by recording the Dirac curve, where electrons and holes reside on a two-dimensional Dirac cone. The measurement configuration is similar to the 4-terminal configuration, but the current was kept constant, and the gate voltage sweeps in between -100 V to 0 V (Figure 2.9a,b).
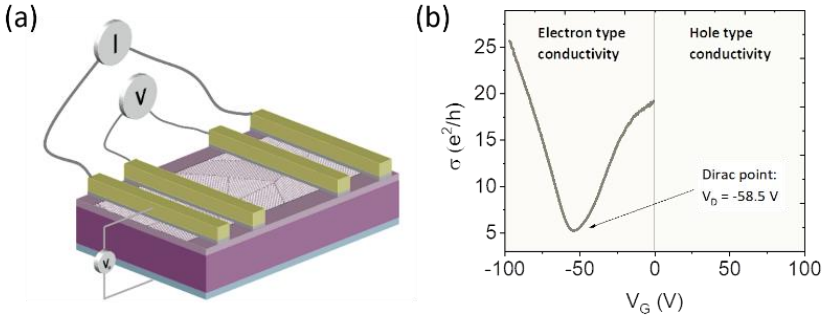

Figure 2.9. (a) Graphene-based device for gate-dependent measurements. (b) Gate-dependent conductance (σ) versus gate voltage (V_G) exhibits the Dirac curve for the device, regions related to electron and hole-type conductivity for Dirac point position.

A typical plot showing the variation of conductance (σ) as a function of the gate voltage (V_G) is shown in Figure 2.9b. The mobility of the charge carriers is an important parameter characterizing graphene channels and can be extracted from the slope of a transfer curve (Figure 2.9b) using the following equation:

$$\mu = \frac{\Delta\sigma}{\Delta V_G} \frac{L_{ch}}{W_{ch}} \frac{1}{eC_{ox}}, \qquad (2.5)$$

where σ is the conductance, V_G is the applied gate voltage, L_{ch} and W_{ch} are the length and width of the graphene channel, and $C_{ox} = 1.211 \times 10^{-8}$ F/cm^{-2} is the capacitance per unit area of the SiO$_2$ layer.

The minimum conductivity σ_{min} is a limit below which the conductivity of graphene cannot decrease, even for zero charge carrier concentration.

Analysis of the effects of doping and defect concentration variation is an essential part of this thesis, where we have attempted to elucidate the impact of the quality of the sample on the electrical properties of graphene. Since the Fermi level is sensitive to the applied gate voltage, therefore, the shift in the Dirac point depends strongly on the doping

concentration. The defect concentration can be quantitatively estimated based on the Drude model and Matthiessen's rule. According to Matthiessen's rule, the effective mobility of the samples is due to long-range Coulomb scattering, short-range resonant impurity scattering, and phonon scattering:

$$\rho = \rho_{Coulomb} + \rho_{phonons} + \rho_s. \tag{2.6}$$

Considering the fact that the mobility in our samples is not limited by phonons, the change in mobility can be attributed to long-range Coulomb or resonant impurity scattering and short-range scattering due to weak point disorders[89]:

$$\sigma = \left(\frac{1}{ne\mu_L} + \rho_S \right)^{-1}, \tag{2.7}$$

where σ – conductance,

  n – charge carrier concentration,

  μ - field effect mobility,

  ρ_S - resistivity of scattering centers.

As we have observed non-linear dependence of the conductivity, this deviation is associated with the density of impurities and it can be fitted using the equation:

$$\sigma = 20 \frac{e^2}{h} \frac{n}{n_{imp}} [90], \tag{2.8}$$

where σ – conductance,

  e – elementary charge,

  h – Planck constant,

  n and n_{imp} – charge carrier and impurities concentrations,

while we also include ρ_S in the equation to account for possible defect scattering.

Chapter III
Impact of metal oxides on graphene

Graphene electronic and spintronic devices widely employ metal oxide ultrathin films that serve as tunnel barriers and gate oxide layers. The presence of such metal oxide layers can impact the properties of graphene and doping levels, interface bonding, and related performance. In this chapter, we will discuss how two widely used oxide interfaces of AlO_x and TiO_x impact graphene distinctly [Paper I]. Furthermore, how unique aspects in AlO_x|grapheneinterfaces can have implications for spintronics and nanoelectronic device performance.

3.1 Significance of metal oxides in graphene electronics and spintronics

Fabricating efficient graphene electronic and spintronics devices requires a conscious choice of materials, especially for those in direct contact with the graphene surface. Metal oxide layers (such as ultra-thin AlO_x, TiO_x, and HfO_2) are widely implemented in graphene nanoelectronic and spintronic devices as a gate oxide and tunnel barrier interfaces. Transistors require the deposition of dielectric layers on top or bottom of the graphene for efficient electrostatic control of the channel and better device reliability[91]. Graphene field-effect transistors (GFETs) employ different metal oxide dielectrics as gate layers [92] or the semi-insulator gate dielectric [36], which make metal oxides key ingredients for graphene electronics. In addition, metal oxide interfaces with 2D materials can serve as a promising means for thin-film memristive devices even on flexible substrates [93] for practical imitation of synaptic activities. The 2D material-based vertical RRAM structures use AlO_x and TiO_x as resistive switching layers sandwiched between graphene and pillar electrodes [94], [95]. The memristive effect in the graphene/metal oxide interface is described by the linearity of the current flow with the ensuing trap-controlled space-charge-limited current (SCLC). Thus metal oxides with 2D materials have a wide prospect for 2D neuroelectronics. Furthermore, in graphene spintronics, metal oxide interfaces are important to both graphene planar as well as vertical structural components [41], [71]. For example, ultrathin layers (~nm) of the metal oxides serve as tunnel barriers in spintronic devices offering optimum interface resistance to overcome the conductivity mismatch problem associated with electrical spin injection [49], [72], [73], which is necessary to reduce interface spin backscattering [96]. Despite the diversity of applications, it is not completely clear how metal oxides interface with graphene. Even though such oxides can induce charge transfer into/from graphene, to what extent these bring changes in the electrical properties of graphene, and how in particular, the oxide layers affect the spin relaxation in graphene is not established. Evaluation of response from different oxides shows that graphene with hafnium oxide compared with aluminum and titanium oxides has the best performance in terms of both cut-off frequency and maximum frequency of oscillation. That represents a promising solution to obtain the best compromise in terms of both contact resistance and field-effect mobility [92]. In this chapter, we discuss the impact of widely used oxides in graphene spintronics on the electronic properties of graphene.

3.2 Impact of metal oxides on graphene

3.2.1 Charge transfer doping mechanism in graphene|metal oxide interfaces

Distinct from the classical (substitutional) doping process, the "charge transfer layer" is used as a platform for adding or withdrawing electrons from graphene. Surface charge transfer doping is a highly efficient, uniform, and non-destructive doping method that reliably dopes 2D materials such as graphene. Charge transfer across any metal interfacing with graphene arises due to the difference in the work function of the metal relative to the carbon atom. To understand the doping mechanism on graphene, the concept of equalization of energy levels between graphene and a surface dopant is used. To describe p-type doping, the dopant energy level locates at higher energy than the valence band of the semiconductor in the energy diagram. The energy difference drives electrons from the valence band maximum (VBM) of the graphene cone to the lowest unoccupied molecular orbital (LUMO) surface dopant level when the materials are close enough (Figure 3.1). This process is similar to thermal equilibrium. However, in this model, there is not only the transition of electrons but the shift of the electron density from the graphene to the doping agent. Thus, the graphene surface acts as an electron donor to the dopant in this process. Similarly, in this diagram for the dopant, the work function of the metal, the energy diagram of metal oxides, and gas molecules can be considered. And the greater the difference, the more graphene doping occurs.
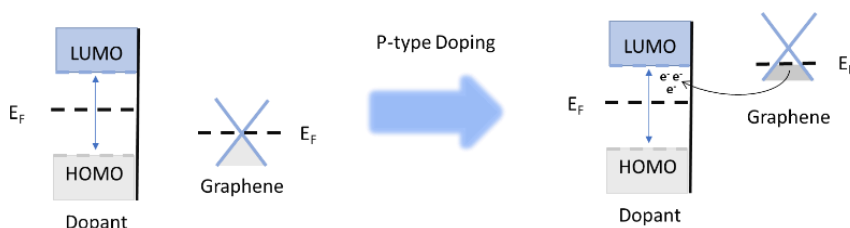

Figure 3.1. Schematic diagram of mechanism before and after p-type surface transfer doping.

For example, Ag and Cu, having a work function of 4.4 and 4.24 eV, respectively, manifest themselves as n-type dopants with charge separation at the metal-graphene interface, while the reverse is the case with Au with a work function of 5.2 eV [97]. Theoretical calculations also showed that for such metals, the Fermi level shift (n or p-type doping) also depends upon the layer thickness [98]. Unlike metals, the situation is not entirely clear when it comes to tunnel barrier oxides such as TiO_x or AlO_x on graphene. DFT calculations showed that the interaction between graphene and metals is weaker for Ti than for Al. The Ti-donated electron charge density is highly localized around the interacting carbon atoms. Besides, titanium does not show the tendency to form clusters, contributing to the uniform distribution on the graphene surface [99]. The redistribution of electron density after oxidation is not fully understood, even from a theoretical perspective. From the experimental point of view, although the ultrathin metal oxide layer can be directly realized using atomic-layer deposition (ALD) or sputtering techniques, these can lead to many defects, are a source of short-range scattering [74], and are less compatible with spintronic device fabrication processing. Therefore, in

graphene spintronic devices, Ti or Al are deposited using electron beam evaporation and are oxidized with contact in air/O_2. This makes it extremely important as well as intriguing to understand the modification after oxidation and how it affects the charge transfer in general at graphene-metal oxide interfaces.

3.2.2 Electrical characteristics in graphene covered with metal oxide

To understand charge transfer in graphene with deposited TiO_x/AlO_x (excluding the impact from contacts), we performed gate-dependent electrical 4-probe measurements (Dirac curves) on graphene devices with multiple contacts before and after the ultrathin (~nm) layer deposition of the metal oxides layers. As shown in Figs 3.2a-b, for both oxide layers, the charge neutrality point (CNP), i. e. the Dirac point (V_D) shifts towards the positive gate voltage region. Such a shift suggests that both these metal oxides cause a downward shift of the Fermi level in graphene, implying p-type doping. It is worth noting that the V_D shift is significant even with the ultrathin (~nm) layer, and the interface trap density of energy states for acceptor shows an effect by both types of oxides, as evidenced by the shift in V_D. Despite the huge variation in V_D (i.e., p-type doping), both oxides-overlaid graphene samples show reasonably good values of sheet conductance (σ_0), and mobility (μ) sustained moderately small changes (similar or ~10% for most of the devices) from pristine graphene devices to graphene|oxide devices.
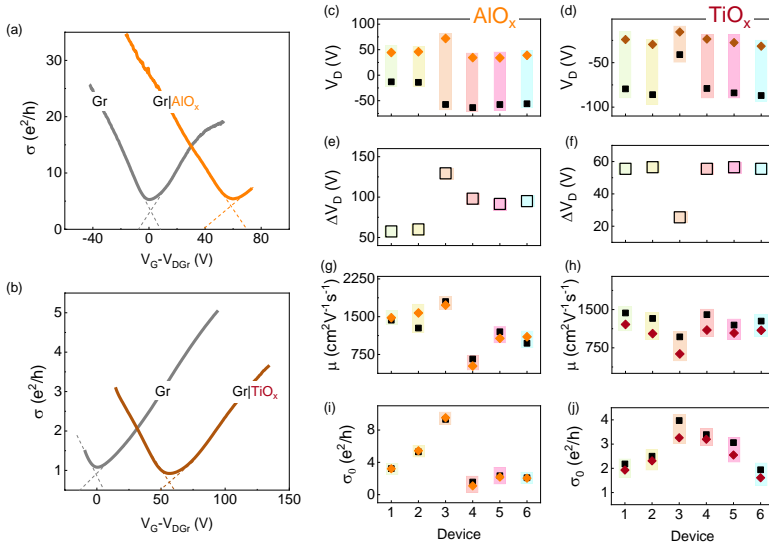

Figure 3.2. Electrical characteristics modification for graphene devices with AlO_x and TiO_x layers. Gate-dependent conductivity (in units of quantum of conductance e^2/h) versus gate voltage (V_G) Dirac curves for the devices with graphene before (grey curve) and after (orange/brown curve) deposition of (a) AlO_x and (b) TiO_x. The dashed lines are provided here to guide Dirac point broadening. (c)–(j) summary of Dirac point location (V_D), and its shift (V_D shift), field-effect electron mobility (μ), sheet conductance (σ_0) for pristine graphene (dark square), and AlO_x and TiO_x (colored diamond) deposited devices.

Our electrical measurements, together with complementary experiments (discussed in paper-I) reveal that a doping ~10^{12} cm^{-2} is primarily due to surface charge transfer between the oxide layers and graphene for most devices, and oxide layer coverage can dope graphene without drastically altering its electrical performance.

Defects in graphene affect charge and spin transport properties significantly, due to long-range Coulomb scattering from charged impurities [100] and short-range defect scattering [101]. Using the equation:

$$\sigma\,(n) = Ce\left|\frac{n}{n_{imp}}\right| + \sigma_{res}\,, \qquad\qquad (3.1)$$

where, $C = 5 \times 10^{15}$ V^{-1}s^{-1}, e is the electronic charge and σ_{res} is the residual conductivity, we estimated the charge impurity density[100] (see Figure 3.3) with a variation Δn_{imp} ~ 5-20 × 10^{11} cm^{-2} for both oxides, which is up to an order higher than the sp^3 defect density that we estimated in Raman spectra (see next section). We, therefore, believe that, as widely observed, the mobility in graphene is limited by the long-range coulomb scatterers, while the sp^3 defects partially contribute to the observed electrical parameters.
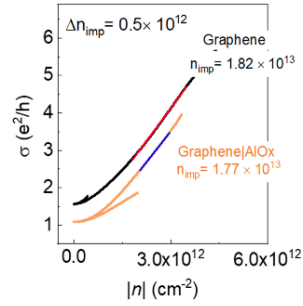

Figure 3.3. Charge impurity density estimated by fitting the Dirac curves using the equation 3.1

3.3 Spectroscopic study of graphene|metal oxides

A deeper investigation can be pursued by XPS which allows for studying the oxidation states, and sp^2 and sp^3 carbon ratio in element analysis. The overview spectra as well as the C 1s range is presented in Figure 3.5a and b. The composition of the aluminum oxide and titanium oxide films is determined by fitting the overview spectra and comparing the O 1s peak intensity for pristine graphene and graphene with each metal oxide film. The Ti 2p and Al 2p spectra are used as well to estimate the composition of the respective oxide film. The Al 2p spectra show binding energy of 75 eV, suggesting that the deposited film is Al$_2$O$_3$ [102]. The O 1s spectrum for the AlO$_x$ sample is symmetrical and has binding energy that corresponds to that of metal oxide as well as silicon oxide. The peak of Ti 2p shows binding energy of 459 eV for the Ti 2p3/2 core level. This suggests that titanium has an oxidation state of 4+ which means that titanium forms TiO$_2$[102]. From the intensities of Ti 2p and O 1s in the overview spectra, the composition of the film can also be estimated. This implies that both metals are nearly fully oxidized.
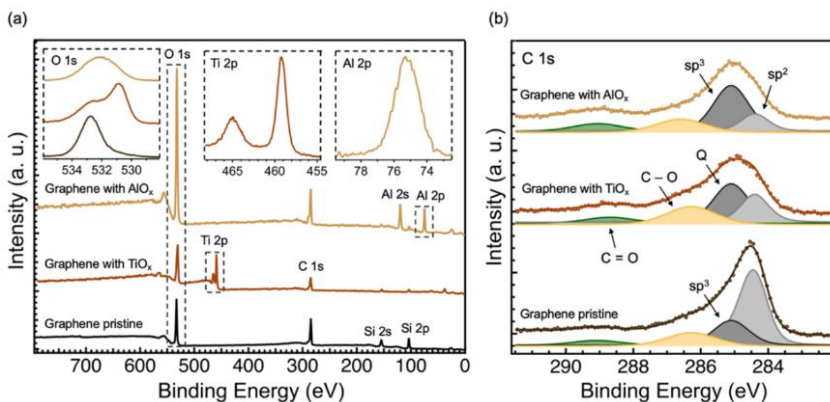
Figure 3.5. (a) Overview of XPS spectra of pristine graphene and graphene with AlO$_x$/TiO$_x$ layer on top and (b) C 1s spectra used for fitting.

The C 1s spectra (Figure 3.5b) are used to compare the relative sp^2 and sp^3 contribution to the peak, as fitted with a set distance. The pristine graphene sample shows a larger sp^2 contribution than the two samples with metal oxide on the graphene surface. As defects are introduced by depositing metal oxide on the graphene surface, the sp^2/sp^3 ratio decreases. A larger proportion of sp^3 is observed for the sample with AlO$_x$ than for the sample with TiO$_x$.

Considering that new defects are introduced in the graphene by the metal oxides, we find that the sp^3/sp^2 ratio for the Gr-TiO$_x$ is of the same order as pristine Gr, but nearly one order larger for Gr-AlO$_x$. This suggests that Gr-AlO$_x$ significantly induces sp^3-defects, which qualitatively corroborates the strong emergence of the D peak in the Raman spectrum.

Table 3. Binding energies and intensities of fitted C 1s spectra and sp^2/sp^3 ratio.

	Graphene		Graphene/AlO$_x$		Graphene/TiO$_x$	
	E$_b$ (eV)	I (Area)	E$_b$ (eV)	I (Area)	E$_b$ (eV)	I (Area)
C 1s – sp^2	284.56	78	284.74	13	284.66	26
C 1s – sp^3	285.26	42	285.44	57	285.36	41
sp^3/sp^2 ratio	0.54		4.35		1.56	
Inf. depth	6.3 nm		7.4 nm		7.8 nm	

Additionally, surface carbon bonded to oxygen can have binding energies around those of sp^3-carbon [103] – in the case of Gr-TiO$_x$, the component marked Q at 285.1 eV must consist of any sp^3-defects in the graphene and such surface carbon. However, in the case of Ti deposits, the surplus intensity at the sp^3-binding energy position has been observed, also observed in pristine graphene, albeit much lesser than Al-oxide layered graphene. Since it is observed for pristine graphene also, the Q peak can be attributed to carbon elsewhere in the system. Furthermore, considering the performance with TiO$_x$ barriers,

this does not necessarily arise from the sp^3 hybridization of the graphene lattice. In fact, keeping in mind that with a large 100 μm X-ray probe diameter, a significant sp^3-contribution can originate from the PMMA resist residues intrinsic to the CVD graphene transfer process (similar to the pristine graphene background sp^3). This can be avoided by MicroRaman characterization. Especially, to study defects in graphene/metal oxide samples, the graphene channel can be probed by micro-Raman spectroscopy. Fig. 3.4 summarizes the Raman spectra obtained on pristine graphene and graphene with metal oxide layers. First, for pristine graphene, the well-known G and 2D mode features, with frequencies near 1584 and 2678 cm^{-1}, respectively, were obtained. The same peaks were also identified on graphene samples with AlO_x/TiO_x layers, which confirms the integrity of graphene sheets covered by oxide layers. The ratio of the 2D peak intensity to the G peak (I_{2D}/I_G) is a parameter to determine the quality and monolayer structure of graphene [104]. Here, in pristine graphene and graphene with TiO_x, the $I_{2D}/I_G \geq 2$ confirms the good quality of the CVD polycrystalline graphene that we employed in this study[105]. However, in the presence of AlO_x, graphene shows different behavior with the 2D to G peak intensity ratio decreasing significantly to 1.45, which suggests possible degradation of sp^2 structure in graphene. In addition, the G peak's doping sensitivity helps confirm the nature of doping. The location of the G peak for pristine graphene is 1584 cm^{-1}. For graphene coated with AlO_x, the peak shift was approximately 3 cm^{-1}, and for the case of TiO_x, about 13 cm^{-1} compared with pristine graphene. A similar shift was also observed for the 2D peak. Such Raman-shift to the left in the oxide layered graphene indicates a p-type doping effect, which is in good agreement with our transport measurements.
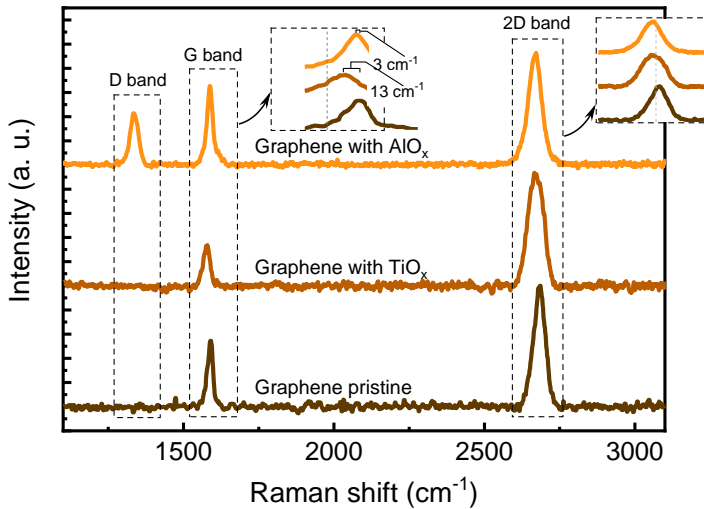

Figure 3.4. Raman spectra of pristine graphene and graphene with deposited TiO_x and AlO_x. The corresponding G band shift for the samples before and after deposition is presented.

However, in the case of aluminum oxide-covered graphene, strikingly, we observed the emergence of the D peak (near 1340 cm^{-1}), which is a signature of Raman-active defects, suggesting the introduction of appreciable sp^3 carbon defects, a source of graphene modification by AlO$_x$ only. Although Raman spectroscopy in most cases serves as qualitative analysis, it is also possible to quantify defects concentration in graphene. We obtained the concentration of defects for a graphene sample with AlO$_x$ by extracting the G to D intensity ratio from the spectrum and the excitation laser wavelength. From the estimation, we found a concentration of defects for graphene with evaporated Al (0.8 nm) $\sim 1.4 \times 10^{11}$ cm^{-2}, which is nearly one defect per 10,000 carbon atoms. For a huge shift in V_D $\sim$50-100 V, corresponding doping of 10^{12} cm^{-2} can be expected. Therefore, the significant doping is due to surface charge transfer doping, while the sp^3-related defect contributions are nearly 10%, which is unique to AlO$_x$ interfaced graphene. Despite the defects, the electrical properties of graphene are relatively preserved in graphene|TiO$_x$ (AlO$_x$) devices.

3.5 Graphene|metal oxides surface morphology

To understand the surface morphology of the oxide coverage over graphene, we investigated the samples by atomic force microscopy (AFM). Here metal oxide layers were realized by first deposition of nm thick metals (Ti or Al) on CVD graphene, followed by their oxidation in the open air. We chose a 1 μm × 1 μm scan area to check the shape of the grains on top of the graphene surface and the height profile (Figure 3.6). Expectedly, there is a deviation from the smooth morphology of pristine graphene to graphene with the oxide layers. The common feature of oxide-covered graphene is the presence of ridges and grooves. The comparison between the surfaces is illustrated in Figure 3.6. The AFM image shows an alternation of dark and bright stripes in the case of Ti or circle-shaped dots in Al. The mean position was fixed to 0 nm height in the height profile. Compared to the height profile with the standard topography of graphene, the oxide-covered graphene possesses a higher topographic root-mean-square roughness. While conspicuous pinholes can be understood from the deviation in the height profile and images for AlO$_x$, perceptible swings in the height profile are also observed in the Gr-TiO$_x$ system. One can attribute the other large clusters to possible resist residue regions observed in pristine graphene that can act as nucleation sites. Both oxides show an area roughness of R$_q$~1 nm, suggesting that both Ti and Al deposited on graphene by e-beam evaporation and following oxidation of the metals do not necessarily lead to full coverage, and hence current crowding is a common problem for both metal oxides in graphene spintronic devices.
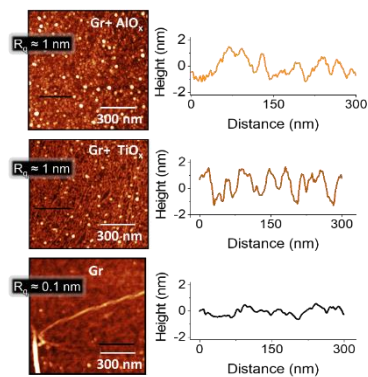

Figure 3.6. AFM images of pristine graphene (Gr) and graphene after AlO$_x$ and TiO$_x$ deposition on top of it. The corresponding grey line scans show roughness profiles, and R$_q$ represents average area roughness.

40

3.6 The sp^3 defects graphene/metal oxides interface

In this chapter, we have presented a systematic study of the impact of metal oxides such as TiO_x and AlO_x on the properties of graphene due to surface charge transfer doping. The gate-dependent measurements on the same devices both prior and after the deposition of oxide reveal a p-type doping effect for both oxides. Besides, the observed sp^3 hybridized defects in the interface of graphene and AlO_x have significant consequences for device performance. Earlier studies have shown that the interaction between graphene and Ti oxide is weaker [106] than in the Al case and uniform coverage of TiO_x is expected [99]. Also, a higher spin lifetime of ~1ns [12] was recorded for the TiO_x tunnel barrier. Considering that both oxides show similar kind of morphology, the additional sp^3 defects in graphene-Al_2O_3 can have implications for graphene electronics and spintronic devices. The sp^3 defect centers can exhibit magnetic moments ~$1\mu_B$ (as unveiled by the electronic structure calculations in Paper I, pages 64-65), which can lead to resonant spin-flip scattering of electrons in graphene spintronic devices, which could explicate the widely observed lower spin lifetimes in Al_2O_3 based graphene spintronic devices. This has been conventionally attributed to pinholes in the AlO_x barrier. On the other hand, the sp^3 defects and defects can act as traps for storing charges, which could be used for a new switching mechanism for setting and resetting processes in graphene-based synapses. Thus, our study provides new results that could contribute to the development of hybrid graphene interfaces for graphene neuromorphic and spintronic devices.

Chapter IV
Current carrying capacity of CVD graphene

Understanding high current stress response in CVD graphene is a key point for device performance and exploring scalable applications. The grainy nature of the channel and resistive tunnel barrier interfaces in CVD graphene spintronic devices can impact the current carrying capacity and operation abilities. In this chapter, we will discuss the impact of high current on graphene and oxide interfaces employed for electrical spin injection, and their performance limits [Paper II].

4.1 High current impact on CVD graphene

As demonstrated in mechanically exfoliated graphene, it can conduct a current density J_b ~ 10^8 A/cm^2 [80], [107], which is typically two orders higher than technologically favorite copper. On the other hand, studies performed in CVD graphene revealed relatively lower breakdown current density of J_b ~4 × 10^7 A/cm^2. Recently a value of 1.18 × 10^8 A/cm^2 has been achieved in 300 nm channels of CVD graphene contacted by metallic electrodes[108]. Since the typical grain size in CVD graphene exceeds such size, it can be considered to be a single-grain device, and the actual current carrying capacity of polycrystalline CVD graphene is still unclear. Here, the limitation of the maximum possible current that can be applied arises from the grainy structure, wrinkles, and defects intrinsic to CVD-graphene devices. The defects and wrinkles act as localized hot spots along with nonuniform resistance distribution not only in the graphene channel but also at the interface. The purpose of this investigation is to determine the stability of graphene spintronic devices.

The standard method to probe high current breakdown is 2T measurements, where the current increase is detected by increasing the applied bias voltage. We used CVD graphene spin devices (as described in earlier chapters) for our study and initial high-current stress experiments were performed in two-terminal (2T) measurements (sweeping voltage and measuring current across two contacts). As shown in Figure 4.1, with the increase in the applied bias voltage, current increases, and eventually, the electrical breakdown is observed at a high current. Low bias current-voltage (I-V) measurements revealed non-linear curves, due to the tunneling behavior of the contacts (as shown in the inset of Figure 4.1) involved in the measurement along with the channel.
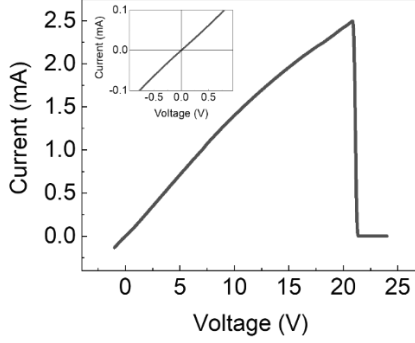
Figure 4.1. 2-terminal I-V curve measured up to electrical breakdown. Inset: Low-bias I-V measurements.

The high current carrying capacity of graphene originates from its unique electronic properties such as high carrier mobility and a large number of active carriers that lead to low sheet resistance. To investigate this in CVD graphene spintronic devices, we measured an extensive number of devices, that revealed a high current density J_b ~ 2-5 × 10^8 A/cm^2 (Figure 4.2) displaying sheet resistance 0.5 - 2.3 kΩ for most of the devices. Here, we calculated the current density using the following formula:

$$J_b = \frac{I_b}{w \cdot t},\qquad\qquad (4.1)$$

where I_b is the applied current to the channel with width w and thickness t of graphene. In Figure 4.3, we show the ripples/wrinkles in graphene (a), and how ripples are integral to an actual device with an electrode (b). Measuring the actual and effective dimensions of the graphene channel after processing, we observed the maximum current density J_b ~ 5.2 × 10^8 A/cm^2.
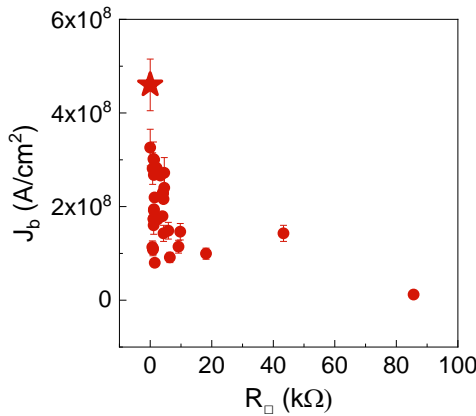

Figure 4.2. Breakdown current density J_b as a function of sheet resistance of the CVD graphene (the star indicates the maximum current density of 5.2 × 10^8 A/cm^2).
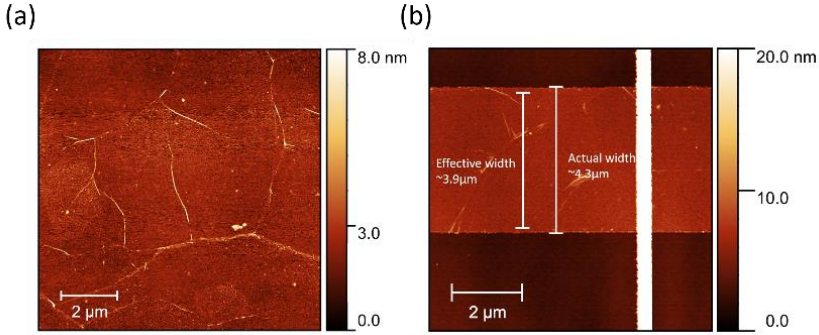
Figure 4.3. AFM image of graphene (a) over 10 μm x 10 μm area with clearly observable wrinkles and ripples, (b) channel with corresponding actual and effective width.

Avoiding common contact with the current source and voltmeter allows us to eliminate the effect of contact resistance. To exclude the impact from contact interfaces, and only focus on the graphene sheet capacity, following the 2T measurements, we I-V characteristics in the four probe configuration. Here, we could isolate the tunneling contributions from contacts, and observe a linear I-V for the graphene channel. At low currents, that is the operating range (± 50 μA), the graphene channel does not deviate from Ohmic behavior. In the high-current region, two regimes can be distinguished in the I-V curve: reversible and non-reversible, where self-heating can be observed (as displayed in Figure 4.4a). Note that despite the high current carrying capacity, the degradation of the CVD graphene channel due to cumulative Joule heating can lead to an irreversible regime. To examine the transition between the two regimes, I-V curves were recorded in cycles with the maximum current varied in steps (I_{step} = 0.2 mA, between 0 - 3 mA). The transition between reversible and irreversible regimes is observed to occur at a specific value of current ($I_{max\,rev}$) in each cycle, and the sheet resistance of the graphene channel changes after each cycle beyond the reversible regime. Interestingly, limiting the operating current to a range less than $I_{max\,rev}$ (~10^8 A/cm^2) prevents overheating and maintains a constant stabilized sheet resistance (Figure 4.4b). This implies that within the $I_{max\,rev}$ regime, graphene devices on Si/SiO$_2$ can be operated with heat dissipation managed by the Si/SiO$_2$ substrate efficiently.
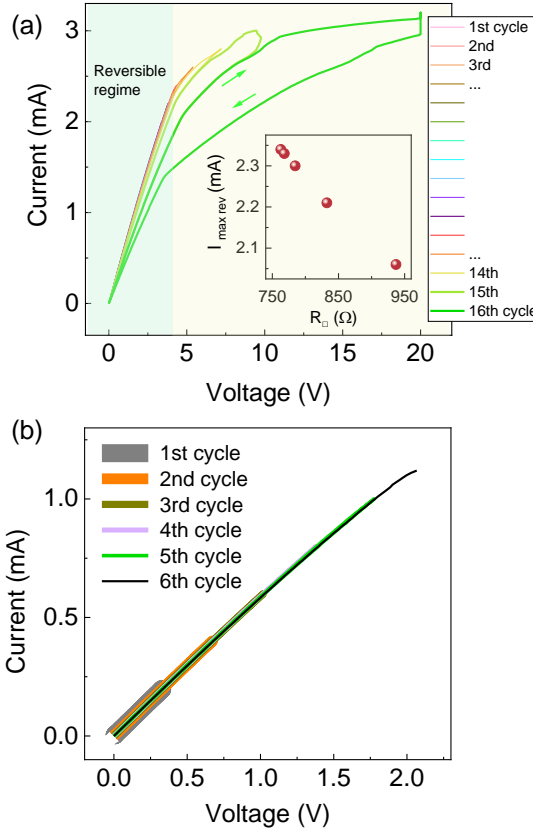
Figure 4.4. (a) Measured 4T I-V curves cycles with linear (reversible) and non-linear (non-reversible) regimes at high voltage (~4.5 V) (b) 4T I-V curves cycles of the device within the reversible regime.

4.2 High current stressing in spin tunnel contacts of graphene/TiO$_x$

As we have discussed in Chapter III, metal oxide tunnel barriers are essential for efficient electrical spin injection into graphene. However, the resistance of these barriers puts a limit on device performance and spin polarization at high currents that are often required for applications, for instance, for possible spin torque-based applications. The behavior of the interface in the devices is quite distinct from those of the materials on either side of the interface. Besides, considering the ultrathin nature of the oxide tunnel barrier, contact resistance modulation can be possible at high currents. In our experiments, following the 3-terminal measurements (described in Chapter II), we have performed electrical measurements to uncover the impact of high currents on tunnel contacts. First, three terminals (3T) I-V measurements using low current reveal tunneling behavior in the ferromagnetic tunnel contacts. The contact resistance was found to be in the range of kΩ. The nonlinearity in the I-V curves was observed due to the tunneling behavior across the

junction as well as the self-heating at higher bias voltage [80], [82], [109]. To better understand the device functionality, cyclic 3T measurements were performed till electrical breakdown across the contacts. In each cycle, a current is swept from 0 to a maximum value and back to zero, where the maximum current was increased in steps of $\Delta I_{max} = 0.25$ mA. As shown in Fig. 4.5a, the resistance of the barrier was seen to decrease at high injection currents. This consistent change can originate from cumulative effects and the observed hysteresis could be related to the trapping of charges under the contacts. In Fig. 4.5b, we show low bias (100 mV) barrier resistance as a function of the high current density to which the contact|graphene interface was subjected. We observed that at high current density, the resistance decreases, which could be ascribed to the possible formation of conducting nanofilaments in the Co|TiO$_2$|graphene junction in the possible off-stoichiometric naturally-oxidized ultra-thin oxide layer and consequent high current crowding.
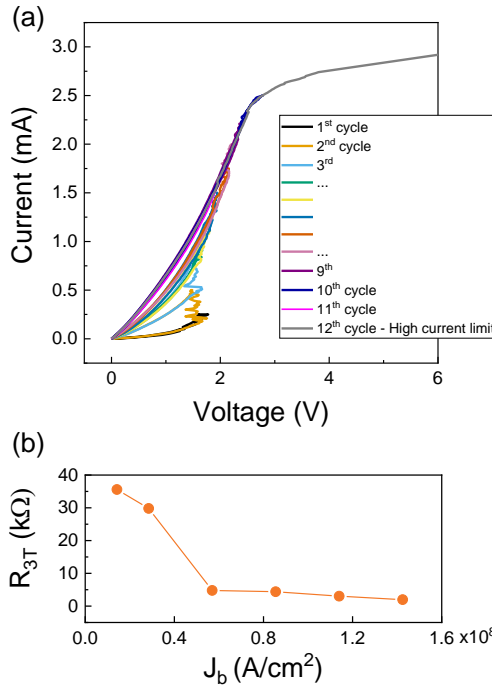

Figure 4.5. (a) Consecutive multiple 3T I-V cycles with increasing maximum applied current and electrical breakdown in the 12th cycle. (b) Contact resistance (measured within the reversible regime, V < 0.1 mV) vs the maximum applied current density in a measurement cycle.
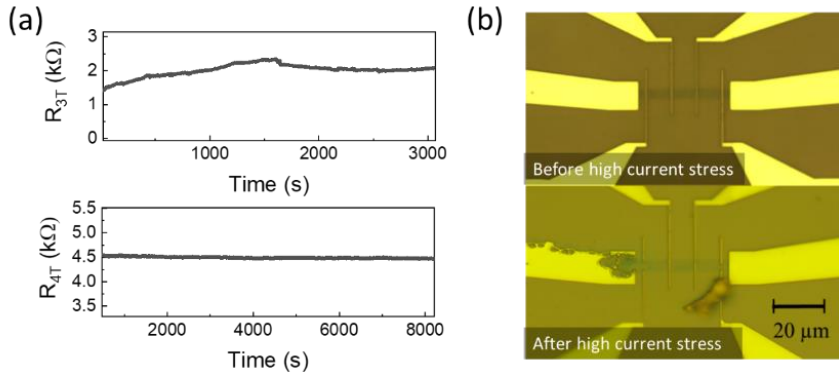
Figure 4.6. (a) Three-probe (upper panel) and four-probe (lower panel) resistance of CVD graphene as a function of time measured using high bias currents of 2 mA and 1 mA, respectively. (b) Optical image of CVD graphene on SiO_2/Si substrate with Co/TiO_2 tunnel contact before (upper panel) and after (lower panel) electrical breakdown.

As shown in Figure 4.6, we also investigated the sustainability of the devices over longer times. Measurements using different terminals provide information about different parts of the device. It is observed that the graphene channel and graphene/metal oxide interface respond differently to a constant high bias current of 2 and 1 mA, respectively. After a prolonged time (approximately 8000 s), graphene still exhibits the same resistance even under a high bias current (Figure 4.6a, lower panel). However, the resistance under the contact does not show the same stability over time for the applied constant bias current of 2 mA (Figure 4.6a, upper panel), which can be attributed to the likely formation of nanofilaments as well as contact interface deterioration. Figure 4.6b shows the optical image of the CVD graphene with ferromagnetic electrodes before and after the electrical breakdown. The CVD graphene still survives under a high bias current, while the electrode starts to break before the graphene breakdown. Notably, our experiments reveal here for the first time how channel resistance and contacts in graphene spintronic devices respond to high current stress. While the channel resistance remains in a reversible/stable regime up to high current densities, the contact deteriorates due to the possible formation of filaments in the 10^8 A/cm^2 current density regime.

4.3 Heating effects in graphene spintronics devices

Even though the behavior of graphene channels and contact interfaces are different, a reliable spin transport signal at high applied currents of 100 µA - 1 mA was observed (shown in Paper II, page 77), although higher currents often led to a decrease in nonlocal resistance, which is a measure of spin current detected by the detector. The observation of the lowering of spin signals at higher currents can be connected to thermoelectric effects in the channel as well as junctions (Figure 4.7). In a typical spin transport device, Joule heating occurs along a channel, which can dissipate through the Si/SiO$_2$ substrate. As long as the rate of heating of the graphene channel is the same as the rate of heat dissipation, the system remains in the reversible regime, with graphene sheet resistance unaltered. In addition to the Joule heating, the heating/cooling process at the electrode interfaces can occur due to the Peltier effect. The multilayer contact structure causes structural modification of the tunnel barriers when the temperature of the injector

electrode increases. Injected electrode possesses hot electrons along the graphene/TiO$_x$ interface. Notably, due to the smaller width of the contacts (100 nm) compared to the characteristic transfer length (1 μm) the contribution of current crowding near the interface can be neglected. Local heating of the injector electrode may not cause Joule heating of the spin transport channel. However, a voltage drop can be expected between the injector and detector electrodes due to the Seebeck effect, which could contribute to a shift in the whole signal, without impacting the nonlocal resistance.
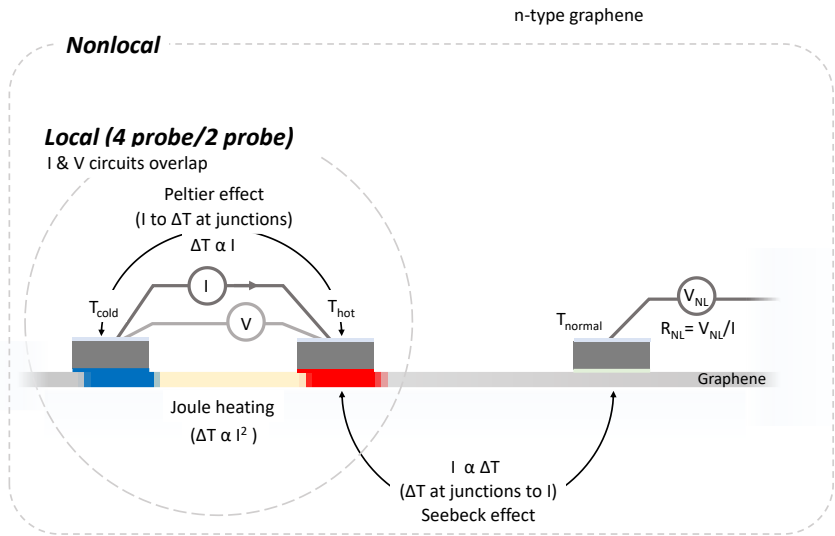

Figure 4.7. Measurement configurations with corresponding thermoelectrical effects.

Conclusions and plans for the future

In this thesis, we have explored the stability and interface details in graphene and contacts in graphene spintronic devices. Considering the practical relevance of large-scale chemical vapor deposited graphene, which shows competitive performances in both quantum and spin transport [110], we have focused our investigations on CVD graphene devices. In such devices, inherently occurring grains and ripples in the μm range affect electrical performances, while charge transfer at contact interfaces could lead to surface charge transfer doping [12]. Titanium and aluminum oxides have been widely used as tunnel barriers to study charge and spin transport, as they offer optimum interface conditions for enhanced efficiency. Like CVD graphene, these metal oxides are also compatible with scalable processing methods. This makes it really important to gain a fundamental understanding of the behavior of the spin current carrying channels as well as contact interfaces, which we have investigated here.

First, to gain in-depth understanding of the graphene/metal oxide interfaces, we probed graphene covered by metal oxides with electrical measurements. Ultrathin Al and Ti oxide interfacing with graphene were found to induce p-type doping $\sim 10^{12}$ cm^{-2} in graphene for both metal oxides, with reasonably retained charge mobility and sheet resistance, before and after the top oxide layer realization. With minor changes in charge traps, the charge impurities cause Coulomb scattering, while short-range defect scattering results from neutral defects. Despite the same kind of doping for both oxides, the oxide layers could bond differently with graphene, as revealed by our X-ray photoelectron spectroscopy and Raman spectroscopy studies. X-ray photoelectron spectroscopy suggests a rather intricate nature of the doping, not just due to charge transfer from C atoms but also due to significant sp^3 defects for Al oxide. This has been precisely confirmed by the emergence of sp^3 defect active Raman D band for Al oxide layered graphene, in sharp contrast to Ti oxide layered graphene, where the D band was absent. Density functional theory calculations revealed that such sp^3 hybridization at the interface exhibits a local magnetic moment ($\sim 0.5 - 1.0$ μ_B) (see Paper I, pages 64-65). This overall difference in how Al and Ti oxide bond with graphene can have prime implications for graphene nanoelectronic and spintronics. The non-zero magnetic moment at the interface could contribute to resonant spin relaxation, which can be a cause behind the generally lower spin lifetimes ($\sim 100 - 200$ ps) observed in AlO$_x$-based graphene spintronic devices. Typically, much larger spin lifetimes of ~ 1ns have been obtained in graphene devices with TiO$_x$ tunnel barriers. On the other hand, the sp^3 defects can also provide means to explore the charge-trapping effects of resistive switching graphene electronic devices. Our experiments reveal that oxide interfaces with graphene can be quite complex with definite implications for graphene electronic and spintronic devices.

Second, to uncover the ultimate current carrying capacity of CVD graphene channels for high-performance spintronic circuits, we performed high-current stress experiments. Despite the polycrystalline nature of CVD graphene, we observed the highest breakdown current density of $\sim 5.2 \times 10^8$ A/cm^2, which is an order higher compared to those observed in multilayer graphene [82]. To probe further details within this range, we performed four-probe measurements that allowed us to demarcate two regimes for high currents, a reversible regime ($\leq 10^8$ A/cm^2), up to which a device can be operated without significant damage, and a non-reversible regime ($> 10^8$ A/cm^2), where permanent damage can occur to the graphene lattice. These experiments established that for low sheet resistance

(~500 Ω/square), the highest breakdown current density of ~10^8 A/cm^2 can be realized even for CVD graphene in the reversible regime. We have also probed the impact of high currents on contacts by detailed 3-terminal electrical measurements. These experiments revealed that even contact interfaces show significant stability up to ~10^7 A/cm^2, while higher current density leads to a modification (lowering) of the interface resistance due to possible ion migration-induced conducting paths within the oxide barriers at the contacts. Furthermore, spin transport measurements on these devices reveal spin current signals via nonlocal measurements till ~10^8 A/cm^2.

In summary, in our two elaborate studies, we gained an understanding of the mechanism and crucial role of graphene/metal oxide interfaces in spintronic device engineering, as well as established the robustness of these devices (both graphene and metal oxide interfaces) when subjected to high current stress. At the same time, tunable interface resistance with thicker tunnel barriers still remains an unexplored avenue. High-performance CVD graphene spin devices clearly need stable tunnel barriers. For this, possible oxygen migration-induced filament formation can be avoided by employing hexagonal boron nitride [111]–[113] or fluorographene [114] due to their superior structural integrity. Since the observed sp^3 bonds can act as carrier traps for synaptic junctions, oxygen ions in the AlO$_x$ layer can be highly mobile in graphene and may form covalence bonds with the broken bonds of graphene for setting and resetting processes in memristive devices.

 During the remaining two years of my Ph.D., I aim to explore charge and spin transport in different graphene|metal-oxide and 2D heterostructures to unveil transport phenomena and tunability of properties. For example, considering the scalability of both CVD-grown materials and oxide layers, a variety of studies in quantum transport and spin hall effect in such systems covered with oxides or other 2D materials will be highly significant. Our existing results with oxide layers on graphene indicate new prospects for creating graphene-metal oxide-based synapses by harnessing interface trap states. Therefore, the investigation would also involve harnessing unique charge transport in these systems for potential neuromorphic components such as synaptic hybrid resistive switching devices and related spin devices. These studies are expected to involve fundamental investigations using our in-house complementary techniques, such as Raman and photoelectron spectroscopy

Acknowledgments

To my main advisor, *Venkata Kamalakar Mutta*, thank you for helping and supporting me through this research way. It would not be the same journey without your teaching of leadership and motivation. I expect more fun in upcoming future. Thank you for always believing in me.

To my co-advisors, *Gabriella Andersson and Olof Karis*, I am extremely grateful for your input and guidelines, which I got in my 2 years of Ph.D.

To also co-advisor, *Tapati Sarkar*, I will always remember our first meeting in the interview, how you understand me and asked questions right on target. Thank you for taking so much time and care for me. I always feel welcomed.

To my group members: *Zhaojun Li, Ulrich Noumbe, Rahul Sharma, David Muradas, Henry Nameirakpam, and Gopal Datt*, we all together created a really inimitable and wonderful team. Thank you for always being around.

To my group members from the beginning of my Ph.D., *Ramu Maddu, Jaganandha Panda, and Himanshu Mishra*, a big thank you for transferring all your knowledge and skills to me.

To my co-authors, Olle Eriksson and Renan Maciel, Andreas Linblad and Elin Berggren, and others, thank you for affording our papers to get it published.

To Håkan Rensmo, I remember the moment when you suggested me this position. Thank you for your bits of advice and encouragement.

To *the big team of the X-ray Photon Science Division*, it will be really hard to put all names (40? 70?), but I am grateful to have all of you. All PhDs buddies, thank you for always having opened doors (even of your homes) for me.

To *Ekaterina Molchanova*, my friend, your chef-d'oeuvre cover made my thesis.

To *my mom, dad, sister, and grandparents*, even though you don't know English, I love you.

To my lovely husband, *Andrei Klimovich*, I would not have done it ever without you. Thank you for being my muse, editor, proofreader, critic, supporter, showman, travel coordinator, and psychologist. But most of all, for being my best friend. I owe you everything.

References

[1]   K. S. Novoselov *et al.*, "Electric field effect in atomically thin carbon films.," *Science (80-.).*, vol. 306, no. 5696, pp. 666–669, Oct. 2004, doi: 10.1126/science.1102896.

[2]   P. R. Wallace, "The Band Theory of Graphite," *Phys. Rev. Journals*, vol. 64, no. 2, pp. 452–457, 1940, doi: 10.2208/jsceja.64.452.

[3]   A. K. Geim and K. S. Novoselov, "The rise of graphene," *Nat. Mater.*, vol. 6, no. 3, pp. 183–191, 2007, doi: 10.1038/nmat1849.

[4]   K. S. Novoselov *et al.*, "Two-dimensional gas of massless Dirac fermions in graphene," *Nature*, vol. 438, no. 7065, pp. 197–200, 2005, doi: 10.1038/nature04233.

[5]   M. Schmitz *et al.*, "Fractional quantum Hall effect in CVD-grown graphene," *2D Mater.*, vol. 7, no. 4, 2020, doi: 10.1088/2053-1583/abae7b.

[6]   K. I. Bolotin, F. Ghahari, M. D. Shulman, H. L. Stormer, and P. Kim, "Observation of the fractional quantum Hall effect in graphene," *Nature*, vol. 462, no. 7270, pp. 196–199, 2009, doi: 10.1038/nature08582.

[7]   M. I. Katsnelson, K. S. Novoselov, and A. K. Geim, "Chiral tunnelling and the Klein paradox in graphene," *Nat. Phys.*, vol. 2, no. 9, pp. 620–625, 2006, doi: 10.1038/nphys384.

[8]   J. Baringhaus *et al.*, "Exceptional ballistic transport in epitaxial graphene nanoribbons," *Nature*, vol. 506, no. 7488, pp. 349–354, 2014.

[9]   D. Huertas-Hernando, F. Guinea, and A. Brataas, "Spin-orbit coupling in curved graphene, fullerenes, nanotubes, and nanotube caps," *Phys. Rev. B - Condens. Matter Mater. Phys.*, vol. 74, no. 15, 2006, doi: 10.1103/PhysRevB.74.155426.

[10]   D. Huertas-Hernando, F. Guinea, and A. Brataas, "Spin-Orbit-Mediated Spin Relaxation in Graphene," *Phys. Rev. Lett.*, vol. 103, no. 14, p. 146801, Sep. 2009, doi: 10.1103/PhysRevLett.103.146801.

[11]   L. Banszerus *et al.*, "Ballistic Transport Exceeding 28 µm in CVD Grown Graphene," *Nano Lett.*, vol. 16, no. 2, pp. 1387–1391, Feb. 2016, doi: 10.1021/acs.nanolett.5b04840.

[12]   M. V. Kamalakar, J. Panda, M. Ramu, O. Karis, and T. Sarkar, "Ultimate spin currents in commercial chemical vapor deposited graphene," *ACS Nano*, vol. 14, no. 10, pp. 12771–12780, 2020, doi: 10.1021/acsnano.0c03376.

[13]   X. Li *et al.*, "Large-Area Synthesis of High-Quality and Uniform Graphene Films on Copper Foils," *Science (80-.).*, vol. 324, no. 5932, pp. 1312–1314, Jun. 2009, doi: 10.1126/science.1171245.

[14]   S. Bae *et al.*, "Roll-to-roll production of 30-inch graphene films for transparent electrodes," *Nat. Nanotechnol.*, vol. 5, pp. 574–578, Aug. 2010, doi: 10.1038/NNANO.2010.132.

[15]   E. S. Polsen, D. Q. McNerny, B. Viswanath, S. W. Pattinson, and A. John Hart, "High-speed roll-to-roll manufacturing of graphene using a concentric tube CVD reactor," *Sci. Rep.*, vol. 5, pp. 1–12, 2015, doi: 10.1038/srep10257.

[16]   Y. Hernandez *et al.*, "High-yield production of graphene by liquid-phase exfoliation of graphite," *Nat. Nanotechnol.*, vol. 3, no. 9, pp. 563–568, Sep. 2008, doi: 10.1038/nnano.2008.215.

[17]   X. Li *et al.*, "Highly conducting graphene sheets and Langmuir–Blodgett films,"

Nat. Nanotechnol., vol. 3, no. 9, pp. 538–542, Sep. 2008, doi: 10.1038/nnano.2008.210.

[18] S. Eigler *et al.*, "Wet Chemical Synthesis of Graphene," *Adv. Mater.*, vol. 25, no. 26, pp. 3583–3587, Jul. 2013, doi: 10.1002/adma.201300155.

[19] L. B. Ebert, "Intercalation Compounds of Graphite," *Annu. Rev. Mater. Sci.*, vol. 6, no. 1, pp. 181–211, Aug. 1976, doi: 10.1146/annurev.ms.06.080176.001145.

[20] X. Li *et al.*, "Large-area graphene single crystals grown by low-pressure chemical vapor deposition of methane on copper," *J. Am. Chem. Soc.*, vol. 133, no. 9, pp. 2816–2819, Mar. 2011, doi: 10.1021/ja109793s.

[21] P. Li *et al.*, "Wafer-scale growth of single-crystal graphene on vicinal Ge(001) substrate," *Nano Today*, vol. 34, p. 100908, Oct. 2020, doi: 10.1016/j.nantod.2020.100908.

[22] M. Wang *et al.*, "Single-crystal, large-area, fold-free monolayer graphene," *Nature*, vol. 596, no. 7873, pp. 519–524, Aug. 2021, doi: 10.1038/s41586-021-03753-3.

[23] H. Guo *et al.*, "Insulating SiO 2 under Centimeter-Scale, Single-Crystal Graphene Enables Electronic-Device Fabrication," *Nano Lett.*, vol. 20, no. 12, pp. 8584–8591, Dec. 2020, doi: 10.1021/acs.nanolett.0c03254.

[24] A. K. Grebenko *et al.*, "High-Quality Graphene Using Boudouard Reaction," *Adv. Sci.*, vol. 9, no. 12, p. 2200217, Apr. 2022, doi: 10.1002/advs.202200217.

[25] X. Li *et al.*, "Large-area synthesis of high-quality and uniform graphene films on copper foils," *Science (80-.).*, vol. 324, no. 5932, pp. 1312–1314, 2009, doi: 10.1126/science.1171245.

[26] J. Dauber *et al.*, "Ultra-sensitive Hall sensors based on graphene encapsulated in hexagonal boron nitride," *Appl. Phys. Lett.*, vol. 106, no. 19, p. 193501, May 2015, doi: 10.1063/1.4919897.

[27] B. T. Schaefer *et al.*, "Magnetic field detection limits for ultraclean graphene Hall sensors," *Nat. Commun.*, vol. 11, no. 1, p. 4163, Dec. 2020, doi: 10.1038/s41467-020-18007-5.

[28] D. Collomb, P. Li, and S. Bending, "Frontiers of graphene-based Hall-effect sensors," *J. Phys. Condens. Matter*, vol. 33, no. 24, p. 243002, Jun. 2021, doi: 10.1088/1361-648X/abf7e2.

[29] T. Kuila, S. Bose, P. Khanra, A. K. Mishra, N. H. Kim, and J. H. Lee, "Recent advances in graphene-based biosensors," *Biosens. Bioelectron.*, vol. 26, no. 12, pp. 4637–4648, Aug. 2011, doi: 10.1016/j.bios.2011.05.039.

[30] Y. Liu, X. Dong, and P. Chen, "Biological and chemical sensors based on graphene materials," *Chem. Soc. Rev.*, vol. 41, no. 6, pp. 2283–2307, 2012, doi: 10.1039/C1CS15270J.

[31] C. I. L. Justino, A. R. Gomes, A. C. Freitas, A. C. Duarte, and T. A. P. Rocha-Santos, "Graphene based sensors and biosensors," *TrAC Trends Anal. Chem.*, vol. 91, pp. 53–66, Jun. 2017, doi: 10.1016/j.trac.2017.04.003.

[32] J. Peña-Bahamonde, H. N. Nguyen, S. K. Fanourakis, and D. F. Rodrigues, "Recent advances in graphene-based biosensor technology with applications in life sciences," *J. Nanobiotechnology*, vol. 16, no. 1, p. 75, Dec. 2018, doi: 10.1186/s12951-018-0400-z.

[33] J. A. Alexander-Webber *et al.*, "Encapsulation of graphene transistors and vertical device integration by interface engineering with atomic layer deposited oxide," *2D Mater.*, vol. 4, no. 1, p. 011008, Nov. 2016, doi: 10.1088/2053-1583/4/1/011008.

[34]   A. Dankert, B. Karpiak, and S. P. Dash, "Hall sensors batch-fabricated on all-CVD h-BN/graphene/h-BN heterostructures," *Sci. Rep.*, vol. 7, no. 1, p. 15231, Dec. 2017, doi: 10.1038/s41598-017-12277-8.

[35]   G. Gu *et al.*, "Field effect in epitaxial graphene on a silicon carbide substrate," *Appl. Phys. Lett.*, vol. 90, no. 25, p. 253507, Jun. 2007, doi: 10.1063/1.2749839.

[36]   P. Li, R. Z. Zeng, Y. B. Liao, Q. W. Zhang, and J. H. Zhou, "A Novel Graphene Metal Semi-Insulator Semiconductor Transistor and Its New Super-Low Power Mechanism," *Sci. Rep.*, vol. 9, no. 1, Dec. 2019, doi: 10.1038/s41598-019-40104-9.

[37]   M. A. Brown, M. S. Crosser, M. R. Leyden, Y. Qi, and E. D. Minot, "Measurement of high carrier mobility in graphene in an aqueous electrolyte environment," *Appl. Phys. Lett.*, vol. 109, no. 9, p. 093104, Aug. 2016, doi: 10.1063/1.4962141.

[38]   W. Gannett, W. Regan, K. Watanabe, T. Taniguchi, M. F. Crommie, and A. Zettl, "Boron nitride substrates for high mobility chemical vapor deposited graphene," *Appl. Phys. Lett.*, vol. 98, no. 24, p. 242105, Jun. 2011, doi: 10.1063/1.3599708.

[39]   A. S. Mayorov *et al.*, "Micrometer-scale ballistic transport in encapsulated graphene at room temperature," *Nano Lett.*, vol. 11, no. 6, pp. 2396–2399, Jun. 2011, doi: 10.1021/nl200758b.

[40]   H. Yang *et al.*, "Two-dimensional materials prospects for non-volatile spintronic memories," *Nature*, vol. 606, no. 7915, pp. 663–673, 2022, doi: 10.1038/s41586-022-04768-0.

[41]   J.-F. Dayen, S. J. Ray, O. Karis, I. J. Vera-Marun, and M. V. Kamalakar, "Two-dimensional van der Waals spinterfaces and magnetic-interfaces," *Appl. Phys. Rev.*, vol. 7, no. 1, p. 011303, Mar. 2020, doi: 10.1063/1.5112171.

[42]   E. W. Hill, A. K. Geim, K. Novoselov, F. Schedin, and P. Blake, "Graphene Spin Valve Devices," *IEEE Trans. Magn.*, vol. 42, no. 10, pp. 2694–2696, Oct. 2006, doi: 10.1109/TMAG.2006.878852.

[43]   N. Tombros, C. Jozsa, M. Popinciuc, H. T. Jonkman, and B. J. van Wees, "Electronic spin transport and spin precession in single graphene layers at room temperature.," *Nature*, vol. 448, no. 7153, pp. 571–574, Aug. 2007, doi: 10.1038/nature06037.

[44]   S. Cho, Y. F. Chen, and M. S. Fuhrer, "Gate-tunable graphene spin valve," *Appl. Phys. Lett.*, vol. 91, no. 12, 2007, doi: 10.1063/1.2784934.

[45]   M. Ohishi, M. Shiraishi, R. Nouchi, T. Nozaki, T. Shinjo, and Y. Suzuki, "Spin Injection into a Graphene Thin Film at Room Temperature," *Jpn. J. Appl. Phys.*, vol. 46, no. No. 25, pp. L605–L607, Jun. 2007, doi: 10.1143/JJAP.46.L605.

[46]   M. H. D. Guimarães, P. J. Zomer, J. Ingla-Aynés, J. C. Brant, N. Tombros, and B. J. Van Wees, "Controlling spin relaxation in hexagonal BN-encapsulated graphene with a transverse electric field," *Phys. Rev. Lett.*, vol. 113, no. 8, pp. 1–5, 2014, doi: 10.1103/PhysRevLett.113.086602.

[47]   M. Gurram *et al.*, "Spin transport in two-layer-CVD-hBN/graphene/hBN heterostructures," *Phys. Rev. B*, vol. 97, no. 4, pp. 1–8, 2018, doi: 10.1103/PhysRevB.97.045411.

[48]   J. Ingla-Aynés, M. H. D. Guimarães, R. J. Meijerink, P. J. Zomer, and B. J. Van Wees, "24-micro miters Spin Relaxation Length in Boron Nitride Encapsulated Bilayer Graphene," *Phys. Rev. B - Condens. Matter Mater. Phys.*, vol. 92, no. 20, pp. 1–5, 2015, doi: 10.1103/PhysRevB.92.201410.

[49]   W. Han *et al.*, "Tunneling Spin Injection into Single Layer Graphene," *Phys. Rev.*

54

Lett., vol. 105, no. 16, p. 167202, Oct. 2010, doi: 10.1103/PhysRevLett.105.167202.

[50] M. Shiraishi, "Graphene spintronics," in *Graphene*, vol. 9, no. 10, Elsevier, 2014, pp. 324–340.

[51] F. Volmer *et al.*, "Role of MgO barriers for spin and charge transport in Co/MgO/graphene nonlocal spin-valve devices," *Phys. Rev. B*, vol. 88, no. 16, p. 161405, Oct. 2013, doi: 10.1103/PhysRevB.88.161405.

[52] D. Kochan, M. Gmitra, and J. Fabian, "Spin Relaxation Mechanism in Graphene: Resonant Scattering by Magnetic Impurities," *Phys. Rev. Lett.*, vol. 112, no. 11, p. 116602, Mar. 2014, doi: 10.1103/PhysRevLett.112.116602.

[53] I. G. Serrano *et al.*, "Two-Dimensional Flexible High Diffusive Spin Circuits," *Nano Lett.*, vol. 19, no. 2, pp. 666–673, Feb. 2019, doi: 10.1021/acs.nanolett.8b03520.

[54] P. R. Whelan *et al.*, "Fermi velocity renormalization in graphene probed by terahertz time-domain spectroscopy," *2D Mater.*, vol. 7, no. 3, 2020, doi: 10.1088/2053-1583/ab81b0.

[55] I. G. Serrano, J. Panda, T. Edvinsson, and M. V. Kamalakar, "Flexible transparent graphene laminates: Via direct lamination of graphene onto polyethylene naphthalate substrates," *Nanoscale Adv.*, vol. 2, no. 8, pp. 3156–3163, 2020, doi: 10.1039/d0na00046a.

[56] A. Avsar *et al.*, "Toward Wafer Scale Fabrication of Graphene Based Spin Valve Devices," *Nano Lett*, vol. 11, pp. 2363–2368, 2011, doi: 10.1021/nl200714q.

[57] M. Dro *et al.*, "Nanosecond Spin Lifetimes in Single-and Few-Layer Graphene–hBN Heterostructures at Room Temperature," 2014, doi: 10.1021/nl501278c.

[58] V. E. Calado *et al.*, "Ballistic transppport in graphene grown by chemical vapor deposition," *Appl. Phys. Lett*, vol. 104, p. 23103, 2014, doi: 10.1063/1.4861627.

[59] M. Schmitz *et al.*, "High mobility dry-transferred CVD bilayer graphene," *Appl. Phys. Lett*, vol. 110, p. 263110, 2017, doi: 10.1063/1.4990390.

[60] D. De Fazio *et al.*, "High-Mobility, Wet-Transferred Graphene Grown by Chemical Vapor Deposition," *ACS Nano*, vol. 13, no. 8, pp. 8926–8935, Aug. 2019, doi: 10.1021/acsnano.9b02621.

[61] L. Banszerus *et al.*, "Ultrahigh-mobility graphene devices from chemical vapor deposition on reusable copper," doi: 10.1126/sciadv.1500222.

[62] M. Drögeler *et al.*, "Spin Lifetimes Exceeding 12 ns in Graphene Nonlocal Spin Valve Devices," *Nano Lett.*, vol. 16, no. 6, pp. 3533–3539, Jun. 2016, doi: 10.1021/acs.nanolett.6b00497.

[63] M. V. Kamalakar, C. Groenveld, A. Dankert, and S. P. Dash, "Long distance spin communication in chemical vapour deposited graphene," *Nat. Commun.*, vol. 6, 2015, doi: 10.1038/ncomms7766.

[64] A. Avsar *et al.*, "Toward wafer scale fabrication of graphene based spin valve devices," *Nano Lett.*, vol. 11, no. 6, pp. 2363–2368, 2011, doi: 10.1021/nl200714q.

[65] D. Khokhriakov, B. Karpiak, A. M. Hoque, and S. P. Dash, "Two-dimensional spintronic circuit architectures on large scale graphene," *Carbon N. Y.*, vol. 161, pp. 892–899, 2020, doi: 10.1016/j.carbon.2020.01.103.

[66] Z. M. Gebeyehu *et al.*, "Spin communication over 30 μm long channels of chemical vapor deposited graphene on SiO2," *2D Mater.*, vol. 6, no. 3, 2019, doi: 10.1088/2053-1583/ab1874.

[67]   W. Fu, P. Makk, R. Maurand, M. Bräuninger, and C. Schönenberger, "Large-scale fabrication of BN tunnel barriers for graphene spintronics," *J. Appl. Phys.*, vol. 116, no. 7, 2014, doi: 10.1063/1.4893578.

[68]   M. Drögeler *et al.*, "Dry-transferred CVD graphene for inverted spin valve devices," *Appl. Phys. Lett.*, vol. 111, no. 15, p. 152402, Oct. 2017, doi: 10.1063/1.5000545.

[69]   T. Bisswanger *et al.*, "CVD Bilayer Graphene Spin Valves with 26 µm Spin Diffusion Length at Room Temperature," *Nano Lett.*, vol. 22, no. 12, pp. 4949–4955, 2022, doi: 10.1021/acs.nanolett.2c01119.

[70]   H. Mishra *et al.*, "Experimental advances in Charge and Spin Transport in Chemical Vapor Deposited Graphene," *J. Phys. Mater.*, vol. 27, no. xxxx, pp. 0–31, Jul. 2021, doi: 10.1088/2515-7639/ac1247.

[71]   F. Godel, M. V. Kamalakar, B. Doudin, Y. Henry, D. Halley, and J.-F. Dayen, "Voltage-controlled inversion of tunnel magnetoresistance in epitaxial nickel/graphene/MgO/cobalt junctions," *Appl. Phys. Lett.*, vol. 105, no. 15, p. 152407, Oct. 2014, doi: 10.1063/1.4898587.

[72]   B. Dlubak *et al.*, "Highly efficient spin transport in epitaxial graphene on SiC," *Nat. Phys.*, vol. 8, no. 7, pp. 557–561, Jul. 2012, doi: 10.1038/nphys2331.

[73]   C. K. Safeer *et al.*, "Room-Temperature Spin Hall Effect in Graphene/MoS2 van der Waals Heterostructures," *Nano Lett.*, 2019, doi: 10.1021/acs.nanolett.8b04368.

[74]   M. Z. Iqbal, S. Siddique, and A. Rehman, "Enhanced intervalley scattering of aluminum oxide-deposited graphene," *Carbon N. Y.*, vol. 124, pp. 188–192, 2017, doi: 10.1016/j.carbon.2017.07.067.

[75]   J. Panda, M. Ramu, O. Karis, T. Sarkar, and M. V. Kamalakar, "Ultimate Spin Currents in Commercial Chemical Vapor Deposited Graphene," *ACS Nano*, vol. 14, no. 10, pp. 12771–12780, 2020, doi: 10.1021/acsnano.0c03376.

[76]   M. Popinciuc *et al.*, "Electronic spin transport in graphene field-effect transistors," *Phys. Rev. B*, vol. 80, no. 21, p. 214427, Dec. 2009, doi: 10.1103/PhysRevB.80.214427.

[77]   T. Yamaguchi, S. Masubuchi, K. Iguchi, R. Moriya, and T. Machida, "Tunnel spin injection into graphene using Al2O3 barrier grown by atomic layer deposition on functionalized graphene surface," *J. Magn. Magn. Mater.*, vol. 324, no. 5, pp. 849–852, 2012.

[78]   G. Stecklein, P. A. Crowell, J. Li, Y. Anugrah, Q. Su, and S. J. Koester, "Contact-Induced Spin Relaxation in Graphene Nonlocal Spin Valves," *Phys. Rev. Appl.*, vol. 6, no. 5, pp. 1–11, 2016, doi: 10.1103/PhysRevApplied.6.054015.

[79]   Y. Anugrah, J. Hu, G. Stecklein, P. A. Crowell, and S. J. Koester, "Independent gate control of injected and detected spin currents in CVD graphene nonlocal spin valves," *AIP Adv.*, vol. 8, no. 1, 2018, doi: 10.1063/1.5008761.

[80]   R. Murali, Y. Yang, K. Brenner, T. Beck, and J. D. Meindl, "Breakdown current density of graphene nanoribbons," *Appl. Phys. Lett.*, vol. 94, no. 24, pp. 2007–2010, 2009, doi: 10.1063/1.3147183.

[81]   K. S. Novoselov *et al.*, "Unconventional quantum Hall effect and Berry's phase of 2π in bilayer graphene," *Nat. Phys.*, vol. 2, no. 3, pp. 177–180, Mar. 2006, doi: 10.1038/nphys245.

[82]   K. J. Lee, A. P. Chandrakasan, and J. Kong, "Breakdown current density of CVD-grown multilayer graphene interconnects," *IEEE Electron Device Lett.*, vol. 32, no. 4, pp. 557–559, 2011, doi: 10.1109/LED.2011.2108259.

[83]   J. Hodkiewicz and T. F. Scientific, "The Importance of Tight Laser Power Control When Working with Carbon Nanomaterials," vol. 60.

[84]   A. C. F. and J. Robertson, "Interpretation of Raman spectra of disordered and amorphous carbon," *Phys. Rev. B*, vol. 31, no. 2, pp. 632–645, 2000, doi: 10.1007/BF02543692.

[85]   A. C. Ferrari *et al.*, "Raman spectrum of graphene and graphene layers," *Phys. Rev. Lett.*, vol. 97, no. 18, pp. 1–4, 2006, doi: 10.1103/PhysRevLett.97.187401.

[86]   L. G. Caṇado *et al.*, "General equation for the determination of the crystallite size la of nanographite by Raman spectroscopy," *Appl. Phys. Lett.*, vol. 88, no. 16, pp. 1–4, 2006, doi: 10.1063/1.2196057.

[87]   L. G. Cançado, A. Jorio, and M. A. Pimenta, "Measuring the absolute Raman cross section of nanographites as a function of laser energy and crystallite size," *Phys. Rev. B - Condens. Matter Mater. Phys.*, vol. 76, no. 6, pp. 1–7, 2007, doi: 10.1103/PhysRevB.76.064304.

[88]   R. H. Fowler and L. Nordheim, "Electron Emission in Intense Electric Fields," *R. Soc.*, vol. 14, no. 1923, pp. 683–691, 1928, doi: 10.1142/9789814503464_0087.

[89]   J. Yan and M. S. Fuhrer, "Correlated charged impurity scattering in graphene," *Phys. Rev. Lett.*, vol. 107, no. 20, pp. 1–24, 2011, doi: 10.1103/PhysRevLett.107.206601.

[90]   S. Adam, E. H. Hwang, V. M. Galitski, and S. Das Sarma, "A self-consistent theory for graphene transport," *Proc. Natl. Acad. Sci. U. S. A.*, vol. 104, no. 47, pp. 18392–18397, 2007, doi: 10.1073/pnas.0704772104.

[91]   Y. Wu *et al.*, "State-of-the-Art Graphene High-Frequency Electronics," 2012.

[92]   M. A. Giambra *et al.*, "Graphene Field-Effect Transistors Employing Different Thin Oxide Films: A Comparative Study," *ACS Omega*, vol. 4, no. 1, pp. 2256–2260, Jan. 2019, doi: 10.1021/acsomega.8b02836.

[93]   Q. A. Vu *et al.*, "A High-On/Off-Ratio Floating-Gate Memristor Array on a Flexible Substrate via CVD-Grown Large-Area 2D Layer Stacking," *Adv. Mater.*, vol. 29, no. 44, Nov. 2017, doi: 10.1002/adma.201703363.

[94]   Y. J. Huang and S. C. Lee, "Graphene/h-BN Heterostructures for Vertical Architecture of RRAM Design," *Sci. Rep.*, vol. 7, no. 1, pp. 1–9, 2017, doi: 10.1038/s41598-017-08939-2.

[95]   S. Lee, J. Sohn, Z. Jiang, H. Y. Chen, and H. S. Philip Wong, "Metal oxide-resistive memory using graphene-edge electrodes," *Nat. Commun.*, vol. 6, pp. 1–7, 2015, doi: 10.1038/ncomms9407.

[96]   Y. Feng, D. J. Trainer, and K. Chen, "Graphene tunnel junctions with aluminum oxide barrier," *J. Appl. Phys.*, vol. 120, no. 16, 2016, doi: 10.1063/1.4966572.

[97]   Y. Ren, S. Chen, W. Cai, Y. Zhu, C. Zhu, and R. S. Ruoff, "Controlling the electrical transport properties of graphene by in situ metal deposition," *Appl. Phys. Lett.*, vol. 97, no. 5, pp. 1–4, 2010, doi: 10.1063/1.3471396.

[98]   G. Giovannetti, P. A. Khomyakov, G. Brocks, V. M. Karpan, J. Van Den Brink, and P. J. Kelly, "Doping graphene with metal contacts," *Phys. Rev. Lett.*, vol. 101, no. 2, pp. 4–7, 2008, doi: 10.1103/PhysRevLett.101.026803.

[99]   C. H. Hu, Y. Zheng, Y. Zhang, S. Q. Wu, Y. H. Wen, and Z. Z. Zhu, "Electronic and magnetic properties of silicon adsorption on graphene," *Solid State Commun.*, vol. 151, no. 17, pp. 1128–1130, 2011, doi: 10.1016/j.ssc.2011.05.027.

[100]   J. H. Chen, C. Jang, S. Adam, M. S. Fuhrer, E. D. Williams, and M. Ishigami, "Charged-impurity scattering in graphene," *Nat. Phys.*, vol. 4, no. 5, pp. 377–381, 2008, doi: 10.1038/nphys935.

[101]   C. Jang, S. Adam, J. H. Chen, E. D. Williams, S. Das Sarma, and M. S. Fuhrer, "Tuning the effective fine structure constant in graphene: Opposing effects of dielectric screening on short- and long-range potential scattering," *Phys. Rev. Lett.*, vol. 101, no. 14, pp. 1–4, 2008, doi: 10.1103/PhysRevLett.101.146805.

[102]   D. Briggs, "X-ray photoelectron spectroscopy (XPS)," *Handb. Adhes. Second Ed.*, pp. 621–622, 2005, doi: 10.1002/0470014229.ch22.

[103]   J. M. Chappé *et al.*, "Analysis of multifunctional titanium oxycarbide films as a function of oxygen addition," *Surf. Coatings Technol.*, vol. 206, no. 8–9, pp. 2525–2534, 2012, doi: 10.1016/j.surfcoat.2011.11.005.

[104]   A. Das *et al.*, "Monitoring dopants by Raman scattering in an electrochemically top-gated graphene transistor," *Nat. Nanotechnol.*, vol. 3, no. 4, pp. 210–215, 2008, doi: 10.1038/nnano.2008.67.

[105]   X. Li *et al.*, "Large-area synthesis of high-quality and uniform graphene films on copper foils.," *Science*, vol. 324, no. 5932, pp. 1312–4, Jun. 2009, doi: 10.1126/science.1171245.

[106]   M. Bokdam, P. A. Khomyakov, G. Brocks, and P. J. Kelly, "Field effect doping of graphene in metal|dielectric|graphene heterostructures: A model based upon first-principles calculations," *Phys. Rev. B - Condens. Matter Mater. Phys.*, vol. 87, no. 7, pp. 1–13, 2013, doi: 10.1103/PhysRevB.87.075414.

[107]   J. Moser, A. Barreiro, and A. Bachtold, "Current-induced cleaning of graphene," *Appl. Phys. Lett.*, vol. 91, no. 16, pp. 1–4, 2007, doi: 10.1063/1.2789673.

[108]   S. Debroy, S. Sivasubramani, G. Vaidya, S. G. Acharyya, and A. Acharyya, "Temperature and Size Effect on the Electrical Properties of Monolayer Graphene based Interconnects for Next Generation MQCA based Nanoelectronics," *Sci. Rep.*, vol. 10, no. 1, pp. 1–11, 2020, doi: 10.1038/s41598-020-63360-6.

[109]   T. Yu, E. K. Lee, B. Briggs, B. Nagabhirava, and B. Yu, "Bilayer graphene system: Current-induced reliability limit," *IEEE Electron Device Lett.*, vol. 31, no. 10, pp. 1155–1157, 2010, doi: 10.1109/LED.2010.2058994.

[110]   H. Mishra *et al.*, "Experimental advances in Charge and Spin Transport in Chemical Vapor Deposited Graphene," *J. Phys. Mater.*, vol. 27, no. xxxx, pp. 0–31, Jul. 2021, doi: 10.1088/2515-7639/ac1247.

[111]   M. V. Kamalakar, A. Dankert, J. Bergsten, T. Ive, and S. P. Dash, "Enhanced Tunnel Spin Injection into Graphene using Chemical Vapor Deposited Hexagonal Boron Nitride," *Sci. Rep.*, vol. 4, p. 6146, Aug. 2014, doi: 10.1038/srep06146.

[112]   M. V. Kamalakar, A. Dankert, P. J. Kelly, and S. P. Dash, "Inversion of Spin Signal and Spin Filtering in Ferromagnet|Hexagonal Boron Nitride-Graphene van der Waals Heterostructures," *Sci. Rep.*, vol. 6, p. 21168, Feb. 2016, doi: 10.1038/srep21168.

[113]   M. Gurram, S. Omar, and B. J. van Wees, "Electrical spin injection, transport, and detection in graphene-hexagonal boron nitride van der Waals heterostructures: progress and perspectives," *2D Mater.*, vol. 5, p. 032004, 2018, doi: 10.1088/2053-1583/aac34d.

[114]   A. L. Friedman, O. M. J. van 't Erve, C. H. Li, J. T. Robinson, and B. T. Jonker, "Homoepitaxial tunnel barriers with functionalized graphene-on-graphene for charge and spin transport.," *Nat. Commun.*, vol. 5, p. 3161, Jan. 2014, doi: 10.1038/ncomms4161.

Paper I

Research Article

Insights and Implications of Intricate Surface Charge Transfer and sp³-Defects in Graphene/Metal Oxide Interfaces

Daria Belotcerkovtceva, Renan P. Maciel, Elin Berggren, Ramu Maddu, Tapati Sarkar, Yaroslav O. Kvashnin, Danny Thonig, Andreas Lindblad, Olle Eriksson, and M. Venkata Kamalakar*

Read Online

ACCESS | Metrics & More | Article Recommendations | Supporting Information

ABSTRACT: Adherence of metal oxides to graphene is of fundamental significance to graphene nanoelectronic and spintronic interfaces. Titanium oxide and aluminum oxide are two widely used tunnel barriers in such devices, which offer optimum interface resistance and distinct interface conditions that govern transport parameters and device performance. Here, we reveal a fundamental difference in how these metal oxides interface with graphene through electrical transport measurements and Raman and photoelectron spectroscopies, combined with ab initio electronic structure calculations of such interfaces. While both oxide layers cause surface charge transfer induced p-type doping in graphene, in sharp contrast to TiO_x, the AlO_x/graphene interface shows the presence of appreciable sp³ defects. Electronic structure calculations disclose that significant p-type doping occurs due to a combination of sp³ bonds formed between C and O atoms at the interface and possible slightly off-stoichiometric defects of the aluminum oxide layer. Furthermore, the sp³ hybridization at the AlO_x/graphene interface leads to distinct magnetic moments of unsaturated bonds, which not only explicates the widely observed low spin-lifetimes in AlO_x barrier graphene spintronic devices but also suggests possibilities for new hybrid resistive switching and spin valves.

KEYWORDS: graphene, charge transfer, graphene electronics, spintronics, sp³-defects

■ INTRODUCTION

Graphene has evolved into an ideal medium for quantum and spin transport applications and a unique integration platform for complex heterostructures with other two-dimensional (2D) materials.[1,2] Recent developments show record quantum and spin transport performance that can be achieved in large-scale chemical vapor deposited (CVD) graphene, making it a prospective material for practical implementation into quantum and spin-integrated circuits.[3−5] Metal oxide interfaces are integral to graphene nanoelectronics and spintronic devices, ranging from memristors and single-electron transistors to tunnel field-effect transistors and graphene spin valves, where the interface nature guides their performance. In particular, titanium oxide and aluminum oxide have been widely used as tunnel barriers, primarily due to their efficacy and compatibility with device processing methods. Although ultrathin metal oxide layers can be directly realized using atomic-layer deposition or sputtering techniques, these techniques can lead to significant defects, impacting the overall structure and electrical nature of graphene.[6,7] Instead, Ti and Al are deposited using electron beam evaporation in graphene spin devices and are subsequently oxidized upon contact with air/O₂. In graphene electronic devices, metal oxides are used as gate dielectrics, effective barriers for graphene tunnel

junctions,[8] and thin-film memristive devices[9] for practical imitation of synaptic activities, where interface charge transfer and bonding can guide the resistive switching phenomena.[10] For both planar and vertical graphene spintronic devices,[11,12] ultrathin layers (∼nm thickness) of the metal oxides serve as tunnel barriers offering optimum interface resistance to overcome the conductivity mismatch problem associated with electrical spin injection.[13,14] However, obtaining faithful pinhole-free coverage is challenging for both aluminum and titanium oxides, prepared by e-beam evaporation and post-oxidation. In particular, compared to spin lifetimes up to ∼3.5 ns in graphene spintronic devices using TiO_x barriers,[15−17] the AlO_x-based devices widely show an order lower spin lifetime of ∼100 ps,[18−20] which has been generally attributed to the presence of pinholes, consequent current crowding, and contact-induced spin relaxation.[21,22] The one order lower performance of AlO_x-based devices remains

36209

puzzling, despite the same fabrication process and similar thicknesses of oxides. Therefore, understanding the physics governing graphene/metal-oxide interfaces is of fundamental significance to graphene nanoelectronic and spintronic devices. While metals and metal oxides on graphene introduce surface charge transfer p-type or n-type doping arising from the difference in the work function of the metal relative to graphene,[17,23,24] the situation is non-trivial for tunnel barrier oxides such as ultrathin TiO_x or AlO_x on graphene. Considering expected charge transfer effects, the redistribution of electron density after oxidation of metals is unclear, even from a theoretical perspective. In addition to surface charge-transfer doping, in-plane and out-of-plane defect-related doping in graphene can greatly influence charge and spin relaxation. The possibilities of introducing long-range and short-range scatterers, defects due to ultrathin oxide layers on graphene, and their direct influence on electrical properties of graphene and spin relaxation in tunnel transport through such barriers have never been explicit. This investigation aims to uncover, at an atomic level, the important differences in the nature of defects between Al oxide and Ti oxide adhering to graphene for their influence on electrical and spintronic performance.

■ MATERIALS AND METHODS

In this work, we explore the modifications in graphene due to its full coverage with metal oxides through electrical transport measurements, spectroscopic techniques, atomic force microscopy, and theoretical electronic structure calculations. To faithfully explore the extrinsic doping, defect effects, and their implications, we investigated the impact of TiO_x and AlO_x adsorption on the electronic properties of fully covered graphene. To understand the electronic alterations due to oxides, we measured electrical properties on the same devices before and after the oxide realization by metal deposition and oxidation. X-ray photoelectron spectroscopy (XPS) and Raman spectroscopy were used to determine the nature of doping and oxidation states of C, Al, and Ti in AlO_x- and TiO_x-covered graphene and their distinct interface behavior. The topography, probed by atomic force microscopy (AFM), shows characteristic features and coverage unique to each kind of oxide. We correlate these results with electronic structure calculations to understand the intricate interfacial properties and possible atomic and electronic configurations that lead to our experimental observations. Finally, we discuss how the interface defects observed in this study illuminate the current understanding of spin relaxation in the widely used tunnel barriers in graphene spintronics and lead to new implications for nanoelectronic and spintronic devices.

Figure 1 shows graphene field-effect devices used in our experiments before and after metal (metal oxide) realization on graphene. The first step in fabricating graphene devices is to pattern a graphene channel using optical lithography and Ar plasma etching, resulting in 5 μm wide graphene stripes. Following this, graphene devices were fabricated by electron beam lithography patterning, e-beam metal evaporation, and subsequent lift-off (details in the Supporting Information). Next, electrical measurements were performed on the resulting devices to obtain transport parameters of the pristine graphene channels. After these initial measurements, the devices were subjected to an additional layer of metal oxide by electron beam evaporation and oxidation in open air. The critical part of the procedure is the Ti or Al (0.8 nm) deposition on the same device and keeping the device working for repeated measurements with the metal oxide layers on top of graphene. This allowed us to understand the modification due to doping and possible defect creation in the same graphene stripes.
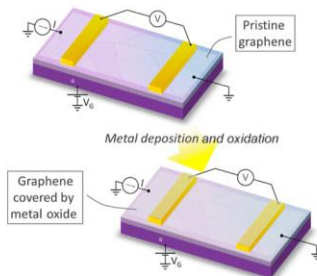

Figure 1. Experimental scheme of a graphene field-effect device before and after Al/Ti deposition and oxidation.

■ RESULTS AND DISCUSSION

The initial characterization of changes in the graphene properties was carried out by gate-dependent measurements of four-probe channel sheet-resistance ($R_\square$) with varying gate voltage (V_G). To determine the contribution stemming from graphene and graphene covered with TiO_x/AlO_x, Dirac curves were measured on the same devices before and after the deposition of the metals. As shown in Figure 2a,b, for both oxide layers, the charge neutrality point (CNP), that is, the Dirac point (V_D), shifts toward the positive gate voltage region. Such a shift means that these metal oxides cause a downward shift of the Fermi level in graphene, implying p-type doping. It is worth noting that the V_D shift (ΔV_D) is significant even with an ultrathin ~1 nm layer, and the interface trap density of states for the acceptor is affected by both types of oxides, as evidenced by ΔV_D. In Figure 2c−j, all electrical parameters are compared with pristine graphene to determine changes in a total of 12 devices measured here. Despite the huge variation in V_D (i.e., doping level), minimum conductivity (σ_0), and mobility (μ), both oxide-overlaid graphene samples show reasonably good values, and for most of the devices, the changes are moderately small (similar to or ~10% for most devices) from initial pristine graphene devices to graphene/oxide devices. Strikingly, the sheet resistance at the CNP is similar for graphene before and after metal oxide realization, indicating a minimum conductivity that remains reasonably intact (as shown in Figure 2i,j). The minimum conductivity at V_D for both oxides (Figure 2i,j) showed less than 5% change from pristine graphene samples. Furthermore, in the shape of the Dirac curves, the plateaus around the CNP in the metal oxide-covered devices are not appreciably different from those seen in the pristine devices. The analysis of Dirac curves reveals (see Supporting Information Figure S1) a low trap density in all samples, and the minor changes in electrical parameters after the realization of top oxide layers can be linked to modifications in long-range Coulomb scattering due to charged impurities[25] and the short-range defect scattering,[26] including possible sp^3 defects. Considering that Al and Ti metals result in n-type doping in graphene,[24,27,28] these observations suggest that the p-type doping of ~10^{12} to 10^{13} cm^{-2} (for change in ΔV_D of ~ 50−100 V) is primarily due to the surface charge transfer between the oxide layers and graphene for most devices. This means that the oxide layer coverage achieved by electron beam evaporation and

61
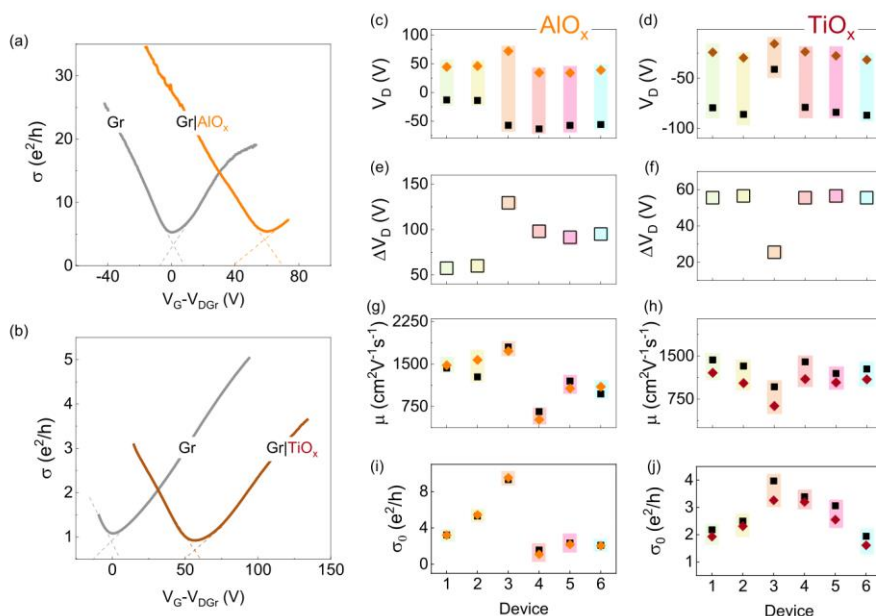
Figure 2. Electrical characteristics' modification for graphene devices with AlO_x and TiO_x layers. Gate-dependent conductivity (in units of quantum of conductance e^2/h) vs gate voltage (V_G). Dirac curves for the devices with graphene before (gray curve) and after (orange/brown curve) deposition of (a) AlO_x and (b) TiO_x. The dashed lines are provided here to guide Dirac point broadening. (c−j) Summary of Dirac point location (V_D) and its shift (ΔV_D), field-effect electron mobility (μ), minimum conductivity (σ_0) for pristine graphene (dark square), and AlO_x- and TiO_x-deposited (colored diamond) devices.
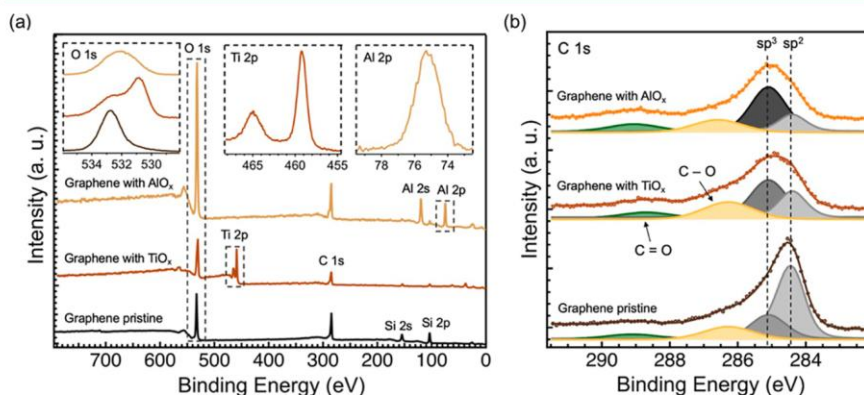
Figure 3. XPS characterization. (a) Overview spectra of pristine graphene (dark brown), graphene with deposited TiO_x (brown), and AlO_x (orange), and (b) C 1s components used for the least-squares fits. All spectra were obtained using a monochromatic Al K_α source. The binding energy is calibrated using the Si 2p peak at 103.3 eV in SiO_2[37] and the carbon sp^2 peak at 284.4 eV.[38,39]
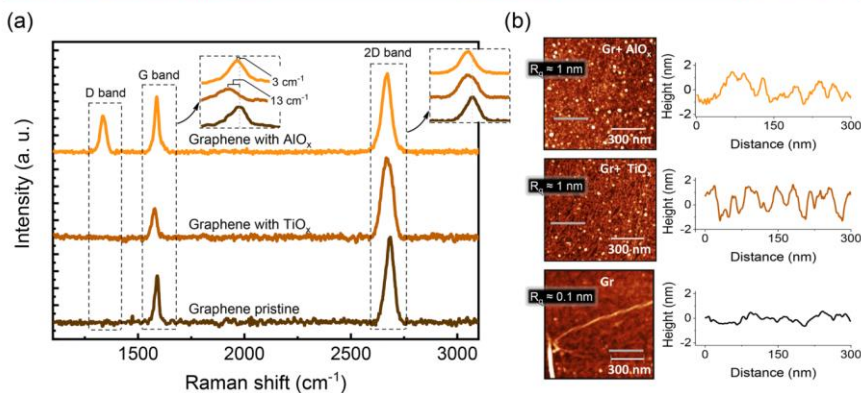
Figure 4. (a) Raman spectra of pristine graphene and graphene with deposited TiO_x and AlO_x along with insets showing shifts in G and 2D bands. (b) AFM images of representative graphene (Gr) and graphene after TiO_x (Gr + TiO_x) and AlO_x (Gr + AlO_x) deposition on top of it. The corresponding gray line scans show the roughness profiles, and R_q represents the average area roughness.

subsequent oxidation can be used to protect graphene without drastically altering its properties. The charge transfer serves as a tool to tune the carrier concentration faithfully. It is known that in-plane defects in graphene can lead to n-type doping,[29] which rules out such defects. However, in addition to charge-transfer doping, sp^3 out-of-plane defects could also lead to p-type doping[30] and can cause spin-flip scattering as well as spin precession relaxation in graphene. To further explore the nature of such defects, we performed XPS measurements (see sample characterization details in the Supporting Information) on our samples.

In Figure 3, the XPS data on pristine graphene and graphene with metal oxide layers are shown. The Al 2p spectrum (Figure 3a, upper right panel) shows a binding energy of 75 eV, suggesting that the deposited film is Al_2O_3.[31] The regional spectrum of Ti 2p (Figure 3a, central panel) shows a binding energy of 459 eV for the Ti $2p_{3/2}$ core level, corresponding to TiO_2.[32,33] This implies that both metals are nearly fully oxidized. The XPS spectra for C 1s core-level binding energy is shown in Figure 3b. The observed increase in binding energy for oxide-covered samples suggests a charge transfer from graphene to interface atoms, confirming p-type doping. Figure 3b shows that the pristine graphene sample exhibits an expected intense sp^2 contribution compared to graphene covered with metal oxides. The observed background contribution of sp^3 can come from other sources, such as resist residue and other C-species in the sample measurement environment. In sharp contrast, the Gr-AlO_x sample shows a dominating contribution from sp^3 defects (intensity ratio of $sp^3/sp^2 \approx 3$), which signals strong evidence of sp^3 defects created in the graphene lattice during the Al oxidation. Conversely, the transport parameters suggest that sp^2 contribution should maintain dominance even for Gr-AlO_x, so significant quenching of the signal of sp^2 contribution can be due to the added surface oxide layers. Unlike Gr-AlO_x samples, we observe a lower value of $sp^3/sp^2 \approx 1.6$ for Gr-TiO_x, suggesting a lower-level source of the sp^3 signal. Here, in our analysis, subtracting the sp^3 contributions of bare graphene

from our oxide samples can reveal some sp^3 contribution also in Gr-metal oxide samples. However, since each sample has its own background, for comparisons, we chose to look at the sp^3/sp^2 intensity ratios. Considering that high spin lifetimes were achieved with TiO_x tunnel barriers, the increased sp^3 intensity does not necessarily mean an sp^3 hybridization of the graphene lattice.[34] In fact, with a large 100 μm X-ray probe diameter, a significant sp^3 contribution can originate from the PMMA resist residues and related effects intrinsic to the CVD graphene transfer process[35,36] (similar to the sp^3 background in pristine graphene). This, and the possible reduction in sp^2 intensity due to oxide coverage, could increase the observed intensity at the sp^3 binding energy for Gr-TiO_x. Additionally, it is worth noting that surface carbon species bonded to oxygen atoms can have binding energies equivalent to those of sp^3-carbon,[34] which could further add to the surplus intensity at the sp^3 binding energy position for the Gr-TiO_x sample. Thus, the XPS measurements with large-area sampling give qualitative evidence of the presence of sp^3 carbon in the graphene lattice covered with AlO_x. On the other hand, large-area sampling can be circumvented by micro-Raman characterization. Figure 4 shows the Raman spectra obtained on pristine graphene and graphene with metal oxide layers. First, as shown in Figure 4, for pristine graphene, the well-known G and 2D mode features, with frequencies near 1584 and 2678 cm^{-1}, respectively, were obtained. The same peaks were also identified on the graphene samples with AlO_x or TiO_x layers, confirming the integrity of graphene sheets covered by oxide layers.

The ratio of the 2D peak to the G peak intensities (I_{2D}/I_G) is a parameter to determine the quality and monolayer structure of graphene.[40] Here, in pristine graphene and graphene with TiO_x, $I_{2D}/I_G \geq 2$ confirms the good quality of the CVD polycrystalline graphene that we employed in this study.[41] However, in the presence of AlO_x, graphene shows different behavior, with the value of I_{2D}/I_G significantly decreasing to 1.45, which suggests possible degradation of the sp^2 structure of graphene. In addition, the G peak's doping sensitivity helps

63

confirm the nature of doping. The location of the G peak for pristine graphene is 1590 cm^{-1}. For graphene coated with AlO$_x$, the peak shift was approximately 3 cm^{-1} and for the case of TiO$_x$, it was approximately 13 cm^{-1} compared with pristine graphene. A similar shift was also observed for the 2D peak. Such a Raman shift to the left in the oxide-layered graphene indicates a p-type doping effect, which is in good agreement with our transport and XPS measurements. However, in the case of aluminum oxide-covered graphene, strikingly, we observed the emergence of the D peak (near 1340 cm^{-1}), which is a signature of Raman-active defects in graphene, suggesting the introduction of appreciable sp^3 carbon defects, a source of graphene modification by AlO$_x$ only. Although Raman spectroscopy in most cases serves as a qualitative analysis, it is possible to quantify the presence of defects in graphene. Using the model proposed in literature,[42] we obtained the concentration of defects for a graphene sample with AlO$_x$ by extracting the G to D intensity ratio from the spectrum and the excitation laser wavelength (see Raman spectroscopy details in the Supporting Information). From the estimation, we found a concentration of defects for graphene with evaporated Al (0.8 nm) of ~1.4 × 10^{11} cm^{-2}, which is nearly one defect per 10,000 carbon atoms. As stated earlier, for a large shift in V_D of ~ 50−100 V, a corresponding doping of 10^{12} to 10^{13} cm^{-2} can be expected. Therefore, the significant doping is due to surface charge-transfer doping, while the sp^3-related defect contributions are up to 2 orders less, which is unique to the AlO$_x$-interfaced graphene. Despite the defects, the electrical properties of graphene are relatively preserved in graphene/AlO$_x$ devices. In graphene spintronic devices, the sp^3 defects are expected to contribute to spin relaxation, mainly when the electrical spin injection is carried out in graphene spintronic devices, resulting in significantly shorter spin lifetimes. This has been conventionally attributed to pinholes in the AlO$_x$ barrier. Density functional theory (DFT)-based electronic structure calculations showed that the interaction between graphene and metal oxides is weaker for Ti oxide than for Al oxide.[43] The Ti-donated electron charge density is highly localized around the neighboring carbon atoms, and titanium does not tend to form clusters, which is excepted to lead to uniform coverage.[44] To understand the surface morphology of the oxide coverage over graphene, we investigated the samples by AFM. We chose a 1 μm × 1 μm scan area to check the shape of the grains on top of the graphene surface and the height profile. Expectedly, there is a deviation from the smooth morphology of pristine graphene to graphene with the oxide layers. The common feature of oxide-covered graphene is the presence of ridges and grooves. The comparison between the surfaces is shown in Figure 4b. The AFM images show an alternation of dark and bright stripes in the case of Ti or circle-shaped dots in Al. The mean position was fixed to a 0 nm height in the height profile. Compared to the height profile with the standard topography of graphene, the oxide-covered graphene possesses a higher topographic root-mean-square roughness. While conspicuous pinholes can be identified from the deviation in the height profile and images for AlO$_x$, perceptible swings in the height profile are also observed in the Gr-TiO$_x$ system. One can attribute the other large clusters to possible resist residue regions observed in pristine graphene that can act as nucleation sites. Both oxides show an area roughness of R_q ~ 1 nm, suggesting that both Ti and Al deposited on graphene by e-beam evaporation and following oxidation of the metals do not necessarily lead to

full coverage, and hence, current crowding can be a common problem for both metal oxides. This leaves us with the additional sp^3 defects unique to AlO$_x$-layered graphene. Despite the XPS data indicating that Al and Ti are fully oxidized, we cannot assure perfect stoichiometric compositions leading to the observed charge-transfer doping in graphene. In particular, previous DFT calculations established charge transfer from graphene to titanium.[45,46] However, the charge transfer and sp^3 defect interface in graphene-Al oxide have not been addressed. To understand that on an atomic scale, we performed electronic structure calculations, shown in Figure 5.
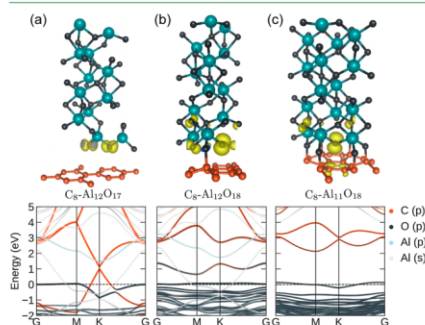
Figure 5. Simulated system's geometry (upper panel). The atoms Al, O, and C are represented by green, gray, and orange, respectively. The yellow clouds are the atom-projected magnetic moment densities of the crystal. The lower panel shows the projected band structure of (a) slightly off-stoichiometric aluminum oxide on graphene monolayer structures (C$_8$–Al$_{12}$O$_{17}$): the Fermi level shifts down in relation to the Dirac point and the unit cell magnetic moment is ~0.44 μ_B. (b) Perfect stoichiometry (C$_8$–Al$_{12}$O$_{18}$) giving rise to partially sp^3-bonded graphene leading to a local band gap opening and magnetic moments (0.61 μ_B per unit cell). (c) Electronic structure of graphene with sp^3-bonded C$_8$–Al$_{11}$O$_{18}$ where the unit cell magnetic moment is 1 μ_B. The s- and p-bands from Al crossing both the Dirac cone and Fermi level (gray colored bands) are due to dangling bonds at the very top surface of the composite.

Taking experimental conditions into account and using DFT calculations, we performed an interface study of the AlO$_x$ corundum α-phase with a hexagonal unit cell in contact with a graphene monolayer sheet. The AlO$_x$ slab structure can be arranged with different atomic terminations in proximity to graphene (e.g., oxygen or aluminum atom). Each case leads to varying results of the electronic property of the composite. Here, we only highlight three different interfaces (i.e., C$_8$−Al$_{12}$O$_{18}$, C$_8$−Al$_{11}$O$_{18}$, and C$_8$−Al$_{12}$O$_{17}$) where oxygen is in proximity to graphene and the total energy suggests stable or metastable geometries. For all cases, the geometry was relaxed following force minimization. For other geometries and details, see the Supporting Information. Figure 5 shows atomic and electronic structure results for AlO$_x$ layers on graphene using the experimental oxide layer thickness value of ~1 nm. Notably, calculations performed for the perfect stoichiometry (C$_8$−Al$_{12}$O$_{18}$), with graphene interfaced with aluminum atoms, did not yield any charge transfer and the Fermi level remained intact (see the Supporting Information). However, when oxygen atoms are in proximity to graphene, a strong

64

hybridization between the p-orbitals from oxygen and p_z-orbitals from carbon atoms causes the Dirac cone to be strongly distorted and positioned above the Fermi level.

Interestingly, calculations with a slight off-stoichiometry ($Al_{12}O_{17}$) give rise to systematic Fermi-level shifts of ~1 eV and p-doping with oxygen atoms closer to the graphene lattice (Figure 5a) without completely distorting or destroying the Dirac cone. In the process of e-beam evaporation of Al, the possibility of Al atoms scattered from the graphene lattice and the activated carbon atoms being susceptible to subsequent bonding with oxygen atoms cannot be ruled out. Our calculations suggest that oxygen atoms can also make sp^3 bonds with graphene, as shown in Figure 5b,c. The calculations reveal that p-type doping emerges due to the oxygen atoms next to the graphene layer. However, for stoichiometric and slightly off-stoichiometric Al_2O_3, even a few oxygen atoms firmly bound with the carbon atoms buckle the graphene layer locally and destroy the Dirac cone by inducing sp^3 states and a local band gap opening. For computational reasons, the number of sp^3 defects considered in the calculations is relatively high compared to experiments (where 1 out of 10,000 atoms have Raman-active sp^3 defects). Nevertheless, the presented calculations show how sp^3 bonds can induce significant band gap opening. The practical scenario for our samples prepared with CVD graphene can combine these two features with every 10,000th location featuring a band structure as in Figure 5c. Overall, our experiments reveal that sp^3-hybridized defect centers are a significant feature of AlO_x, which is expected to buckle graphene locally. Such buckling is known to introduce spin−orbit coupling[47] and magnetic moments.[48] Our calculations with both perfect stoichiometric and non-stoichiometric Al-oxide sp^3-bonded systems lead to an effective magnetic moment situated on unsaturated bonds, with values ranging from 0.44 μ_B (off-stoichiometric) to 1 μ_B (high-density sp^3-bonded lattice) per unit cell.

In this investigation, we observed that non-invasive e-beam-evaporated Al and Ti-based oxides with metals near full-oxidized states adhere in subtle ways to graphene. While both oxides cause surface charge-transfer doping, the sp^3 defects at the graphene/AlO_x interface can have significant implications for graphene spintronics, where spin currents are injected from a ferromagnet into graphene through the ultrathin oxide barrier. Spin−orbit coupling and local magnetic moments can dominate spin-flip and resonant scattering at graphene/AlO_x interfaces. Specifically, the resonant scattering with magnetic impurities has been considered responsible for observing low spin lifetimes of ~100 ps, widely observed in AlO_x barrier graphene spintronic devices.[49] With no magnetic ordering, the sparsely distributed sp^3-based magnetic moments can become an additional source of spin relaxation in AlO_x barrier-based devices, other than the previously attributed pinholes in Al-oxide barrier-based studies in graphene spintronics. Furthermore, our calculations show that despite these magnetic moments being predominantly concentrated at non-saturated bonds (as shown in Figure 5), they can nevertheless induce magnetization in a small region of the graphene sheet, implying a significant source of spin scattering at the interface. In graphene spintronics, although hydrogenated graphene displayed increased spin lifetime with a normal g-factor,[50] enhanced spin-scattering due to magnetic moment formation in graphene[51] and reduced spin lifetimes due to colossal spin−orbit coupling[52] have also been reported. Therefore, spin transport experiments with aluminum oxide-covered graphene

could provide further insights into such observations. At the same time, the sparse magnetic moments at graphene/AlO_x interfaces could be ordered in exotic heterostructures via proximity effects[11] for enhanced proximity-induced magnetism in graphene[11,53] and in a controlled manner for novel spin valves. For resistive switching devices, the sp^3 bonds can act as carrier traps for synaptic junctions, and oxygen ions in the AlO_x layer can be highly mobile in graphene and could form covalent bonds with the broken bonds of graphene for setting and resetting processes in memristive devices.[10] Thus, magnetic defects with exchange-biased layers show potential for hybrid multilevel spin valve-resistive switching random access memory devices.

■ CONCLUSIONS

In summary, we explored the subtle nature of ultrathin Al and Ti oxides interfacing with graphene. With similar coverage observed by AFM, electrical measurements revealed surface charge transfer p-type doping of ~10^{12} to 10^{13} cm^{-2} for both metal oxides, with reasonably preserved charge mobility and sheet resistance. However, X-ray photoelectron spectroscopy suggests an intricate nature of the doping, not just due to charge transfer from C-atoms but also due to significant sp^3 defects for Al-oxide. This is precisely confirmed by the emergence of the sp^3 defect-active Raman D band for Al-oxide-layered graphene, in sharp contrast to Ti-oxide-layered graphene, where the band was absent. Our electronic structure calculations suggest that the observed 100 ppm sp^3 defects originate from O bonding with C and an out-of-plane buckling of carbon atoms. Such defects in Al-oxide-layered graphene can lead to a local magnetic moment in ~0.5−1.0 μ_B, primarily located on unsaturated bonds of O atoms. In the Ti-oxide case, this moment is absent, which offers an explanation for the dramatic difference in spin lifetimes widely observed in devices with different oxide tunnel contacts. At the same time, these results provide new implications for developing unique interfaces for hybrid graphene resistive switching and spintronic devices.

■ ASSOCIATED CONTENT

ⓢ Supporting Information

The Supporting Information is available free of charge at https://pubs.acs.org/doi/10.1021/acsami.2c06626.

> Details of the device fabrication process; sample characterization using electrical measurements and analysis, Raman spectroscopy, AFM, and X-ray photoelectron spectroscopy; and computation details for aluminum oxide simulation with aluminum oxide interface construction, perfect stoichiometric AlO_x/graphene interface, a small concentration of sp^3 bond in perfect stoichiometric oxide, and slightly off-stoichiometric AlO_x/graphene interface (PDF)

■ AUTHOR INFORMATION

Corresponding Author

M. Venkata Kamalakar − *Department of Physics and Astronomy, Uppsala University, SE-751 20 Uppsala, Sweden;* ● orcid.org/0000-0003-2385-9267; Email: venkata.mutta@physics.uu.se

65

Authors

Daria Belotcerkovtceva − *Department of Physics and Astronomy, Uppsala University, SE-751 20 Uppsala, Sweden*

Renan P. Maciel − *Department of Physics and Astronomy, Uppsala University, SE-751 20 Uppsala, Sweden*

Elin Berggren − *Department of Physics and Astronomy, Uppsala University, SE-751 20 Uppsala, Sweden*

Ramu Maddu − *Department of Materials Science and Engineering, Uppsala University, SE-751 03 Uppsala, Sweden*

Tapati Sarkar − *Department of Materials Science and Engineering, Uppsala University, SE-751 03 Uppsala, Sweden;* ⊙ orcid.org/0000-0003-4754-2504

Yaroslav O. Kvashnin − *Department of Physics and Astronomy, Uppsala University, SE-751 20 Uppsala, Sweden*

Danny Thonig − *Department of Physics and Astronomy, Uppsala University, SE-751 20 Uppsala, Sweden; School of Science and Technology, Örebro University, SE-70182 Örebro, Sweden*

Andreas Lindblad − *Department of Physics and Astronomy, Uppsala University, SE-751 20 Uppsala, Sweden;* ⊙ orcid.org/0000-0002-9188-9604

Olle Eriksson − *Department of Physics and Astronomy, Uppsala University, SE-751 20 Uppsala, Sweden; School of Science and Technology, Örebro University, SE-70182 Örebro, Sweden*

Complete contact information is available at:
https://pubs.acs.org/10.1021/acsami.2c06626

Notes

The authors declare no competing financial interest.

■ REFERENCES

(1) Fiori, G.; Bonaccorso, F.; Iannaccone, G.; Palacios, T.; Neumaier, D.; Seabaugh, A.; Banerjee, S. K.; Colombo, L. Electronics Based on Two-Dimensional Materials. *Nat. Nanotechnol.* **2014**, *9*, 768−779.

(2) Avsar, A.; Ochoa, H.; Guinea, F.; Özyilmaz, B.; van Wees, B. J.; Vera-Marun, I. Colloquium : Spintronics in Graphene and Other Two-Dimensional Materials. *Rev. Mod. Phys.* **2020**, *92*, 021003.

(3) Mishra, H.; Panda, J.; Maddu, R.; Sarkar, T.; Dayen, J.-F.; Belotcerkovtceva, D.; Kamalakar, M. V. Experimental Advances in Charge and Spin Transport in Chemical Vapor Deposited Graphene. *J. Phys. Mater.* **2021**, *4*, 042007.

(4) Cummings, A. W.; Dubois, S. M.-M.; Charlier, J.-C.; Roche, S. Universal Spin Diffusion Length in Polycrystalline Graphene. *Nano Lett.* **2019**, *19*, 7418−7426.

(5) Cummings, A. W.; Duong, D. L.; Nguyen, V. L.; Van Tuan, D.; Kotakoski, J.; Barrios Vargas, J. E.; Lee, Y. H.; Roche, S. Charge Transport in Polycrystalline Graphene: Challenges and Opportunities. *Adv. Mater.* **2014**, *26*, 5079−5094.

(6) Dlubak, B.; Seneor, P.; Anane, A.; Barraud, C.; Deranlot, C.; Deneuve, D.; Servet, B.; Mattana, R.; Petroff, F.; Fert, A. Are Al2 O3 and MgO Tunnel Barriers Suitable for Spin Injection in Graphene? *Appl. Phys. Lett.* **2010**, *97*, 092502.

(7) Martin, M.-B.; Dlubak, B.; Weatherup, R. S.; Yang, H.; Deranlot, C.; Bouzehouane, K.; Petroff, F.; Anane, A.; Hofmann, S.; Robertson, J.; Fert, A.; Seneor, P. Sub-Nanometer Atomic Layer Deposition for Spintronics in Magnetic Tunnel Junctions Based on Graphene Spin-Filtering Membranes. *ACS Nano* **2014**, *8*, 7890−7895.

(8) Feng, Y.; Trainer, D. J.; Chen, K. Graphene Tunnel Junctions with Aluminum Oxide Barrier. *J. Appl. Phys.* **2016**, *120*, 164505.

(9) Vu, Q. A.; Kim, H.; Nguyen, V. L.; Won, U. Y.; Adhikari, S.; Kim, K.; Lee, Y. H.; Yu, W. J. A High-On/Off-Ratio Floating-Gate Memristor Array on a Flexible Substrate via CVD-Grown Large-Area 2D Layer Stacking. *Adv. Mater.* **2017**, *29*, 1703363.

(10) Huang, Y.-J.; Lee, S. C. Graphene/h-BN Heterostructures for Vertical Architecture of RRAM Design. *Sci. Rep.* **2017**, *7*, 9679.

(11) Dayen, J.-F.; Ray, S. J.; Karis, O.; Vera-Marun, I. J.; Kamalakar, M. V. Two-Dimensional van Der Waals Spinterfaces and Magnetic-Interfaces. *Appl. Phys. Rev.* **2020**, *7*, 011303.

(12) Godel, F.; Venkata Kamalakar, M. V.; Doudin, B.; Henry, Y.; Halley, D.; Dayen, J.-F. Voltage-Controlled Inversion of Tunnel Magnetoresistance in Epitaxial Nickel/Graphene/MgO/Cobalt Junctions. *Appl. Phys. Lett.* **2014**, *105*, 152407.

(13) Dlubak, B.; Martin, M.-B.; Deranlot, C.; Servet, B.; Xavier, S.; Mattana, R.; Sprinkle, M.; Berger, C.; De Heer, W. a.; Petroff, F.; Anane, A.; Seneor, P.; Fert, A. Highly Efficient Spin Transport in Epitaxial Graphene on SiC. *Nat. Phys.* **2012**, *8*, 557−561.

(14) Han, W.; Pi, K.; McCreary, K. M.; Li, Y.; Wong, J. J. I.; Swartz, a. G.; Kawakami, R. K. Tunneling Spin Injection into Single Layer Graphene. *Phys. Rev. Lett.* **2010**, *105*, 167202.

(15) Kamalakar, M. V.; Groenveld, C.; Dankert, A.; Dash, S. P. Long Distance Spin Communication in Chemical Vapour Deposited Graphene. *Nat. Commun.* **2015**, *6*, 6766.

(16) Gebeyehu, Z. M.; Parui, S.; Sierra, J. F.; Timmermans, M.; Esplandiu, M. J.; Brems, S.; Huyghebaert, C.; Garello, K.; Costache, M. V.; Valenzuela, S. O. Spin communication over 30 μm long channels of chemical vapor deposited graphene on SiO 2. *2D Mater* **2019**, *6*, 034003.

(17) Panda, J.; Ramu, M.; Karis, O.; Sarkar, T.; Kamalakar, M. V. Ultimate Spin Currents in Commercial Chemical Vapor Deposited Graphene. *ACS Nano* **2020**, *14*, 12771−12780.

(18) Tombros, N.; Jozsa, C.; Popinciuc, M.; Jonkman, H. T.; van Wees, B. J. Electronic Spin Transport and Spin Precession in Single Graphene Layers at Room Temperature. *Nature* **2007**, *448*, 571−574.

(19) Popinciuc, M.; Józsa, C.; Zomer, P. J.; Tombros, N.; Veligura, A.; Jonkman, H. T.; van Wees, B. J. Electronic Spin Transport in Graphene Field-Effect Transistors. *Phys. Rev. B: Condens. Matter Mater. Phys.* **2009**, *80*, 214427.

(20) Yamaguchi, T.; Masubuchi, S.; Iguchi, K.; Moriya, R.; Machida, T. Tunnel Spin Injection into Graphene Using Al2O3 Barrier Grown by Atomic Layer Deposition on Functionalized Graphene Surface. *J. Magn. Magn. Mater.* **2012**, *324*, 849−852.

(21) Stecklein, G.; Crowell, P. A.; Li, J.; Anugrah, Y.; Su, Q.; Koester, S. J. Contact-Induced Spin Relaxation in Graphene Nonlocal Spin Valves. *Phys. Rev. Appl.* **2016**, *6*, 054015.

(22) Anugrah, Y.; Hu, J.; Stecklein, G.; Crowell, P. A.; Koester, S. J. Independent Gate Control of Injected and Detected Spin Currents in CVD Graphene Nonlocal Spin Valves. *AIP Adv.* **2018**, *8*, 015129.

(23) Ren, Y.; Chen, S.; Cai, W.; Zhu, Y.; Zhu, C.; Ruoff, R. S. Controlling the Electrical Transport Properties of Graphene by in Situ Metal Deposition. *Appl. Phys. Lett.* **2010**, *97*, 053107.

(24) Giovannetti, G.; Khomyakov, P. A.; Brocks, G.; Karpan, V. M.; van den Brink, J.; Kelly, P. J. Doping Graphene with Metal Contacts. *Phys. Rev. Lett.* **2008**, *101*, 026803.

(25) Chen, J. H.; Jang, C.; Adam, S.; Fuhrer, M. S.; Williams, E. D.; Ishigami, M. Charged-Impurity Scattering in Graphene. *Nat. Phys.* **2008**, *4*, 377−381.

66

(26) Jang, C.; Adam, S.; Chen, J. H.; Williams, E. D.; Das Sarma, S.; Fuhrer, M. S. Tuning the Effective Fine Structure Constant in Graphene: Opposing Effects of Dielectric Screening on Short- and Long-Range Potential Scattering. *Phys. Rev. Lett.* **2008**, *101*, 146805.

(27) Caridad, J. M.; Connaughton, S.; Ott, C.; Weber, H. B.; Krstić, V. An Electrical Analogy to Mie Scattering. *Nat. Commun.* **2016**, *7*, 12894.

(28) Shi, X.; Dong, G.; Fang, M.; Wang, F.; Lin, H.; Yen, W. C.; Chan, K. S.; Chueh, Y. L.; Ho, J. C. Selective N-Type Doping in Graphene via the Aluminium Nanoparticle Decoration Approach. *J. Mater. Chem. C* **2014**, *2*, 5417−5421.

(29) Mackenzie, D. M. A.; Galbiati, M.; De Cerio, X. D.; Sahalianov, I. Y.; Radchenko, T. M.; Sun, J.; Pena, D.; Gammelgaard, L.; Jessen, B. S.; Thomsen, J. D.; Bøggild, P.; Garcia-Lekue, A.; Camilli, L.; Caridad, J. M. Unraveling the Electronic Properties of Graphene with Substitutional Oxygen. *2D Mater* **2021**, *8*, 045035.

(30) Childres, I.; Jauregui, L. A.; Tian, J.; Chen, Y. P. Effect of Oxygen Plasma Etching on Graphene Studied Using Raman Spectroscopy and Electronic Transport Measurements. *New J. Phys.* **2011**, *13*, 025008.

(31) Tateno, Y.; Mitsuhashi, F.; Adachi, M.; Yonemura, T.; Saito, Y.; Yamamoto, Y.; Nakabayashi, T. An Investigation to Determine the Interface Condition between Graphene and Aluminum Oxide. *Jpn. J. Appl. Phys.* **2020**, *59*, 124001.

(32) Zhang, L.; Koka, R. V. A Study on the Oxidation and Carbon Diffusion of TiC in Alumina-Titanium Carbide Ceramics Using XPS and Raman Spectroscopy. *Mater. Chem. Phys.* **1998**, *57*, 23−32.

(33) Moulder, J. F.; Stickle, W. F.; Sobol, P. E.; Bomben, K. D. *Handbook of X-Ray Photoelectron Spectroscopy: A Reference Book of Standard Spectra for Identification and Interpretation of XPS Data*; Physical Electronics Division, Perkin-Elmer Corporation, 1992.

(34) Chappé, J. M.; Fernandes, A. C.; Moura, C.; Alves, E.; Barradas, N. P.; Martin, N.; Espinós, J. P.; Vaz, F. Analysis of Multifunctional Titanium Oxycarbide Films as a Function of Oxygen Addition. *Surf. Coat. Technol.* **2012**, *206*, 2525−2534.

(35) Ryu, S.; Liu, L.; Berciaud, S.; Yu, Y. J.; Liu, H.; Kim, P.; Flynn, G. W.; Brus, L. E. Atmospheric Oxygen Binding and Hole Doping in Deformed Graphene on a SiO2 Substrate. *Nano Lett.* **2010**, *10*, 4944−4951.

(36) Gammelgaard, L.; Caridad, J. M.; Cagliani, A.; Mackenzie, D. M. A.; Petersen, D. H.; Booth, T. J.; Bøggild, P. Graphene Transport Properties upon Exposure to PMMA Processing and Heat Treatments. *2D Mater.* **2014**, *1*, 035005.

(37) Leszczynski, J. *Handbook of Computational Chemistry*; Springer Science & Business Media, 2012.

(38) Haubner, K.; Murawski, J.; Olk, P.; Eng, L. M.; Ziegler, C.; Adolphi, B.; Jaehne, E. The Route to Functional Graphene Oxide. *ChemPhysChem* **2010**, *11*, 2131−2139.

(39) Lesiak, B.; Kövér, L.; Tóth, J.; Zemek, J.; Jiricek, P.; Kromka, A.; Rangam, N. C Sp 2 /Sp 3 Hybridisations in Carbon Nanomaterials − XPS and (X)AES Study. *Appl. Surf. Sci.* **2018**, *452*, 223−231.

(40) Das, A.; Pisana, S.; Chakraborty, B.; Piscanec, S.; Saha, S. K.; Waghmare, U. V.; Novoselov, K. S.; Krishnamurthy, H. R.; Geim, A. K.; Ferrari, A. C.; Sood, A. K. Monitoring Dopants by Raman Scattering in an Electrochemically Top-Gated Graphene Transistor. *Nat. Nanotechnol.* **2008**, *3*, 210−215.

(41) Li, X.; Cai, W.; An, J.; Kim, S.; Nah, J.; Yang, D.; Piner, R.; Velamakanni, A.; Jung, I.; Tutuc, E.; Banerjee, S. K.; Colombo, L.; Ruoff, R. S. Large-Area Synthesis of High-Quality and Uniform Graphene Films on Copper Foils. *Science* **2009**, *324*, 1312−1314.

(42) Cançado, L. G.; Jorio, A.; Ferreira, E. H. M.; Stavale, F.; Achete, C. A.; Capaz, R. B.; Moutinho, M. V. O.; Lombardo, A.; Kulmala, T. S.; Ferrari, A. C. Quantifying Defects in Graphene via Raman Spectroscopy at Different Excitation Energies. *Nano Lett.* **2011**, *11*, 3190−3196.

(43) Bokdam, M.; Khomyakov, P. A.; Brocks, G.; Kelly, P. J. Field Effect Doping of Graphene in Metal|dielectric|graphene Hetero-structures: A Model Based upon First-Principles Calculations. *Phys. Rev. B: Condens. Matter Mater. Phys.* **2013**, *87*, 075414.

(44) Hu, C. H.; Zheng, Y.; Zhang, Y.; Wu, S. Q.; Wen, Y. H.; Zhu, Z. Z. Electronic and Magnetic Properties of Silicon Adsorption on Graphene. *Solid State Commun.* **2011**, *151*, 1128−1130.

(45) Gillespie, P. N. O.; Martsinovich, N. Electronic Structure and Charge Transfer in the TiO2 Rutile (110)/Graphene Composite Using Hybrid DFT Calculations. *J. Phys. Chem. C* **2017**, *121*, 4158−4171.

(46) Du, A.; Ng, Y. H.; Bell, N. J.; Zhu, Z.; Amal, R.; Smith, S. C. Hybrid Graphene/Titania Nanocomposite: Interface Charge Transfer, Hole Doping, and Sensitization for Visible Light Response. *J. Phys. Chem. Lett.* **2011**, *2*, 894−899.

(47) Castro Neto, A. H.; Guinea, F. Impurity-Induced Spin-Orbit Coupling in Graphene. *Phys. Rev. Lett.* **2009**, *103*, 026804.

(48) Santos, E. J. G.; Ayuela, A.; Sánchez-Portal, D. Universal Magnetic Properties of Sp 3-Type Defects in Covalently Functionalized Graphene. *New J. Phys.* **2012**, *14*, 043022.

(49) Kochan, D.; Gmitra, M.; Fabian, J. Spin Relaxation Mechanism in Graphene: Resonant Scattering by Magnetic Impurities. *Phys. Rev. Lett.* **2014**, *112*, 116602.

(50) Wojtaszek, M.; Vera-Marun, I. J.; Maassen, T.; van Wees, B. J. Enhancement of Spin Relaxation Time in Hydrogenated Graphene Spin-Valve Devices. *Phys. Rev. B: Condens. Matter Mater. Phys.* **2013**, *87*, No. 081402(R).

(51) McCreary, K. M.; Swartz, A. G.; Han, W.; Fabian, J.; Kawakami, R. K. Magnetic Moment Formation in Graphene Detected by Scattering of Pure Spin Currents. *Phys. Rev. Lett.* **2012**, *109*, 186604.

(52) Balakrishnan, J.; Kok Wai Koon, G.; Jaiswal, M.; Castro Neto, a. H.; Özyilmaz, B. Colossal Enhancement of Spin−Orbit Coupling in Weakly Hydrogenated Graphene. *Nat. Phys.* **2013**, *9*, 284−287.

(53) Leutenantsmeyer, J. C.; Kaverzin, A. A.; Wojtaszek, M.; van Wees, B. J. Proximity Induced Room-Temperature Ferromagnetism in Graphene Probed with Spin Currents. *2D Mater.* **2016**, *4*, 014001.

67

Insights and implications of intricate surface charge transfer and sp³-defects in graphene/metal oxide interfaces

Daria Belotcerkovtceva[1], Renan P. Maciel[1], Elin Berggren[1], Ramu Maddu[2], Tapati Sarkar[2], Yaroslav O. Kvashnin[1], Danny Thonig[1,3], Andreas Lindblad[1], Olle Eriksson[1,3], M. Venkata Kamalakar[1*]

[1]*Department of Physics and Astronomy, Uppsala University, Box 516, SE-751 20 Uppsala, Sweden*
[2]*Department of Materials Science and Engineering, Uppsala University, Box 35, SE-751 03 Uppsala, Sweden*
[3]*School of Science and Technology, Örebro University, Fakultetsgatan 1, SE-70182 Örebro, Sweden*
*Email: venkata.mutta@physics.uu.se

1   Device Fabrication

Commercial CVD graphene (Graphenea Inc.) grown on Cu substrate and transferred over 4 inches Si/SiO₂ wafer was employed for device fabrication. Via photolithography and 50 W argon plasma etching process, graphene was first patterned into 55 μm long stripes of 5 μm width. Then, the remaining photoresist was removed with acetone at 70°C and rinsed with isopropanol (IPA). Electrical contacts with a layered structure of TiO_x(2 nm)/Co(60 nm)/Al(3 nm) and separated by a spacing of 10 μm were fabricated on graphene stripes by e-beam lithography patterning and metal lift-off. The lift-off was achieved in hot acetone, rinsed by IPA. The devices were imaged using an optical microscope, with the optical parameters adjusted to observe the contrast of graphene over SiO₂/Si. After performing electrical measurements on pristine devices, the Ti or Al (0.8 nm) metal was evaporated by e-beam evaporation with a deposition rate of 0.5 Å/s, which was subsequently oxidized in air conditions.

2   Sample characterization

2a. Electrical Measurements

Electrical transport measurements were performed in high-vacuum conditions ($\sim 10^{-7}$ mbar) with a room-temperature setup, using a Keithley current source and a nanovoltmeter. In addition, gate voltage was applied by a Keithley source meter. Using the equation $\sigma\,(n) = Ce\left|\dfrac{n}{n_{imp}}\right| + \sigma_{res}$, where $C = 5 \times 10^{15}$ V⁻¹s⁻¹, n is the carrier density, e is the electronic charge and σ_{res} is the residual conductivity, we estimated the charge impurity density[1] (Fig. S1a shows a representative fitting for a sample before and after the realization of AlO_x) with a variation Δn_{imp} ~5-20 × 10¹¹ cm⁻² for both oxides, which is up to an order higher than the sp³ defect density that we found using Raman spectroscopy. In addition, we also found low trap density ~10¹¹ cm⁻² (trapped carriers $n_{trap} = \Delta V_{DP}\, C_g/2e$ in the charge trapping effect[2], with a change in Dirac point ΔV_{DP} in hysteresis of Dirac curves, gate capacitance C_g, and electronic charge e) for all samples, compared to actual shift in the Dirac point due to oxide layers.
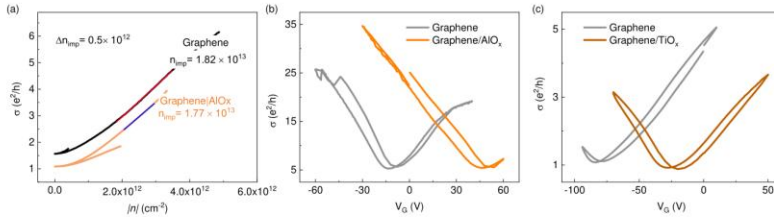
Figure S1. (a) Charge impurity density estimated by fitting the Dirac curves using $\sigma\,(n)$. Conductance change vs. gate voltage at 1 V/s gate sweep rate for graphene devices before and after oxide realization for (b) AlO_x and (c) TiO_x layers on graphene.

2b. Raman Spectroscopy

Raman spectroscopy was conducted with a Renishaw Reflex (Invia) Raman spectrometer for the single-layer CVD graphene (pristine graphene) and after Ti or Al deposition to see the evolution of the 2D and G peaks and the appearance of the D peak to calculate the defect concentration. To estimate the defect density via Raman spectroscopy, we used the empirical formula: $(n_D = \dfrac{2.4 * 10^{22}}{\lambda_L^4}\dfrac{I_D}{I_G}$ with λ_L the laser line wavelength) which is applicable in high-density regimes $(\dfrac{I_D}{I_G} \approx 60\%)$[3].

1

68

2c. Atomic Force Microscopy

Conventional AFM images of the graphene with deposited Ti and Al were obtained by Scanning Probe Microscope Bruker Dimension Icon with high resolution and low noise level for topography analysis using scan areas of 1 μm × 1 μm and 250 nm × 250 nm with corresponding height profiles and root mean square roughness. While imaging, we used PeakForce in the ScanAsyst imaging mode introduced by Bruker. The PeakForce method combines tapping mode as well as contact mode where direct force is controlled, and damaging lateral forces are avoided. The scan ScanAsyst algorithm optimizes the speed of the scan, z-position, and forces. In our samples, it was the optimum mode for high-resolution images of graphene with deposited ultra-thin metal oxides.

2d. X-ray Photoelectron Spectroscopy

X-ray photoelectron spectroscopy (XPS) was performed using a Physical Electronics Quantera II Scanning XPS Microprobe with a monochromatic Al Kα source (1486.7 eV). Overview spectra were collected with a beam diameter set to 200 μm and pass energy to 224 eV, resulting in an energy resolution of 1.3 eV. For single region spectra of O 1s, Al 2p, C 1s, and Ti 2p, a 100 μm beam diameter and 55 eV pass energy was used, resulting in an energy resolution of 0.7 eV. To avoid the possibility of defect contributions from the edges in the devices, we performed XPS measurements on a 0.7×0.7 cm^2 Si/SiO$_2$ substrate fully covered with CVD graphene and top metal-oxides. XPS spectra were analyzed by correcting the background with the Shirley method and fitting core-electron peaks with Voigt functions.

3 Computational details for aluminum oxide simulation

The ab-initio calculations were performed using the Vienna Ab-initio Simulation Package (VASP). For all simulations, we considered the projector augmented wave (PAW) approach and the generalized gradient approximation (GGA) using the Perdew-Burke-Ernzerhof (PBE) functional. With an energy cutoff of 520 eV, the plane-wave basis set for the AlO$_x$/graphene structure was chosen. The ionic forces were optimized with a Monkhorst-Pack mesh of k-points of $9 \times 9 \times 1$ subdivisions, and the convergence criterion was 0.001 eV/Å. The vacuum space in the z-periodic direction was approximately 35 Å for all investigated configurations, which is large enough to avoid interactions between periodic images. The Van der Waals (vdW) interaction was considered for the combined graphene-oxide structures using the DFT-D3 approach with Becke-Johnson damping[4]. To analyze the electronic properties of the studied systems, we combined the vasp post-processing tools[5,6].
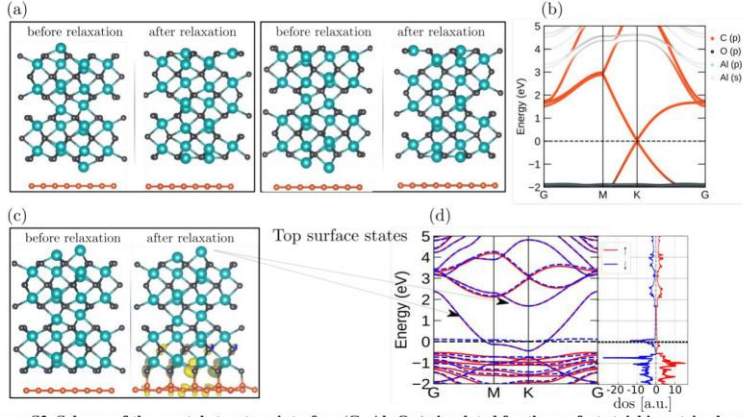
3a. Aluminum oxide interface construction

In this work, we considered a $2 \times 2 \times 1$ hexagonal graphene supercell with $a_1 = a_2 \sim 4.92$ Å and a $1 \times 1 \times 1$ aluminum oxide Al$_2$O$_3$ unit cell with lattice vectors $b_1 = b_2 \sim 4.76$ Å. To study the interface between graphene and aluminum oxide (α-Al$_2$O$_3$), we compensated for the existing lattice mismatch by applying a strain of 3.25% in the Al$_2$O$_3$ unit cell. Within this choice, we ensure that all graphene electrical-related properties are primarily preserved. In addition, an approximately 13 Å thick slab of Al$_2$O$_3$ (correspondent to the Al$_{12}$O$_{18}$ stoichiometry) is attached to the top of the graphene supercell in order to mimic the experimentally synthesized samples. For the simulation purpose, an initial spacing of 2 Å between these two crystals was considered.

The Al$_{12}$O$_{18}$ slab can have (two) Al or (three) oxygen atoms near graphene. Since one can find similar results even for different geometries, we consider the amount of dangling bonds at the top and at the bottom surface of the slab as a criterion to select the number of various interfaces to be studied. In particular, we chose three interfaces that are illustrated in Fig. S2a and S2c. Additionally, we investigated the structural and electrical properties of slightly off-stoichiometric oxides (Fig. S3) when one Al or O atom next to the graphene layer is removed.

3b. Perfect stoichiometric AlO$_x$/graphene interface

Fig. S2 shows the structure before and after the atomic relaxation, as well as the band structures of all considered graphene-Al$_{12}$O$_{18}$ systems, and summarizes the properties found for the combined structure graphene/Al$_{12}$O$_{18}$. In Fig. S2a, we observe that when aluminum is in proximity to the graphene layer, a flat bond between Al and O is formed, and the equilibrium distance between the two crystals exhibits an increase of 0.9 Å after force minimization. This suggests that this Al$_{12}$O$_{18}$ geometry has a weak interaction with graphene. Consequently, no significant change at the Dirac cone of the graphene structure is observed (see Fig. S2b). However, when oxygen is in proximity to the graphene layer, two (out of three) oxygen atoms form sp^3 bonds with the carbon atoms (Fig. S2c). The unbonded oxygen holds unpaired electrons. For this reason, this oxygen shows a total magnetic moment of 0.32 μ$_B$ while the whole system has a magnetization of 0.61 μ$_B$ per unit cell.

2

Figure S2. Scheme of the crystal structure interface (C$_8$-Al$_{12}$O$_{18}$) simulated for the perfect stoichiometric aluminum oxide. The colors green, gray, and orange represent Al, O, and C atoms. (a) Graphene/aluminum oxide interface before and after force minimization when aluminum is in proximity to the graphene layer. (b) The band structure shows no shifting of the Dirac cone when aluminum is in proximity to the graphene layer. (c) Force minimization when oxygen is in proximity to the graphene layer shows a formation of an sp^3 bond due to a strong hybridization between two oxygen and carbon atoms. The yellow crowds around O atoms represent the projected magnetic moment densities of the crystal. (d) The spin-polarized band structure and its corresponding total density of states (DOS) show the splitting of the different spins around the Fermi level. (The surface states' contributions from Al atoms are highlighted with arrows.)

3c. Small concentration of sp^3 bond in perfect stoichiometric oxide

To better understand the influence of the sp^3 bond in the electronic structure of pristine graphene, we created an interface with only one sp^3 bond per unit cell (rather than two, as shown in Fig. S2c). This interface is constructed by restricting the optimized system represented in Fig. S2c to just forming one sp^3 bond while preventing it from minimizing forces again. The resulting electronic band structure (see Fig. 5 in the main paper) has a significant gap widening of the Dirac cone. Furthermore, the magnetization of the entire system is lowered from 0.65 μ_B to 0.5 μ_B per unit cell.

3d. Slightly off-stoichiometric AlO$_x$/graphene interface

For the slightly off-stoichiometric system, we focused on the geometry where oxygen is in proximity to the graphene layer. The reason for such analysis is that the charge transfer is expected mainly from the carbon to the oxygen atoms. For the graphene-Al$_{11}$O$_{18}$ structure, we observe after force minimization that two sp^3 bonds are formed between the oxygen and carbon atoms (see Fig. S3a). However, in the case of graphene-Al$_{12}$O$_{17}$, the crystals exhibit an increase of 0.9 Å of the initial distance, and no deformation in the graphene layer is observed. The total magnetization corresponding to the graphene-Al$_{11}$O$_{18}$ structure is 1.0 μ_B, while for Al$_{12}$O$_{17}$ is 0.44 μ_B. A gap opening at the Dirac cone is observed for both systems (see Figs. S3b and S3d). Furthermore, in both the band structure and spin-polarized DOS, the magnetism around the oxygen atoms near to graphene layer causes the states around the Fermi level to have different spin polarities (see Fig. S3d). Despite this, we found that Al$_{12}$O$_{17}$ induces p-type doping in the graphene structure, whereas it opens a gap of approximately 1 eV.

3

70
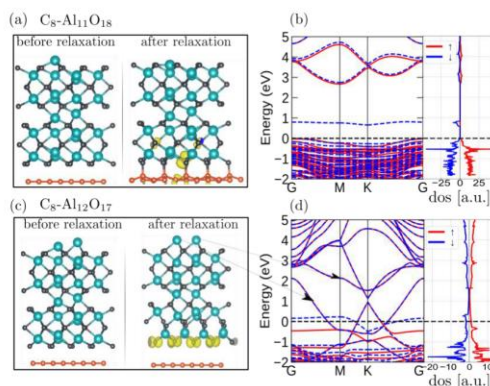
Figure S3. Schematic representation of the slightly off-stoichiometric oxide. The (a) $Al_{11}O_{18}$ and (c) $Al_{12}O_{17}$ slab before and after force minimization. The optimized structure also shows the projected magnetic moment densities of the crystal, primarily around oxygen atoms. The resolved band structure and the spin projected density of states of the (b) $Al_{11}O_{18}$ and (d) $Al_{12}O_{17}$, where red (blue) represents spin up (down). The arrows highlight the top surface states' contributions to the electronic band structure for the latter. (The representative colors of each atom, the yellow crowds around the oxygen atoms, and the arrows have the same meanings as in Fig. S2).

References

(1)   Chen, J. H.; Jang, C.; Adam, S.; Fuhrer, M. S.; Williams, E. D.; Ishigami, M. Charged-Impurity Scattering in Graphene. *Nat. Phys.* **2008**, *4* (5), 377–381. https://doi.org/10.1038/nphys935.

(2)   Kalon, G.; Jun Shin, Y.; Giang Truong, V.; Kalitsov, A.; Yang, H. The Role of Charge Traps in Inducing Hysteresis: Capacitance-Voltage Measurements on Top Gated Bilayer Graphene. *Appl. Phys. Lett.* **2011**, *99* (8), 1–4. https://doi.org/10.1063/1.3626854.

(3)   Cançado, L. G.; Takai, K.; Enoki, T.; Endo, M.; Kim, Y. A.; Mizusaki, H.; Jorio, A.; Coelho, L. N.; Magalhães-Paniago, R.; Pimenta, M. A. General Equation for the Determination of the Crystallite Size La of Nanographite by Raman Spectroscopy. *Appl. Phys. Lett.* **2006**, *88* (16), 1–4. https://doi.org/10.1063/1.2196057.

(4)   GRIMME, STEFAN, EHRLICH, STEPHAN, GOERIGK, L. Effect of the Damping Function in Dispersion Corrected Density Functional Theory STEFAN. *J. Comput. Chem.* **2011**, *32* (Sfb 858), 1456. https://doi.org/10.1002/jcc.

(5)   M Ganose, A.; J Jackson, A.; O Scanlon, D. Sumo: Command-Line Tools for Plotting and Analysis of Periodic Ab Initio Calculations. *J. Open Source Softw.* **2018**, *3* (28), 717. https://doi.org/10.21105/joss.00717.

(6)   Herath, U.; Tavadze, P.; He, X.; Bousquet, E.; Singh, S.; Muñoz, F.; Romero, A. H. PyProcar: A Python Library for Electronic Structure Pre/Post-Processing. *Comput. Phys. Commun.* **2020**, *251*. https://doi.org/10.1016/j.cpc.2019.107080.

4

71

Paper II

High current limits in chemical vapor deposited graphene spintronic devices

Daria Belotcerkovtceva[1,§], J. Panda[1,§], M. Ramu[2], Tapati Sarkar[2], Ulrich Noumbe[1], and M. Venkata Kamalakar[1] (✉)

[1] Department of Physics and Astronomy, Uppsala University, Box 516, Uppsala SE-751 20, Sweden
[2] Department of Materials Science and Engineering, Uppsala University, Box 35, Uppsala SE-751 03, Sweden
[§] Daria Belotcerkovtceva and J. Panda contributed equally to this work.

ABSTRACT

Understanding the stability and current-carrying capacity of graphene spintronic devices is key to their applications in graphene channel-based spin current sensors, spin-torque oscillators, and potential spin-integrated circuits. However, despite the demonstrated high current densities in exfoliated graphene, the current-carrying capacity of large-scale chemical vapor deposited (CVD) graphene is not established. Particularly, the grainy nature of chemical vapor deposited graphene and the presence of a tunnel barrier in CVD graphene spin devices pose questions about the stability of high current electrical spin injection. In this work, we observe that despite structural imperfections, CVD graphene sustains remarkably highest currents of 5.2×10^8 A/cm^2, up to two orders higher than previously reported values in multilayer CVD graphene, with the capacity primarily dependent upon the sheet resistance of graphene. Furthermore, we notice a reversible regime, up to which CVD graphene can be operated without degradation with operating currents as high as 10^8 A/cm^2, significantly high and durable over long time of operation with spin valve signals observed up to such high current densities. At the same time, the tunnel barrier resistance can be modified by the application of high currents. Our results demonstrate the robustness of large-scale CVD graphene and bring fresh insights for engineering and harnessing pure spin currents for innovative device applications.

KEYWORDS

chemical vapor deposited (CVD) graphene, high current density, graphene spintronics, spin integrated circuits, graphene spin valve

1 Introduction

Over the last decade, the field of two-dimensional (2D) nanoelectronics and spintronics [1] has witnessed enormous advancements in using graphene for new applications that show promise for memory-logic integrated circuits, including neuromorphic components. In particular, attaining high performance in wafer-scale commercial systems is necessary for graphene spintronic sensors and circuits to take off. Yet, challenges remain when it comes to the feasibility of applications such as spin torque effects [2] and spin torque oscillators [3] that require high current carrying capacity and stability. Even nanodevices using copper have a current carrying limitation of ~ 10^8 A/cm^2. Today, the advancement of the chemical vapor deposition method has enabled the production of practical and industry-compatible large-area graphene [3, 4]; with commercial graphene being readily available, it presents real prospects in high-quality charge and spin transport devices [5]. For example, competitive spin transport achieved in monolayer chemical vapor deposited (CVD) graphene [6, 7], including on flexible substrates [8], and recent reports of ultimate spin current capabilities using CVD graphene [9], even under ambient conditions, show massive scope for the growth of graphene spintronic applications. However, when it comes to current carrying capacity, the grainy structure of CVD graphene and tunnel barriers utilized in

spintronic devices pose a question on the limitation of the maximum current applicable in such devices. Past studies, mainly performed on mechanically exfoliated few-layer graphene nanoribbons obtained from Kish graphite, have shown a breakdown current density of ~ 10^8 A/cm^2 [10, 11], including results obtained in bilayer graphene [12]. Compared to these reports on exfoliated systems, current stress investigation on multilayer CVD graphene revealed one order less maximum breakdown current density ~ 4×10^7 A/cm^2 [13]. Recently, a current density of 1.18×10^8 A/cm^2 was reported in 300 nm channels of CVD graphene contacted by metal electrodes [14]. Since the size of the graphene channel is too small here to contain grain boundaries or ripples, such a value matches well with measurements on single crystalline exfoliated graphene flakes. However, considering this size is less than the typical micron range crystal size in CVD graphene, the current carrying capacity of large-scale CVD graphene is still unclear. Especially, earlier results in polycrystalline samples showed one order lower current density [13]. While CVD graphene presents significant scope for scalability and practical applications, it exhibits intrinsic defects, grain boundaries, wrinkles, and transfer/fabrication-accrued impurities, that are known to limit the electrical performance of these devices. CVD graphene grown over Cu substrate is reported to feature grain sizes of a few microns [15]. Commercial graphene

displays typical grain boundaries/ripples in the size range of 2–5 μm, confirmed through multiple techniques [16] (displayed later in Fig. 1). The nanoscale defects of grain boundaries and wrinkles increase electrical resistance, and consequently can act as hot spots where localized resistive heating and breakdown can occur preferentially [17]. Localized Joule heating in grain boundaries tends to constrict device shape leading to further defect formations. For devices longer than 5 μm, local high-temperature spots can arise due to grain boundaries and wrinkles, subsequently affecting current limits of the spin devices. On a smaller scale, heated grain boundaries cause heat flow leading to faster device failure. Therefore, understanding the stability and maximum current carrying capacity of CVD graphene spin channels and contacts under the influence of high current is crucial for developing high spin current generation capabilities and spin current interconnect applications for spin integrated circuits.

In this work, we demonstrate a very high current carrying capacity in monolayer CVD graphene with a breakdown density of sub-10^9 A/cm^2. Through elaborate 2-probe and 4-probe measurements, we uncover a distinct channel behavior upon high current stress and range up to which CVD graphene channel can be electrically operated and how breakdown current density varies with graphene sheet resistance. We also explore spin transport in such channels with high electrical currents of 1 mA (~ 10^8 A/cm^2), stability of several hours of long-term current passage, and the response of contacts to such high currents.

2 Results and discussion

To investigate the current carrying capacity of monolayer CVD graphene-based spin devices, we fabricated graphene spin devices using commercial CVD graphene on Cu (Graphenea, Spain), with multiple TiO$_x$|Co electrodes for spin injection and detection. Raman spectrum indicating the monolayer nature of CVD graphene is shown in Fig. S1 in the Electronic Supplementary Marterial (ESM). We also performed atomic force microscopy (AFM) of our CVD graphene on Si/SiO$_2$ substrate as well as of the patterned device structures, which reveals grains and wrinkles in the μm range, as shown in Figs. 1(a) and 1(b). The detailed device fabrication procedure is explained in the Methods section. Figure 1(c) shows a schematic of a patterned CVD graphene with ferromagnetic tunnel contacts. To determine the electrical

properties of graphene and contact interfaces, we first performed low current electrical transport measurements in several configurations. Four probe gate dependence measurements yielded field-effect electron mobility ~ 1,750 cm^2/(V·s) (Fig. 1(d)), which demonstrates that our devices show reasonable mobility needed to establish good quality spin transport. A high n-type doping was intrinsic to the as-prepared devices and can be primarily attributed to the interaction with the substrate and dangling bonds that are expected in the top 280 nm SiO$_2$ layer of the Si/SiO$_2$ substrate, which can promote charge transfer across the graphene-SiO$_2$ interface. Other causes that contribute to the n-type doping are fabrication process steps that involve solvents, reactive ion etching for pattering graphene, and electrode realization [9, 18]. Low current characterization of channel, contacts, and spin valve signal are shown in Fig. S2 in the ESM. Following these initial measurements, we performed high-current stressing experiments, first with two terminals (2T), a standard method employed in past studies. As shown in Fig. 1(e) (I–V characteristics), the current (I) increases with an applied bias voltage (V), and at a specific high current, the graphene breakdown occurs, resulting in an abrupt drop in the current. The non-linear 2T I–V curve at low voltages confirms tunneling behavior across the oxide tunnel barrier interfaces with graphene (Fig. 1(e)). However, a continuous reduction in slope at higher currents can be attributed to a heating-related cumulative increase in the graphene channel resistance. To further determine the actual response of graphene channels, we performed four-terminal (4T) I–V measurements (Fig. 1(f)), which revealed linear I–V characteristics up to a high current of 2 mA (~ 10^8 A/cm^2) with graphene sheet resistance ~ 0.5–2 kΩ/□. Interestingly, a sharp onset of non-linear saturation behavior was also observed. While this can be attributed to the increase in resistance due to Joule heating and cumulative effects, the overall behavior depends upon the competition between the rate of heating in graphene and the rate of heat dissipation in the SiO$_2$/Si substrate.

As seen in the repeated cyclic measurements performed in the four-terminals scheme (4T) (Fig. 1(f)), the channel resistance undergoes changes beyond a specific current density. Since these devices are broken after each high current measurement, we presented our overall observations on several devices showing different sheet resistances. The current saturation regime divides the I–V curve into reversible and non-reversible, where self-
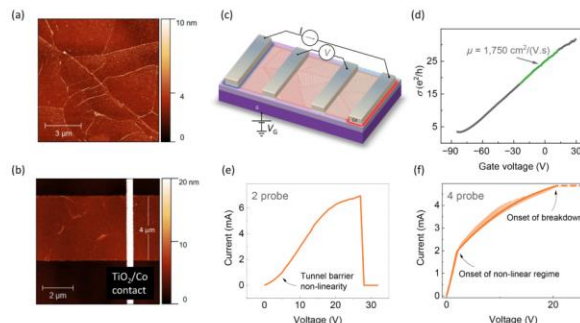

Figure 1 AFM image of (a) graphene over 10 μm × 10 μm area with distinguished wrinkles and ripples, and (b) graphene channel near contact region of a device with corresponding actual width. (c) Schematic of a graphene device in four-probe measurement technique. (d) Gate dependence with extracted mobility at low bias currents. (e) 2-terminal I–V curve of the CVD graphene undergoing electrical breakdown. (f) 4-terminal I–V characteristics with constantly increasing sweep range. The onset of breakdown is typical of the current source response as the voltage measured by the voltmeter abruptly reaches the compliance voltage limit of the current source.

heating can be observed at a high current (Fig. 2(a)). To examine the transition between the two regimes, *I–V* curves were recorded within cycles with the varying maximum current in steps (I_{step} = 0.2 mA, between 0–3 mA). Despite the high current carrying capacity, the CVD graphene channel degradation due to cumulative Joule heating can lead to an irreversible regime. The transition between reversible and irreversible regimes is observed to occur at a specific value of current ($I_{max\,rev}$) in each cycle, and the sheet resistance of the graphene channel changes after each cycle beyond the reversible regime. The behavior of $I_{max\,rev}$ for each cycle is found to characteristically vary with the sheet resistance, as displayed in the inset of Fig. 2(a), as a higher resistance requires a lower maximum current to modify the graphene sheet. However, keeping the operation of the device in the current range less than $I_{max\,rev}$ (~ 10^8 A/cm^2) allows graphene not to overheat and endure stable sheet resistance, as shown in Fig. 2(b). This implies that graphene devices on Si/SiO$_2$ can be operated with heat dissipation managed by the substrate Si/SiO$_2$ efficiently within the $I_{max\,rev}$ limit. Such information is particularly crucial because, while high current carrying capacity is known in graphene, the degradation has never been explicitly understood. The present study involving 4T measurement allows us to enlighten this issue for the first time. Furthermore, this allows us to isolate the role of contacts and only unveil the impact of high current stressing on graphene channels.

To fully determine the current-carrying capacity of the CVD graphene spin devices, including the tunnel contacts, we have measured the *I–V* characteristics of different graphene devices with varying sheet resistances extending up to 20 kΩ and above. A typical high field *I–V* characteristic is shown in Fig. 1(e) with increasing bias voltage until the graphene breakdown occurs at higher currents of several mA. Figure 2(c) shows the current density measured as a function of the CVD graphene sheet resistance for breakdown and reversible regimes for low sheet resistance devices (< 3 kΩ). The breakdown current density (J_b) values for these spin devices were in the range of 2–5.2 × 10^8 A/cm^2. The values of J_b observed in our monolayer CVD graphene spin devices are comparable to the breakdown current densities seen in the previously reported bilayer/multilayer graphene and

graphene nanoribbons [11, 13, 19]. Also, as shown in Fig. 2(c), the reversible current density (at the onset of saturation) of these devices was found to be ~ 10^8 A/cm^2, which suggests that our spin devices can be operated at high currents, beyond the typical current densities needed for spin-transfer torque applications. For most of our devices, the sheet resistance was found to have a typical value < 8 kΩ, with some devices closer to 20 kΩ and higher. To uncover the qualitative behavior of the breakdown current density of the CVD graphene with sheet resistance, we measured J_b as a function of sheet resistance of several devices, including devices that displayed high sheet resistance. As shown in Fig. 2(d), CVD graphene channels with higher sheet resistance exhibit lower J_b values and are more likely to undergo breakdown for the same current density. Defects, wrinkles, grain boundaries, and impurities increase the effective resistivity and result in high resistive sheets. The behavior in Fig. 2(d) can be understood from the fact that considering the same substrate heat dissipation and similar breakdown temperature for all CVD graphene sheets, higher resistance would require a lower current (assuming breakdown power density $J_b^2 \times R_\square \approx$ const for all our samples leads to $J_b \propto 1/\sqrt{R_\square}$) for channel breakage. Note that in these spin devices, the value of J_b also includes the tunnel barrier resistive contact region that could degrade at high current densities. Despite this, in the inset of Fig. 2(d), we show the fit of $J_b \propto R_\square^{-a}$, and obtain $\alpha \approx 0.32$, which is reasonably close to the expected value of $\alpha = 0.5$. These results suggest that CVD graphene with sheet resistance lower than kΩ can have a high breakdown current density of ~ 10^9 A/cm^2, which could be achieved by highly doped graphene by surface charge transfer doping without degrading the electrical quality of graphene [18] and using high thermal conductivity substrates for greater heat dissipation.

As displayed in Fig. 3(a), the CVD graphene channels show nonlocal (NL) spin transport at high currents. In the NL measurement scheme shown in the inset of Fig. 3(b), spin-polarized currents are electrically injected into the graphene channel through the current circuit (*I*), and the resulting diffusion of pure spin current at a distance of *L* is detected by the voltage circuit (V_{NL}). Such isolation of the current and voltage circuits
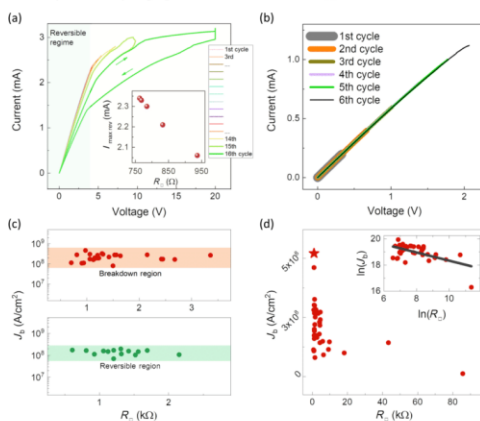
Figure 2 (a) Measured 4T *I–V* curve cycles with linear (reversible) and non-linear (non-reversible) regimes at high voltage (*V* > 4.5 V). Inset: $I_{max\,rev}$ versus sheet resistance of graphene for each cycle beyond $I_{max\,rev}$. (b) 4T *I–V* curve cycles of the device within the reversible regime. (c) Measured maximum current density versus sheet resistance in different devices. (d) Breakdown current density as a function of sheet resistance of the CVD graphene (the star symbol indicates the maximum breakdown of current density obtained in our devices). Inset: current density versus sheet resistance fitted to $J_b \propto R_\square^{-a}$.
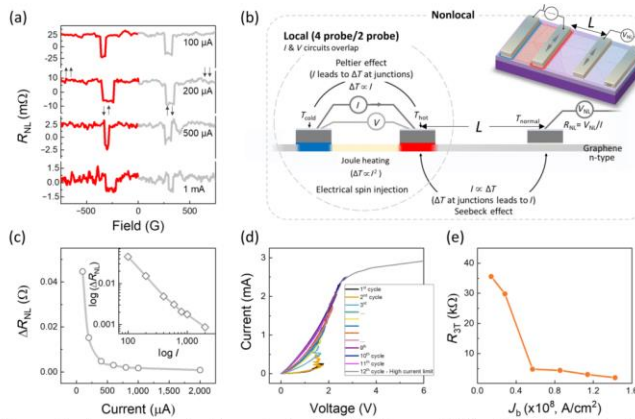
Figure 3 (a) Spin transport signal measured in the spin-valve geometry showing switching between parallel (↑↑ or ↓↓) to antiparallel (↓↑ or ↑↓) configurations of the injector and detector electrodes at different applied currents. (b) Local and nonlocal measurement configurations in graphene spin devices, with depiction of thermoelectric effects such as Joule heating, Peltier effect, and Seebeck effect in a device. (c) Nonlocal resistance as a function of applied current from spin-valve transport measurements. The inset shows the logarithmic dependence of the plot. (d) Consecutive multiple 3T *I*–*V* cycles with increasing maximum applied current and electrical breakdown in the 12th cycle. (e) Contact resistance (measured at 100 mV) versus maximum applied current density in a measurement cycle.

allows for reliable measurement of pure spin accumulation, eliminating spurious magneto-resistive contributions associated with direct charge currents. Further details of the spin transport measurements can be found in the ESM. As shown in Fig. 3(a), clear spin valve signals were observed at very high spin injection currents of 100 μA–1 mA, implying that even at current densities $\sim 10^8$ A/cm^2, graphene channels endure and show spin diffusion. Considering a large injector-detector separation of $L = 10$ μm, the observed spin signals are reasonable for standard spin polarization of Co|TiO$_2$ injectors into graphene and of similar order as previously reported on Si/SiO$_2$ devices [6, 20, 21]. Interestingly, the nonlocal resistance strongly depends on the applied current (Fig. 3(c)), with the spin signal amplitudes heavily quenched at very high currents of 1 mA ($\sim 10^8$ A/cm^2). In graphene devices carrying high currents (both 2-probe or 4-probe measurements, shown in Figs. 1 and 2, respectively), while Joule heating occurs in the current carrying graphene channel, Peltier heating/cooling can take place at junctions [17, 22] (illustrated in Fig. 3(b)), which can be revealed by thermography techniques [23, 24]. On the other hand, in the nonlocal measurement geometry employed in the spin transport measurement, the spin injection circuit only involves spin current, and the corresponding graphene strip undergoes Joule heating. In addition, in this part, heating/cooling is expected to occur at the interface between graphene and TiO$_2$|Co due to the Peltier effect [17, 22]. Since the width of the contacts in our devices (~ 100 nm) is much smaller than the characteristic contact transfer length for the interface materials involved (~ 1 μm), we can rule out the contribution of the current crowding effect [17]. In the pure spin diffusion channel (between injector and detector), with no direct electrical bias across the injector and detector, in principle no Joule heating is expected, although a temperature difference between the contacts could lead to some Seebeck voltage [25]. Because graphene exhibits slow electron-lattice cooling rates, the thermoelectric effects are likely to contribute to the baseline in V_{NL} [26]. In addition, due to the negligible temperature gradient across the graphene-tunnel barrier-ferromagnet injector interface (as electric current passes through

the whole stack at the contacts), any thermal spin voltage is expected to be negligible compared to actual electrically-created nonlocal spin voltage [27]. Therefore, the behavior of spin valve amplitude at high currents can be ascribed to hot electrons due to a high voltage drop (at high current) across the injector interface. Such high voltage bias can result in enhanced ferromagnet-tunnel barrier interface spin excitations, leading to higher electron–magnon spin-flip scattering, which is expected to quench spin polarization [28–30]. In addition, change in barrier profile, a higher channel resistance due to cumulative heating, and possible reduced contact resistance at higher bias/high temperature are further expected to contribute to the observation of lower spin valve signals at higher current [31]. The tunnel barrier response to high currents is not known here. In particular, considering the oxide nature of the barrier, contact resistance modulation is expected. To understand that, three terminals (3T) cyclic measurements up to high currents were performed. As shown in Fig. 3(d), the resistance of the barrier was seen to decrease at high injection currents. While some contacts showed high current sustainability and typical tunneling *I*–*V* characteristic curves till high currents (as shown in Fig. S3(a) in the ESM), high resistive contacts (due to high voltage drop across interfaces) showed a decrease in resistance upon high current stressing. Such a decrease at relatively high voltage could be ascribed to the possible formation of conducting nanofilaments in the Co|TiO$_2$|graphene junction due to naturally oxidized ultra-thin oxide, and consequent high current density and contact enhanced spin relaxation in graphene, which could contribute to the enhanced quenching of spin signal in Fig. 3(c). In Fig. 3(e), we show low bias (100 mV) contact|graphene interface resistance as a function of the high current. Interestingly, our experiments reveal here for the first time that the channel and contact resistances exhibit very different responses to high currents. While the channel resistance remains unchanged in a reversible/stable regime up to high current densities, the contact resistance changes due to the possible formation of filaments in the 10^8 A/cm^2 current density regime. In our devices, the tunnel barrier (Gr/TiO$_x$/Co junction) is

expected to exhibit non-stoichiometric ultra-thin metal oxide. High electric field/high voltage bias across the ultrathin barrier (~ nm) can facilitate Ti nanofilament formation or oxygen ion migration across the junction, which can explicate the 3T graphene|ferromagnetic tunnel contact resistance reduction when subjected to high current density.

Finally, to test the endurance of the contacts and channels in our spin devices, we have performed time-dependent measurements at current densities ~ 10^8 A/cm^2 in graphene spin devices. Figure 4(a) shows time-dependent 3T (contact resistance) and 4T (graphene resistance) measurements. While the resistance of the contacts changes at high currents, the channel resistance stays fairly stable for a long time at high currents. Note that, in comparison to the 3T cyclic measurements on contacts in Fig. 3(d), where high current reduces the contact resistance, due to the possible formation of conducting filaments across the interface, measurement at constant high current over longer periods could lead to breakage and reformation/increase in density of the nanofilaments under high current stress. This could explain the initial increase in resistance in Fig. 4(a) till the stabilization in resistance is attained by the reformation of nanofilaments with enhanced current carrying capacity. Since the graphene channel survives till high currents and electromigration [32], considering interface thermal and conductivity mismatch and lower current carrying capacity of metals, the high current density is expected to affect the metal contact pads before the breakage of graphene. Figure 4(b) shows the optical images of the CVD graphene devices before and after the breakdown limit. The images reveal faster degradation of thick metal contacts than CVD graphene, despite the single-layer nature of graphene here. These experiments suggest that ultrathin tunnel barriers with higher resistance undergo modification in resistance. The tunable interface resistance with thicker tunnel barriers could have potential in synaptic spin-valve memristors. On the other hand, a possible way

to avoid oxygen-migrated filament formation in conventional oxides could be to employ stable amorphous carbon interfacial layers [33], hexagonal boron nitride [34–36], or fluorographene [37] due to their structural integrity. Furthermore, with the advent of atomically thin 2D magnets and their spinterfaces [38], the high-current electromigration issues with conventional ferromagnetic thin films could possibly be mitigated.

3 Conclusions

In summary, graphene spintronic devices were investigated to determine the ultimate current carrying capacity through monolayer CVD graphene and ferromagnetic tunnel contacts. We observed the highest current carrying capacity in monolayer CVD graphene, with a breakdown current density of 5.2×10^8 A/cm^2, an order higher than the previously reported values in multilayer CVD graphene interconnects. By systematic four-terminal and three-terminal measurements, for the first time, we uncovered a reversible regime ~ 10^8 A/cm^2 up to which the graphene on Si/SiO$_2$ substrate remains stable and exhibits long-term durability. In addition, with high electrical currents up to ~ 10^8 A/cm^2, we observed spin valve signal and tunnel barrier resistance modifications by possible conductive nanofilament formation at high currents. Our work offers insights on high current limits in graphene spintronics devices, a reversible regime up to which devices can be operated without degradation, possibilities for implementing barrier resistance modulation, and further engineering opportunities for efficient graphene spintronic applications.

## 4 Methods

4.1 Device fabrication

Graphene spin devices were fabricated using commercially obtained CVD graphene on Cu (Graphenea, Spain) transferred over a 4-inch Si wafer. The CVD graphene with ~ 4–5 μm width and ~ 60 μm long stripes was patterned using optical lithography followed by oxygen plasma etching with 50 W power. The remaining photoresist was then removed using hot acetone at 70 °C for 10 min, followed by isopropanol rinsing for 5 min. Next, ferromagnetic tunnel contacts with different widths were patterned on graphene stripes using electron beam lithography and metal lift-off. An optimized layer of 0.8 nm evaporated titanium metal for these electrodes was first oxidized to form a tunnel barrier layer of TiO$_x$. Following this, e-beam-assisted metal evaporation was performed to deposit successive layers of 60 nm Co and 5 nm Al. Finally, lift-off was achieved in hot acetone and rinsed by isopropyl alcohol (IPA). The obtained devices featured contacts with widths of 150–350 nm and an active contact area with graphene of ~ 1 μm^2. The devices were imaged using an optical microscope, with the optical parameters adjusted to observe the contrast of graphene over SiO$_2$/Si.

4.2 Raman spectroscopy

The single-layer nature of CVD graphene was confirmed by Raman spectroscopy. Spectra were obtained in the range 1,000–3,200 cm^{-1} under 532 nm laser excitation.

4.3 Spin transport and electrical measurements

Spin transport measurements in spin-valve and Hanle configurations were performed using Keithley current source and nano-voltmeter in high vacuum condition with a room temperature electromagnet set up. The magnetic field sweep was carried out in the range −1,000 to 1,000 G. The electrical three-

(a)

(b)
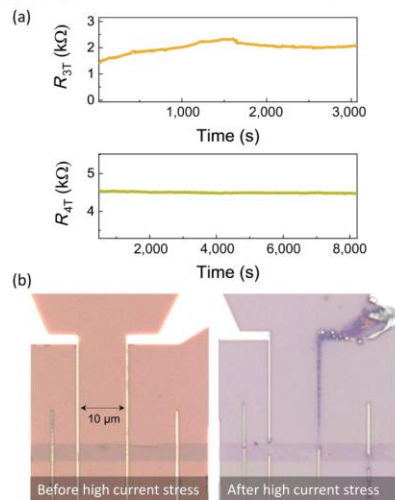
Figure 4 (a) Three-probe (contact) and four-probe (graphene channel) resistances as a function of time measured at high bias currents of 2 and 1 mA, respectively. (b) Optical images of the CVD graphene on SiO$_2$/Si substrate with Co/TiO$_2$ tunnel contact before and after the electrical breakdown.

terminals and four-terminals measurements were performed using a Keithley current source (with currents 100, 200, 500, and 1,000 μA for spin transport measurements) and a nanovoltmeter. Cyclic four probe current-voltage measurements were carried our with a Keithley sourcemeter.

References

[1] Avsar, A.; Ochoa, H.; Guinea, F.; Özyilmaz, B.; van Wees, B. J.; Vera-Marun, I. J. Colloquium: Spintronics in graphene and other two-dimensional materials. *Rev. Mod. Phys.* **2020**, *92*, 021003.

[2] Wang, P. C.; Filippi, R. G. Electromigration threshold in copper interconnects. *Appl. Phys. Lett.* **2001**, *78*, 3598–3600.

[3] Muñoz, R.; Gómez-Aleixandre, C. Review of CVD synthesis of graphene. *Chem. Vap. Depos.* **2013**, *19*, 297–322.

[4] Kim, K. S.; Zhao, Y.; Jang, H.; Lee, S. Y.; Kim, J. M.; Kim, K. S.; Ahn, J. H.; Kim, P.; Choi, J. Y.; Hong, B. H. Large-scale pattern growth of graphene films for stretchable transparent electrodes. *Nature* **2009**, *457*, 706–710.

[5] Mishra, H.; Panda, J.; Maddu, R.; Sarkar, T.; Dayen, J. F.; Belotcerkovtseva, D.; Kamalakar, M. V. Experimental advances in charge and spin transport in chemical vapor deposited graphene. *J. Phys. Mater.* **2021**, *4*, 042007.

[6] Kamalakar, M. V.; Groenveld, C.; Dankert, A.; Dash, S. P. Long distance spin communication in chemical vapour deposited graphene. *Nat. Commun.* **2015**, *6*, 6766.

[7] Gebeyehu, Z. M.; Parui, S.; Sierra, J. F.; Timmermans, M.; Esplandiu, M. J.; Brems, S.; Huyghebaert, C.; Garello, K.; Costache, M. V.; Valenzuela, S. O. Spin communication over 30 μm long channels of chemical vapor deposited graphene on SiO$_2$. *2D Mater.* **2019**, *6*, 034003.

[8] Serrano, I. G.; Panda, J.; Denoel, F.; Vallin, Ö.; Phuyal, D.; Karis, O.; Kamalakar, M. V. Two-dimensional flexible high diffusive spin circuits. *Nano Lett.* **2019**, *19*, 666–673.

[9] Panda, J.; Ramu, M.; Karis, O.; Sarkar, T.; Kamalakar, M. V. Ultimate spin currents in commercial chemical vapor deposited graphene. *ACS Nano* **2020**, *14*, 12771–12780.

[10] Moser, J.; Barreiro, A.; Bachtold, A. Current-induced cleaning of graphene. *Appl. Phys. Lett.* **2007**, *91*, 163513.

[11] Murali, R.; Yang, Y. X.; Brenner, K.; Beck, T.; Meindl, J. D. Breakdown current density of graphene nanoribbons. *Appl. Phys. Lett.* **2009**, *94*, 243114.

[12] Novoselov, K. S.; McCann, E.; Morozov, S. V.; Fal'ko, V. I.; Katsnelson, M. I.; Zeitler, U.; Jiang, D.; Schedin, F.; Geim, A. K. Unconventional quantum hall effect and Berry's phase of 2π in bilayer graphene. *Nat. Phys.* **2006**, *2*, 177–180.

[13] Lee, K. J.; Chandrakasan, A. P.; Kong, J. Breakdown current density of CVD-grown multilayer graphene interconnects. *IEEE Electron Device Lett.* **2011**, *32*, 557–559.

[14] Debroy, S.; Sivasubramani, S.; Vaidya, G.; Acharyya, S. G.; Acharyya, A. Temperature and size effect on the electrical properties of monolayer graphene based interconnects for next generation MQCA based nanoelectronics. *Sci. Rep.* **2020**, *10*, 6240.

[15] Kim, K.; Lee, Z.; Regan, W.; Kisielowski, C.; Crommie, M. F.; Zettl, A. Grain boundary mapping in polycrystalline graphene. *ACS Nano* **2011**, *5*, 2142–2146.

[16] Fan, X.; Wagner, S.; Schädlich, P.; Speck, F.; Kataria, S.; Haraldsson, T.; Seyller, T.; Lemme, M. C.; Niklaus, F. Direct observation of grain boundaries in graphene through vapor hydrofluoric acid (VHF) exposure. *Sci. Adv.* **2018**, *4*, eaar5170.

[17] Grosse, K. L.; Dorgan, V. E.; Estrada, D.; Wood, J. D.; Vlassiouk, I.; Eres, G.; Lyding, J. W.; King, W. P.; Pop, E. Direct observation of resistive heating at graphene wrinkles and grain boundaries. *Appl. Phys. Lett.* **2014**, *105*, 143109.

[18] Belotcerkovtceva, D.; Maciel, R. P.; Berggren, E.; Maddu, R.; Sarkar, T.; Kvashnin, Y. O.; Thonig, D.; Lindblad, A.; Eriksson, O.; Kamalakar, M. V. Insights and implications of intricate surface charge transfer and sp^3-defects in graphene/metal oxide interfaces. *ACS Appl. Mater. Interfaces* **2022**, *14*, 36209–36216.

[19] Yu, T. H.; Lee, E. K.; Briggs, B.; Nagabhirava, B.; Yu, B. Bilayer graphene system: Current-induced reliability limit. *IEEE Electron Device Lett.* **2010**, *31*, 1155–1157.

[20] Banszerus, L.; Schmitz, M.; Engels, S.; Goldsche, M.; Watanabe, K.; Taniguchi, T.; Beschoten, B.; Stampfer, C. Ballistic transport exceeding 28 μm in CVD grown graphene. *Nano Lett.* **2016**, *16*, 1387–1391.

[21] Verguts, K.; Defossez, Y.; Leonhardt, A.; De Messemaeker, J.; Schouteden, K.; Van Haesendonck, C.; Huyghebaert, C.; De Gendt, S.; Brems, S. Growth of millimeter-sized graphene single crystals on Al$_2$O$_3$ (0001)/Pt (111) template wafers using chemical vapor deposition. *ECS J. Solid State Sci. Technol.* **2018**, *7*, M195–M200.

[22] Vera-Marun, I. J.; van den Berg, J. J.; Dejene, F.; van Wees, B. J. Direct electronic measurement of Peltier cooling and heating in graphene. *Nat. Commun.* **2016**, *7*, 11525.

[23] Breitenstein, O.; Warta, W.; Langenkamp, M. *Lock-in Thermography*; Springer Berlin, Heidelberg, 2005.

[24] Harzheim, A.; Spiece, J.; Evangeli, C.; McCann, E.; Falko, V.; Sheng, Y. W.; Warner, J. H.; Briggs, G. A. D.; Mol, J. A.; Gehring, P. et al. Geometrically enhanced thermoelectric effects in graphene nanoconstrictions. *Nano Lett.* **2018**, *18*, 7719–7725.

[25] Sierra, J. F.; Neumann, I.; Costache, M. V.; Valenzuela, S. O. Hot-carrier seebeck effect: Diffusion and remote detection of hot carriers in graphene. *Nano Lett.* **2015**, *15*, 4000–4005.

[26] Bakker, F. L.; Slachter, A.; Adam, J. P.; van Wees, B. J. Interplay of peltier and seebeck effects in nanoscale nonlocal spin valves. *Phys. Rev. Lett.* **2010**, *105*, 136601.

[27] Sierra, J. F.; Neumann, I.; Cuppens, J.; Raes, B.; Costache, M. V.; Valenzuela, S. O. Thermoelectric spin voltage in graphene. *Nat. Nanotechnol.* **2018**, *13*, 107–111.

[28] Parkin, S. S. P.; Kaiser, C.; Panchula, A.; Rice, P. M.; Hughes, B.; Samant, M.; Yang, S. H. Giant tunnelling magnetoresistance at room

temperature with MgO (100) tunnel barriers. *Nat. Mater.* **2004**, *3*, 862–867.

[29] Zhang, S.; Levy, P. M.; Marley, A. C.; Parkin, S. S. P. Quenching of magnetoresistance by hot electrons in magnetic tunnel junctions. *Phys. Rev. Lett.* **1997**, *79*, 3744–3747.

[30] Levy, P. M.; Fert, A. Spin transfer in magnetic tunnel junctions with hot electrons. *Phys. Rev. Lett.* **2006**, *97*, 097205.

[31] Fert, A.; Jaffrès, H. J. Conditions for efficient spin injection from a ferromagnetic metal into a semiconductor. *Phys. Rev. B* **2001**, *64*, 184420.

[32] Durkan, C.; Xiao, Z. C. On the failure of graphene devices by joule heating under current stressing conditions. *Appl. Phys. Lett.* **2015**, *107*, 243505.

[33] Neumann, I.; Costache, M. V.; Bridoux, G.; Sierra, J. F.; Valenzuela, S. O. Enhanced spin accumulation at room temperature in graphene spin valves with amorphous carbon interfacial layers. *Appl. Phys. Lett.* **2013**, *103*, 112401.

[34] Kamalakar, M. V.; Dankert, A.; Bergsten, J.; Ive, T.; Dash, S. P. Enhanced tunnel spin injection into graphene using chemical vapor deposited hexagonal boron nitride. *Sci. Rep.* **2014**, *4*, 6146.

[35] Kamalakar, M. V.; Dankert, A.; Kelly, P. J.; Dash, S. P. Inversion of spin signal and spin filtering in ferromagnet|hexagonal boron nitride-graphene van der Waals heterostructures. *Sci. Rep.* **2016**, *6*, 21168.

[36] Gurram, M.; Omar, S.; van Wees, B. J. Electrical spin injection, transport, and detection in graphene-hexagonal boron nitride van der Waals heterostructures: Progress and perspectives. *2D Mater.* **2018**, *5*, 032004.

[37] Friedman, A. L.; van 't Erve, O. M. J.; Li, C. H.; Robinson, J. T.; Jonker, B. T. Homoepitaxial tunnel barriers with functionalized graphene-on-graphene for charge and spin transport. *Nat. Commun.* **2014**, *5*, 3161.

[38] Dayen, J. F.; Ray, S. J.; Karis, O.; Vera-Marun, I. J.; Kamalakar, M. V. Two-dimensional van der Waals spinterfaces and magnetic-interfaces. *Appl. Phys. Rev.* **2020**, *7*, 011303.

80

High current limits in chemical vapor deposited graphene spintronic devices

Daria Belotcerkovtceva[1,§], J. Panda[1,§], M. Ramu[2], Tapati Sarkar[2], Ulrich Noumbe[1], and M. Venkata Kamalakar[1] (✉)
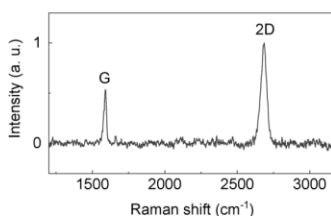
[1] Department of Physics and Astronomy, Uppsala University, Box 516, Uppsala SE-751 20, Sweden
[2] Department of Materials Science and Engineering, Uppsala University, Box 35, Uppsala SE-751 03, Sweden
[§] Daria Belotcerkovtceva and J. Panda contributed equally to this work.

1. Raman spectroscopy of CVD graphene

Figure S1 Raman spectra of CVD graphene on Si/SiO$_2$ substrate used in experiments.

To understand the quality of graphene, we performed Raman spectroscopy of the CVD graphene sample on Si/SiO$_2$ substrate under 532 nm laser excitation. The 2D to G intensity ratio is ~2 which suggests good quality graphene with no defect peaks (Fig. S1).

2. Low current device characterization
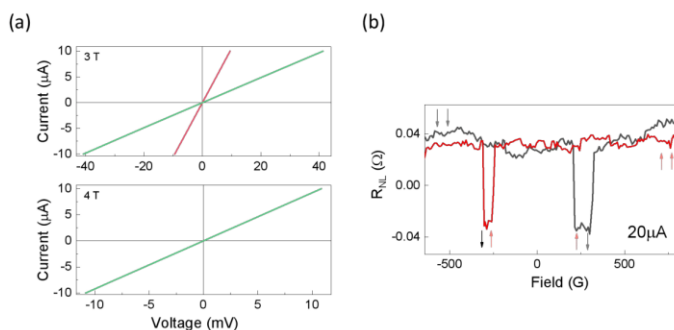
Figure S2 (a) I-V curves measured in 3T configuration to obtain the contact resistance of the injector and detector and 4T I-V curves to calculate the resistivity of the graphene sheet. (b) Spin transport signal measured in the spin-valve geometry showing switching between parallel (↑↑ or ↓↓) to antiparallel (↓↑ or ↑↓) configurations of the injector and detector electrodes at current I = 20 μA.

Address correspondence to venkata.mutta@physics.uu.se

We measured the contact resistance of the ferromagnetic tunnel contacts using 3T configuration I-V characteristics (Fig. S2a). The contact resistance was found to be in the range of 1 - 4 kΩ. To get an efficient spin injection into the graphene the contact resistance should be higher than the graphene sheet resistance. We have also performed four-terminal I-V characteristics to calculate the graphene sheet resistance (Fig. S2a) and observed the sheet resistance of the graphene is 540 $\Omega\square^{-1}$.

We performed nonlocal (NL) measurements to observe spin transport. In the NL scheme, spin currents are electrically injected into the graphene channel through the current circuit (I), and the resulting diffusion spin current at a distance of L is detected by the voltage circuit (V). Such isolation of the current and voltage circuits allows for faithful measurement of pure spin accumulation, eliminating spurious magneto-resistive contributions associated with direct charge currents. By sweeping an in-plane magnetic field ($B_{\parallel}$), the relative magnetic orientations of the injector and detector electrodes are switched from parallel to antiparallel configuration, which results in a spin-valve switching in the measured nonlocal spin voltage ΔV ($\Delta V_{NL} = V_{NL}(\uparrow\uparrow) - V_{NL}(\downarrow\uparrow)$). As depicted in the spin chemical potential profile, this allows for the measurement of the difference in spin chemical potentials for up ($\mu\uparrow$) and down spins ($\mu\downarrow$), also known as the net spin accumulation at a distance L. In our experiments, we perform NL measurements by sweeping the magnetic field forward (-B to +B) and reverse (+B to –B). A clear spin valve signal with spin NL spin-valve resistance $\Delta R_{NL} = \Delta V_{NL}/I \sim 68$ mΩ was observed at room temperature (shown in Fig. S2b). The obtained values are in nearly the same order as previously reported on Si/SiO$_2$ devices [1–3].

3. High current T and 4T I-V characteristics
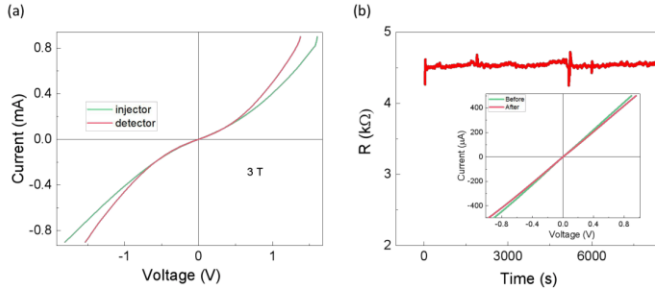
Figure S3 (a) The contact resistance of the injector and detector measured in a 3-terminal (3T) configuration at a higher bias current. (b) The 4T resistance of the CVD graphene as a function of time measured at a higher bias current of 1 mA and the inset shows the four-probe I-V curves before and after endurance measurements.

We have measured the contact resistance of the tunnel contact using the 3T configuration in the device at a higher bias current (Fig. S3a). The 3T I-V clearly shows the nonlinear behavior at a higher bias current also, expected for tunnel contacts used in graphene spin valves. The nonlinearity in I-V curves was observed due to the tunneling behavior across the junction as well as the self-heating at higher bias voltage [4–6] and some variations in resistance can be associated with inhomogeneous graphene/contact interface or nanofilaments formation. For these specific contacts, the contacts show low resistance ($\sim$ kΩ), and the contact shows non-linear tunneling characteristics for fairly large currents without any degradation. Figure S3b shows the resistance of the graphene as a function of time for applied constant bias current of 1 mA. After a long time (about 9000 s), the graphene still has sustained nearly the same resistance with a higher bias current.

References

[1]   L. Banszerus, M. Schmitz, S. Engels, M. Goldsche, K. Watanabe, T. Taniguchi, B. Beschoten, and C. Stampfer, *Ballistic Transport Exceeding 28 Mm in CVD Grown Graphene*, Nano Lett. **16**, 1387 (2016).

[2]   K. Verguts, Y. Defossez, A. Leonhardt, J. De Messemaeker, K. Schouteden, C. Van Haesendonck, C. Huyghebaert, S. De Gendt, and S. Brems, *Growth of Millimeter-Sized Graphene Single Crystals on Al 2 O 3 (0001)/Pt(111) Template Wafers Using Chemical Vapor Deposition* , ECS J. Solid State Sci. Technol. **7**, M195 (2018).

[3]   M. V. Kamalakar, C. Groenveld, A. Dankert, and S. P. Dash, *Long Distance Spin Communication in Chemical Vapour Deposited Graphene*, Nat. Commun. **6**, 6766 (2015).

[4]   T. Yu, E. K. Lee, B. Briggs, B. Nagabhirava, and B. Yu, *Bilayer Graphene System: Current-Induced Reliability Limit*, IEEE Electron Device Lett. **31**, 1155 (2010).

[5]   K. J. Lee, A. P. Chandrakasan, and J. Kong, *Breakdown Current Density of CVD-Grown Multilayer Graphene Interconnects*, IEEE Electron Device Lett. **32**, 557 (2011).

[6]   R. Murali, Y. Yang, K. Brenner, T. Beck, and J. D. Meindl, *Breakdown Current Density of Graphene Nanoribbons*, Appl. Phys. Lett. **94**, 2007 (2009).